UNIVERSITAT POLITÈCNICA DE CATALUNYA BARCELONATECH

Computer modeling of the polarity and amoeboid motion of living cells

Thesis submitted for the degree of
Doctor of Physics, March 2022.

Eduardo Moreno Ramos

Computational and Applied Physics Program

Supervised by

Dr. Sergio Alonso Muñoz

Signature _____

Date _____ / _____ / _____

Abstract

Cell motility is important in many biological processes. Some examples relay in epidermal cells moving towards lesions during wound healing, neutrophils cells migrating towards sites of bacterial infection as part of the immune response, or sperm cells following chemical gradient to reach the ovum.

Migration is a process observed in both, prokaryotes and eukaryotes cells. There exist many different mechanisms of migration depending on the particular cell, such as flagella, amoeboid, crawling or gliding motility. This work focus on the mathematical description of amoeboid crawling-like movement which is one of the most common type of locomotion in eukaryotic cells.

Motility involves a network of interactions among multiple biochemical components. For example, before moving, cells produce an accumulation of proteins/lipids at the membrane in response to an external signal. This process is known as polarization. Next step is the activation of the cytoskeleton, which is the responsible of the locomotion of the cell. Consequently, actin microfilament network forming the cytoskeleton, pushes the membrane and triggers the formation of pseudopods, blebs or filopodia giving rise to the motion of the cell.

One well studied system for this purpose is the amoeba *Dictyostelium Discoideum*, which is a eukaryotic cell that moves in presence (chemotaxis) or absence of external signals. Experiments show that *Dictyostelium Discoideum* present different shapes during motion, perform directed motion inside micro channels, and interact/trasport with micro-objects like small beads.

In this work, a mathematical nonlinear reaction-diffusion model in combination with a dynamic phase field is proposed to reproduce different motility scenarios as amoeboid and fan-shape. Experimental data related with the dynamics of *Dictyostelium Discoideum* were supplied by the Biological Physics Group at the University of Potsdam. A comparison between the numerical simulations and live cell experiments of *D. Discoideum* cells under different developmental conditions permits the optimization of the model.

Alternatively, the model is extended to analyze the effects of the formation of clusters by the interaction with a group of cells and when a single cell is confined inside a microchannel.

Two more complex biochemical models that take into account a more detailed dynamics of the intracellular reactions of *D. Discoideum* cells were also coupled to a dynamic phase field.

This work produces a computational synthetic cell that mimic the dynamics of experimental cells. The use of numeric methods and mathematical models helps with the understanding of the biological process involved in cell locomotion.

Resumen

La motilidad celular es importante en muchos procesos biológicos. Algunos ejemplos se relacionan con células epidérmicas que se desplazan hacia las lesiones durante la cicatrización de heridas, células de neutrófilos que migran hacia sitios de infección bacteriana como parte de la respuesta inmunitaria o espermatozoides que siguen un gradiente químico para llegar al óvulo.

La migración es un proceso observado tanto en células procariotas como eucariotas. Existen muchos mecanismos diferentes de migración dependiendo de la célula en particular, como flagelos, ameboides o motilidad deslizante. Este trabajo se centra en la descripción matemática del movimiento ameboide, que es uno de los tipos de locomoción más comunes en las células eucariotas.

La motilidad implica una red de interacciones entre múltiples componentes bioquímicos. Por ejemplo, antes de moverse, las células producen una acumulación de proteínas/lípidos en la membrana en respuesta a una señal externa. Este proceso se conoce como polarización. El siguiente paso es la activación del citoesqueleto, que es el responsable de la locomoción de la célula. En consecuencia, la red de microfilamentos de actina formada por el citoesqueleto, empuja la membrana y desencadena la formación de seudópodos, ampollas o filopodios que dan lugar al movimiento de la célula.

Un sistema bien estudiado para este propósito es la ameba *Dictyostelium Discoideum*, que es una célula eucariota que se mueve en presencia (quimiotaxis) o ausencia de señales externas. Los experimentos muestran que *Dictyostelium Discoideum* presenta diferentes formas durante el movimiento, realizar un movimiento dirigido dentro de microcanales e interactuar o transportar pequeños micro-objetos (beads).

En este trabajo, se propone un modelo matemático no lineal de reacción-difusión en combinación con un *phase field* dinámico para reproducir diferentes escenarios de motilidad tales como ameboide y *fan-shape*. Los datos experimentales relacionados con la dinámica de *Dictyostelium Discoideum* fueron proporcionados por el Grupo de Física Biológica de la Universidad de Potsdam. Una comparación entre las simulaciones numéricas y los experimentos con células vivas de *D. Discoideum* células bajo diferentes condiciones de desarrollo permite la optimización del modelo.

Alternativamente, el modelo se extiende para analizar los efectos de la formación de grupos por la interacción con un grupo de células y cuando una sola célula está confinada dentro de un microcanal.

Dos modelos bioquímicos más complejos que toman en cuenta una dinámica más detallada de las reacciones intracelulares de celulas *D. Discoideum* fueron acoplados a un *phase field* dinámico.

Este trabajo produce computacionalmente una célula sintética que imita la dinámica de las células experimentales. El uso de métodos numéricos y modelos matemáticos ayuda a comprender el proceso biológico involucrado en la locomoción celular.

Resum

La motilitat cellular és important en molts processos biològics. Alguns exemples es relacionen amb cèllules epidèrmiques que es desplacen cap a les lesions durant la cicatrització de ferides, cèllules de neutròfils que migren cap a llocs d'infecció bacteriana com a part de la resposta immunitària o espermatozoides que segueixen un gradient químic per arribar a l'òvul.

La migració és un procés observat tant en cèllules procariotes com eucariotes. Hi ha molts mecanismes diferents de migració depenent de la cèllula en particular, com flagels, ameboides o motilitat lliscant. Aquest treball se centra en la descripció matemàtica del moviment ameboide, que és un dels tipus de locomoció més comuns a les cèllules eucariotes.

La motilitat implica una xarxa d'interaccions entre múltiples components bioquímics. Per exemple, abans de moure's, les cèllules produeixen una acumulació de proteïnes/lípids a la membrana en resposta a un senyal extern. Aquest procés es coneix com a polarització. El pas següent és l'activació del citoesquelet, que és el responsable de la locomoció de la cèllula. En conseqüència, la xarxa de microfilaments d'actina formada pel citosquelet, empeny la membrana i desencadena la formació de pseudòpodes, butllofes o filopodis que donen lloc al moviment de la cèllula.

Un sistema ben estudiat per a aquest propòsit és l'ameba *Dictyostelium*

Discoideum, que és una cèllula eucariota que es mou en presència (quimiotaxi) o absència de senyals externs. Els experiments mostren que *Dictyostelium Discoideum* presenta diferents formes durant el moviment, realitzar un moviment dirigit dins de microcanals i interactuar o transportar petits microobjectes (beads).

En aquest treball, es proposa un model matemàtic no lineal de reacció-difusió en combinació amb un *phase field* dinàmic per reproduir diferents escenaris de motilitat tals com ameboide i *fan-shape*. Les dades experimentals relacionades amb la dinàmica de *Dictyostelium Discoideum* van ser proporcionades pel Grup de Física Biològica de la Universitat de Potsdam. Una comparació entre les simulacions numèriques i els experiments amb cèllules vives de *D. Discoideum* cèllules sota diferents condicions de desenvolupament permet l'optimització del model.

Alternativament, el model s'estén per analitzar els efectes de la formació de grups per la interacció amb un grup de cèllules i quan una sola cèllula està confinada dins un microcanal.

Dos models bioquímics més complexos que tenen en compte una dinàmica més detallada de les reaccions intracellulars de cèllules *D. Discoideum* van ser acoblats a un *phase field* dinàmic.

Aquest treball produeix computacionalment una cèllula sintètica que imita la dinàmica de les cèllules experimentals. L'ús de mètodes numèrics i models matemàtics ajuda a comprendre el procés biològic involucrat en la locomoció cellular.

Acknowledgements

Primero que nada quiero agradecer de la manera mas sincera a mi asesor **Sergio Alonso** por el hecho de haber aceptado ser mi tutor, de tenerme toda la paciencia necesaria, darme todo el apoyo en cada momento y guiarme paso a paso durante estos cuatro años para poder completar este trabajo, de todo corazón mil gracias Sergio.

Agradezco también a las excelentes personas que tuve la oportunidad de conocer en el grupo de Física de la UPC por todos los ratos compartidos dentro y fuera de la universidad. Gracias a los profesores Blas, Laureano y Enric. Tambien gracias a los compañeros de despacho Francesc, Miquel, Martí, David, Dafni, Thomas, Miquel B, Gustavo y YunXian. Además de todo el personal administrativo del departamento de Física.

También un agradecimiento especial al Profesor Carsten Beta y a todos los miembros del grupo de Biofísica de la Universidad de Potsdam por abrirme las puertas a ser parte temporal de su grupo.

Por otra parte otra mención a todas las personas que me han impulsado a seguir y a creer en mi mas de lo que yo mismo lo he hecho, empezando por mi familia, mis padres Eduardo y Alejandra y mi hermana Alejandra; mis amigos Toño, Luis, Gio que siempre estuvieron al tanto; y a todas las personas que he conocido estos años desde que comenzó este proceso y con las que he compartido todo tipo de momentos y experiencias. Luis P, Diana, Merry, Yaz, Pao, Afef, Heber, JJ, Alex...

Finalmente un último agradecimiento al gobierno de México por el apoyo recibido por parte de CONACYT, el cual me dio la oportunidad de haber estudiado este grado.

Contents

Abstract i

Acknowledgements vii

List of Tables xi

List of Figures xii

Abbreviations 1

Chapter 1 Introduction 1

1.1 Biology of Cell Locomotion 2

1.2 Physics of Cell Locomotion. 12

1.3 Objectives of the work 20

1.4 Organization of the work 21

Chapter 2 Methods 24

2.1 Phase field coupled to a generic bistable reaction-diffusion model for cell motion 25

2.2 Numerical solution of the model 28

Chapter 3 Modeling cell crawling dynamics: from amoeboid to fan-shape motion 33

3.1 Introduction 33

3.2 Experimental Methods 35

3.3 Computational results of the motility scenarios obtained by the bistable model 36

3.4 Cell shapes and velocities in numerical simulations are comparable to experimental values 47

3.5 Discussion 51

Chapter 4 Computational study of interacting cells 56

4.1 Introduction 56

4.2 Phase field description for a multi cellular system 59

4.3 Defining polarity and velocity vectors of migrating cells . . . 61

4.4 Protocol of the interaction between two cells 62

4.5 Motion of single cell depends on polarization 63

4.6 Simulation results of the interactions between two cells . . . 65

4.7 Simulation results with larger set of cells 71

4.8 Increase of density decreases mobility and misalign polarization and motion 72

4.9 Increasing of the system size keeping the density of cells does not modify the observed dynamics 77

4.10 Discussion 79

Chapter 5 Crawling cells in a confined environment 85

5.1 Introduction 85

5.2 Phase field coupled to a crawling cell model inside microchannels 88

5.3 Results of random and persistent cell migration inside microchannels 89

5.4 Discussion 92

Chapter 6 Coupled Ras-Pseudopod inducer model for a crawling cell 95

6.1 Introduction 95

6.2 Biochemical model for Ras activation and pseudopod extension 97

6.3 Mathematical description of the mass-conservation constrain 100

6.4 One dimension results of Ras model are based in stochastic generation of patches 101

6.5 Addition of a physical phase field model for cell shape deformations 106

6.6 Two dimensional stochastic bistable model provides a mechanism of cell crawling motion 107
6.7 Mass-conservation constraint in the Ras model adds more robustness to the system 114
6.8 Influence of cAMP gradient on cell motility 116
6.9 Discussion 118
Chapter 7 Biochemical excitability triggers symmetry breaking 122
7.1 Introduction 122
7.2 Modeling cell symmetry breaking in a $Ras - PIP_3$ system . 124
7.3 One dimensional results for the symmetry breaking Ras-PIP_3 system 129
7.4 Phase field coupled to a symmetry breaking Ras-PIP_3 system 134
7.5 Discussion 136
Chapter 8 Conclusions and outlook. 138
Bibliography 142
Appendices 173
Appendix A Tables 174

List of Tables

A.1 Parameter values for the numerical generic bistable model. . 174
A.2 Parameter values for the numerical biochemical bistable model. 175
A.3 Phase field parameter values for the numerical biochemical bistable model. 176
A.4 Parameter values for the numerical biochemical excitable model. 177

List of Figures

1.1 Diagram of divisions of the living word cells. 3

1.2 Representation of an eukaryotic cell. 4

1.3 Snapshots of *Dictyostelium Discoideum*. 6

1.4 Lifecycle of *Dictyostelium Discoideum*. 8

1.5 Different modes of movement at cellular level. 9

1.6 Examples of some types of organism taxes. 10

1.7 Nullclines and evolution of the concentration for the Fitz-Hugh Nagumo model. A) and B) shows excitable dynamics; C) and D) shows bistable dynamics and E) and F) shows oscillatory dynamics. 15

1.8 Different type interfaces of a phase field variable 19

3.1 Phase diagram of the cell shapes obtained from the numeric generic bistable model. 38

3.2 Complete phase diagrams of the cell shape obtained from generic bistable model. 39

3.3 Numerical and experiments for amoeboid motion. 40

3.4 Numerical and experimental results for the intermediate unstable case. 42

3.5 experimental results for the intermediate unstable case . . . 43

3.6 Numerical and experimental results for the rotational fan-shaped case. 45

3.7 Phase diagram of the entire range of different dynamics obtained from the model at low noise intensity and as a function of the reaction rate k_a versus the maximum area coverage C_0. 46
3.8 Phase diagram by changing the diffusion coefficient (D) and the surface tension (γ) of the numerical simulations of fan-shaped cells. 46
3.9 Directionality ratio from simulations and experiments over $600s$. 49
3.10 Circularity box plot and plot over time representation of amoeboid and fan-shaped cells from simulations and experiments. 52

4.1 Phenotype of simulated cells and vector components measured. 62
4.2 Representation of the collision types and its respective scenario after colliding. 63
4.3 Phenotype snapshots, trajectories, polarity, velocity vectors and angle between results obtained from the bistable generic model by varying reaction rate parameter. 66
4.4 Magnitude of polarity, velocity and angle at different values or reaction rate. 67
4.5 Sequence of snapshots in a two cell interaction scenario representing the alignment, avoidance and stick/push scenarios corresponding to glancing collision dynamics observed in *Dyctiostelium Discoideum* simulations. 69
4.6 Phenotype snapshots, trajectories, polarity, velocity vectors and angle between results obtained from the bistable generic model by varying reaction rate parameter for two cells interaction. 70

4.7 Boxplot representations for the measured angles in the interaction of two cells. 71
4.8 Representative time snapshots in a multiple cell interactive system with periodic boundary conditions. 73
4.9 Snapshots of simulations keeping the number of cells constant at $N = 25$ and changing the grid size with a length separation of $L = 12\mu m$ between a consecutive frame. 74
4.10 Frequency of the size of the clusters, maintaining constant at $N = 25$ the number of cells in the system and changing the grid size. 76
4.11 Mean square displacement divided by time for the group of $N = 25$ cells in different grid squares, together with diffusion coefficients extracted from fitting the Fürth formula. 77
4.12 Snapshots of simulations with the same packing fraction value $\rho_R = 0.78$. Number of cells varied between 25 to 81. . 78
4.13 Frequency of the size of the clusters, maintaining constant the cell density of the system but changing the grid size and the number of cells from 25 to 81. 79

5.1 Most common materials in microfluidic chips (silicon, glass and polymers) and a scheme of a PDMS device microfluidic channel. 86
5.2 Snapshots for a in vivo persistent moving cell inside a microchannel environment. 87
5.3 Snapshots for the different channel width used in simulations. 90
5.4 Sequencially snapshots for the two representative cell population of cells inside the microchannels. 91
5.5 Horizontal axes positions of several trajectories for different reaction rate parameter and width size of the channel. 92

5.6 Mean velocities for different width channel and reaction rate parameter. 93

6.1 Sketch of the biochemical model of polarization and locomotion modules. 98

6.2 Spatio-temporal plots of R (in green) and P (in red) for different values of k_5 and k_2. Variance of noise intensity was fixed at $\sigma_R = 0.04$ and $\sigma_P = 0.025$. 103

6.3 Spatio-temporal plots of R (in green) and P (in red) for different values of k_{14} and k_{18}. Variance of noise intensity was fixed at $\sigma_R = 0.04$ and $\sigma_P = 0.025$. 104

6.4 Hysteresis curves of the deterministic model for R dynamics varying k_2, k_5, k_{14} and k_{18}. 105

6.5 Snapshots of R (in green) and P (in red) dynamics obtained from computer simulations without mass conservation by applying the phase field technique for fixed noise intensity values and different values of k_2 and k_5. 108

6.6 Snapshots of R (in green) and P (in red) dynamics obtained from computer simulations without mass conservation by applying the phase field technique for fixed noise intensity values and different values of k_{14} and k_{18}. 109

6.7 Map of snapshots taken from different variance values of noise intensity for the no mass conserved model. 110

6.8 Snapshots of R (in green) and P (in red) dynamics obtained from computer simulations with mass conservation by applying the phase field technique for fixed noise intensity values and different values of k_2 and k_5. 112

6.9 Map of snapshots taken from different variance values of noise intensity for the mass conserved model. 113

6.10 Kymograph for the two most representative cases of crawling cells obtained by the model. 113
6.11 Box plot representation for the cell speed of the model without (blue color) and with (red color) mass conservation condition. 115
6.12 Speed bar plots measured by the no conserved (blue bars) and conserved (red bars) model. Noise variance σ_P was varied and σ_R was fixed in every panel. 116
6.13 Time snapshots of an amoeboid type cell without the presence of an external gradient and under the presence of a linear gradient. 118
6.14 Simulated cell trajectories for different gradient intensity. . . 119
6.15 Spatio-temporal plots of R (in green) and P (in orange) for different values of the coupling parameter between R and P. 121

7.1 PIP_3 and Ras-GTP waves for deterministic and stochastic simulations. 130
7.2 PIP_3 and Ras-GTP waves for deterministic and stochastic simulations. No PI3K activity was assumed during two periods of time in the simulation. $V_{GEF} = 600s^{-1}$ was considered. 131
7.3 Deterministic and stochastic simulations for Ras-GTP waves. PI3K activity was kept activated only during the first half of the simulation. 133
7.4 Snapshots of PIP_3 waves taken from the stochastic simulation of the two dimensional Ras-PIP_3 model. 134
7.5 Stochastic simulations of the Ras-PIP_3 model when coupled with a dynamical phase field. 136

Chapter 1

Introduction

All existing living organisms have one thing in common: they are made of building blocks called cells. The cell is the basic structural, functional and biological unit of life. Functions they perform include providing structure to the body, taking nutrients from food, converting those nutrients into energy, saving hereditary material to make copies of themselves, and many other functions.

Nowadays, biological research involves experiments where a huge amount of data is present. This is where the work of physics begins, first by allowing us to understand the data and second by predicting how the studied system might work. Once the biology and physics paths cross there emerges a branch of science called biophysics. Biophysics is a field that is specialized in studying how biological processes work. For example, the mechanics of how the molecules of life are made, how different parts of a cell move and function, how our body systems works (brain, circulation, immune system and others) and complex ecosystems [1].

Several subjects are derived and can be studied from a biophysics perspec-

tive—for example, data analysis, computer modelling, neuroscience, medical applications, bio-materials and many others. Of all those mentioned, this work will be focusing on computer modelling as the main tool to study cell polarization, which is the process of how a cell breaks its symmetry in order to define one head/front and tail/back, and the resulting cell motion.

1.1 Biology of Cell Locomotion

1.1.1 Cell Clasification

Living cells can be classified on the basis of cell structure into two groups: prokaryotes and eukaryotes. Some of the most important differences between them is that eukartyotic cells contains a nucleus while prokaryotic cells do not. Also, prokaryotes are single-celled organisms, while eukaryotes can be either single-celled or multicellular [2].

At the same time two of the three domains of life are included in prokaryotes cells: bacteria and archae. The remaining domain belongs to eukaryotic cells: eukarya, which at the same time can be classified into different kingdoms (see Figure 1.1). This classification was proposed by Carl Woese based on rRNA data [3, 4].

Most prokaryotic cells are small and simple in outward appearance, living mostly as independent individuals or in loosely organized communities. They are typically spherical or rod-shaped and measure 1-10 μm (micrometers) in linear dimension. Another characteristic of this type of cell is the lack of organelles such as the nucleus and mitochondria.

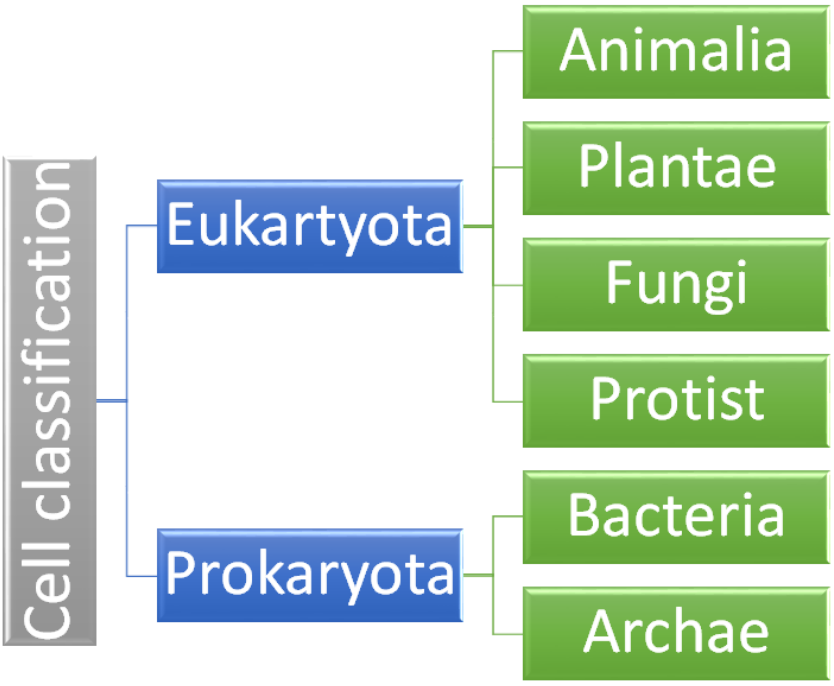

Figure 1.1: Diagram of divisions of the living world. Bacteria and archae included in prokaryotic cells. And eukarya included in eukaryotic cells and at the same time divided into different kingdoms.

1.1.2 Eukaryotic Cells

Eukaryote cells are in general biochemically more diverse, more elaborate and bigger (typically 10 times bigger in linear dimension and 1,000 times larger in volume) than prokaryotic cells, see Figure 1.2. This size increase is accompanied by radical differences in structure and function. This type of cell, unlike the prokaryotic, has a nucleus where DNA is stored. Most also have mitochondria, which can be seen as a small bodies in the cytoplasm that generate most of the chemical energy taking oxygen and harnessing energy from the oxidation of food molecules to produce adenosin triphosphate (ATP), an organic compound that powers the cell's activities.

Having defined some of the main characteristics of eukaryotic cells another classification for this type of cells will be undertaken. There are many different types of eukaryotic cells with some substantial differences among

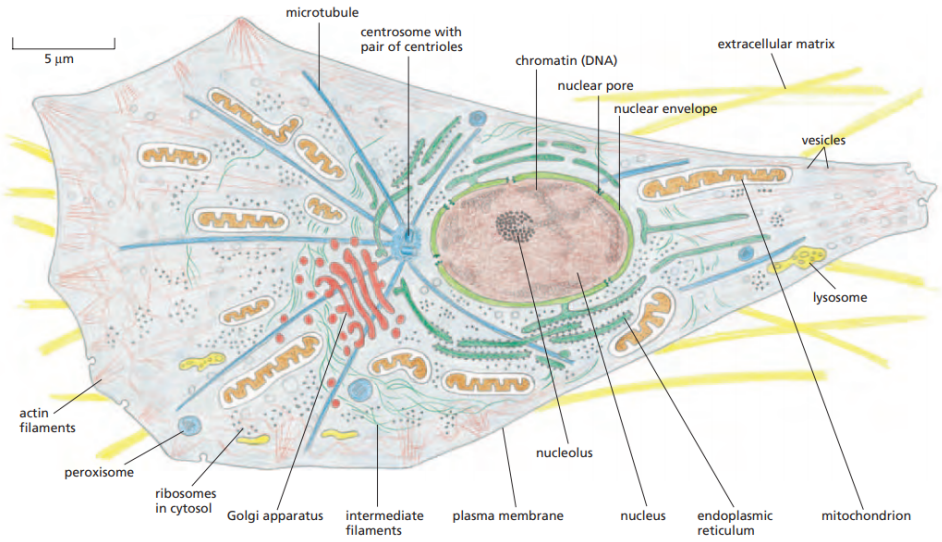

Figure 1.2: Representation of an eukaryotic cell, in this case an animal cell. This kind of cell almost share the same components with plant, fungi and protist kingdom cells. Image taken from [2].

them. they can be commonly classified as animal, plant, fungi and protist [5].

A feature that may be mentioned of this classification is that for example, plant cells and fungi cells have the presence of a cell wall, with the difference that the wall contains cellulose for the plant cells and chitin for the fungus cells. In contrast, animal cells, and some protist cells, can transform into a variety of shapes in comparison with plant and fungi cells due to the lack of a cell wall.

1.1.3 The solitary eukaryotic cells: Protist Kingdom

Protist cells are eukaryotic single-celled organisms that live a solitary life. They sometimes live in small colonies that behave as a group of free-living cells and in other ways as a multicellular organism. Protists are subdivided into groups based on similar characteristics with other kingdoms [6]. For example, some organisms of this category hunt like animals (protozoa),

photosynthesize like plants (the unicellular algae) or scavenge like fungi cells (the unicellular fungi or yeasts and slime molds). And yet, they do not fit into any of these groups.

In the family of protists there are six major groups. One is the Amoebozoa which is also divided into more subgroups. One of these groups mentioned before is commonly called slime molds. This type of cell has the characteristic of interacting depending on the presence or absence of food, acting as single-cell organisms or congregating as a single body, respectively. They feed on microorganisms like bacteria (mostly Escherichia Coli, yeast and fungi) that live in dead plant material, contributing to the decomposition of dead vegetation. For this reason, slime molds are usually found in soil, lawns and on the forest floor. At the same time, slime molds are also classified into the following different types.

The first is the Plasmodial slime molds, basically enormous single cells with thousands of nuclei. They are formed when individual flagellated cells swarm together and fuse. The result is one large bag of cytoplasm with many diploid nuclei. These giant cells have been extremely useful in studies of cytoplasmic streaming (the movement of cell contents) because it is possible to see this happening even under relatively low magnification. In addition, the large size of slime mold cells makes them easier to handle than other cells.

A second group which is of interest in this work is the cellular slime molds. These organisms spend most of their lives as separate single-celled amoeboid protists, but upon the release of a chemical signal, the individual cells aggregate into a swarm. Cellular slime molds are thus of great interest to cell and developmental biologists, because they provide a comparatively simple and easily manipulated system for understanding how cells inter-

act to generate a multicellular organism. There are two groups of cellular slime molds, the Dictyostelida and the Acrasida, which may not be closely related to each other.

A third group, the Labyrinthulomycota or slime nets, are also called slime molds, but appear to be more closely related to the Chromista, and not relatives of the other slime mold groups [7].

1.1.4 *Dyctiostelium discoideum as a study model organism*

Dictyostelium discoideum is a small (10-20 μm diameter) specie of soil-dwelling amoeba which belongs to the *Amebozoa* phylum and the *Dyctyostelida* slime mold type organism. This organism was discovered in 1935 by K. Raper [8]. Due to its ease of cultivation it is commonly used as a model system to study a variety of biological processes [9].

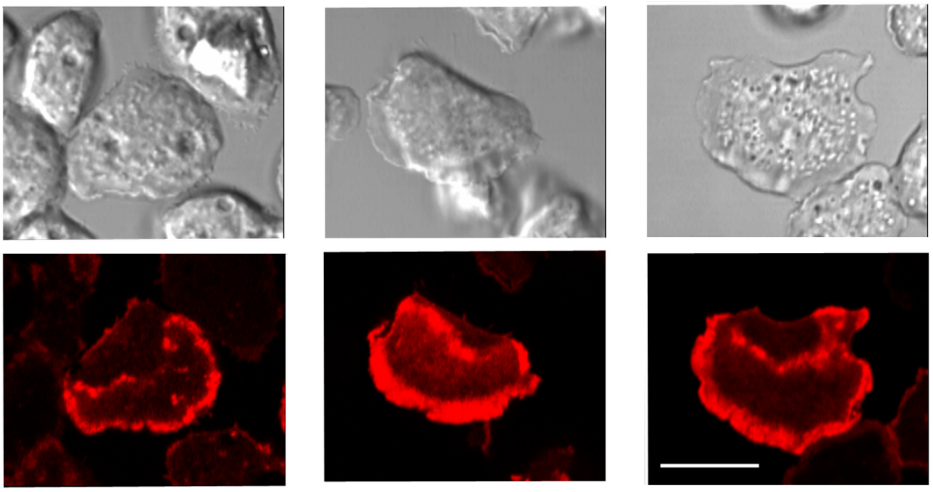

Figure 1.3: Snapshots of *Dictyostelium Discoideum* taken from experiments. Fluorescence part in the bottom panels are related to actin, which forms microfilaments in the cytoskeleton to promote cell movement. Scale bar: $10\mu m$. Image adapted from [10] .

One of the interesting characteristics of *D. Discoideum* organisms is the

social amoeba behavior during their approximately 24 hours life cycle; see Figure 1.4. In this cycle these organisms pass through differentiation, development, morphogenesis and cell death [11]. When starving conditions are present in *D. Discoideum*, it leads to a transition from solitary live single cells to swarming aggregates that eventually develop into multicellular fruiting bodies composed of haploid spores and stalk cells [12].

Aggregation of individual amoebae is mediated by chemoattractant cyclic adenosin monophospahte (cAMP), a substance that triggers the chemotactic movement of cells. For this, one amoeba secretes out a cAMP signal, attracting other amoeba to migrate towards the source [13, 14]. Up to 10^5 individual cells aggregates, leading to the formation of a fruiting body, with the sorus sitting on the top of the stalk. This structure contains cells encapsulated as spores that await dispersal and germination when conditions are favorable for single-cell growth. In this cooperative asexual structure, stalk cells perish and thus exhibit altruistic behavior towards the viable spores which they lift above the substrate, where they are more likely to be dispersed. Once the spores get dispersed a new life cycle begin.

1.1.5 Motility of cells

Motility is one intrinsic characteristic of living systems to exhibit motion and perform mechanical work at the expense of metabolic energy [16]. This ability is affected by two conditions.

First is the genetic, due to the diverse existence of multiple cell phenotypes and the way those cells moves. Some of the cells movements are described briefly below (see Figure 1.5). Flagellar motility has the characteristic that cells present one or more whip-like organelles that protrude from the

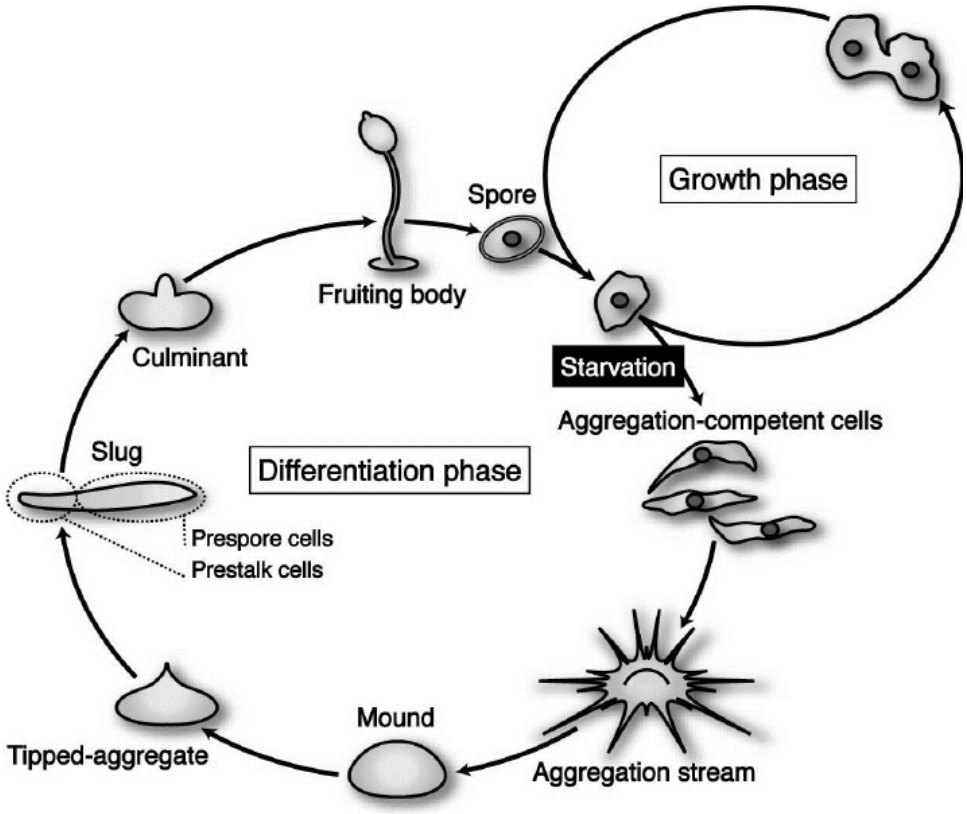

Figure 1.4: Lifecycle of *Dictyostelium Discoideum*. Image taken from [15].

cell body. The main function of these organelles, known as flagellum, is locomotion, but they also work as a sensors of chemicals and temperatures outside the cell [17]. Twitching motility is a form of locomotion dependent on the presence of type IV pili, hair-like filaments that extend out of the cell and permit it to pull forward in a similar way to a grappling hook [18, 19]. Swarming motility, from the verb to swarm, is characterized by movement in large groups. Here, in the same way as flagellar motility, cells use flagellum for displacement [20]. Gliding motility occurs along the long axis of the cell without the aid of flagella or pili, but rather using focal adhesion complexes [21]. Amoeboid motility is a crawling type involving extensions or protrusions of the cell cytoplasm called pseudopods. This kind of movement is one of the most common modes of locomotion in eukaryotic cells [22].

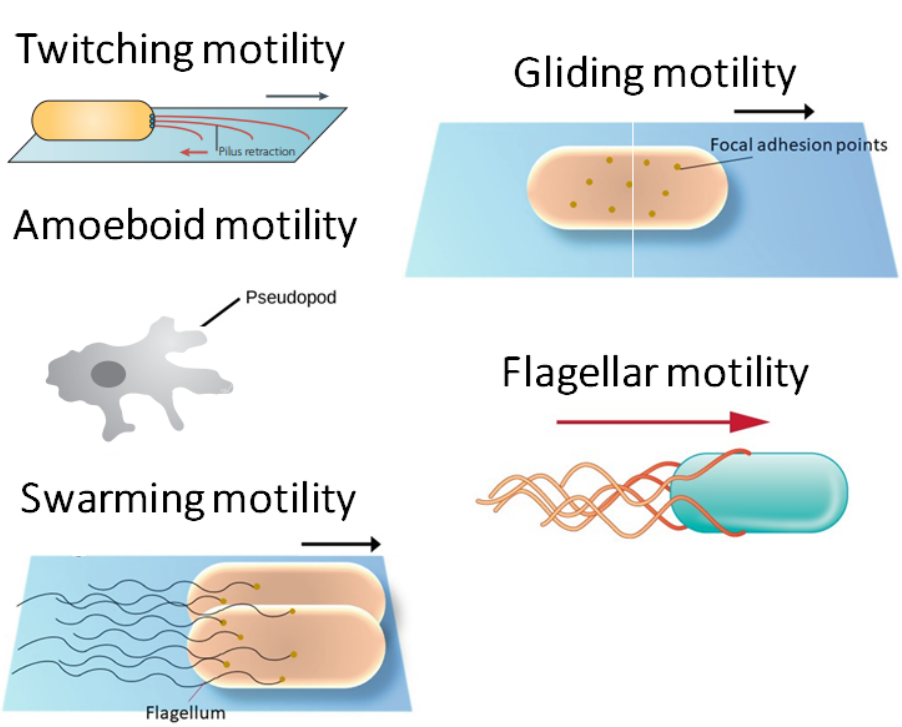

Figure 1.5: Different modes of movement at cellular level. Image adapted from [20, 23].

The second condition is the response to a stimulus of an external environmental factor, known as taxis. Here, we may classify some of the different types of taxis based on the type of stimulus (see Figure 1.6). For example, there is durotaxis, when a cell migrates along an extracellular matrix (ECM) rigidity gradient [24, 25]; electrotaxis or galvanotaxis, with cells guided by an electric field [26, 27]; gravitaxis, a response along the direction of the gravitational force [28]; phototaxis, a movement in response to light [29]; thermotaxis, when the system points its migration towards a gradient of temperature [30]; chemotaxis, a response to a chemical concentration gradient [31]; and many others.

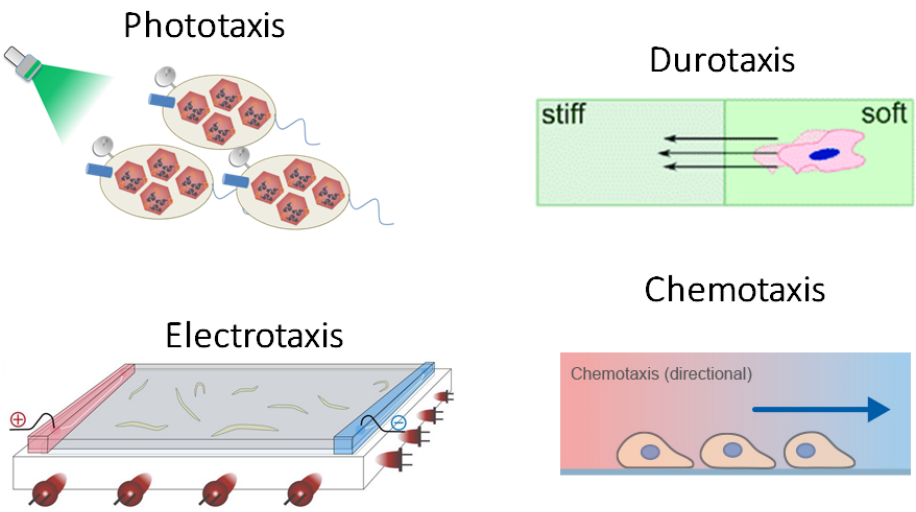

Figure 1.6: Examples of some types of organism taxes. Image adapted from: http://bltdbiostandards.weebly.com/bio-123.html, [25, 27] and https://ibidi.com/content/313-chemotaxis-in-cell-physiology.

1.1.6 Conditions of the cell migration

There are different types of cell motion depending on the cellular type. Keratocytes play a key role in maintaining the transparency of cornea movement in a persistent way, keeping a regular velocity [32, 33]. Sperm cells use the flagellum to reach the egg for fertilization to occur [34]. Leukocytes or white blood cells use their pseudopods to move and keep the human body free of infection [35, 36]. One question that immediately arises is how a cell can define a compass to know in which direction it should move?

All migrating cells have one common characteristic: a process previously defined as polarization. In other words, before moving, cells need the formation of a front and a back to specify an axis to define the direction of motion. This process is important, because without it they would move in all directions at once, producing fluctuating dynamics.

Polarization generally involves a drastic change in the cell shape; it arises primarily through the direct signaling and localization of certain protein

molecules to specific areas of the cell membrane [37, 38, 39, 40]. These changes in the membrane are driven by another component of the cell: the cytoskeleton.

The cytoskeleton may be defined as a system crisscrossing the cytoplasm and formed by a complex network of proteins (actin being one of the most important). It is composed of three main elements: microtubules, microfilaments and intermediate filaments. Together they form a structure of girders, ropes and motors that gives the cell mechanical strength, shape, control and movement guiding [41, 42].

The diversity in cell shapes and functions could lead us to think that the mechanism inside each cell type to restructure the cytoskeleton, organize the proteins and generate polarity must be completely different from others. Nevertheless, all those processes are common to all cell types and they share the same actin filament (or also known as microfilaments) concept.

Actin is a globular protein essentially found in all eukaryotic cells, being the main component of the cell cytoskeleton and responsible for forming the actin filaments [43]. Actin filaments are present in many important cell processes, including cell division [44], cell signaling, cell junctions [45] and cell shape. For example, cell motion is produced when the actin filament network assembles fragments called F-actin at the leading edge of the cell, causing a push on the membrane [46]. The attachment of those filaments to the membrane is controlled by proteins which have a certain affinity for the proteins involved in the polarization process. Therefore, changes in biochemical concentrations may produce local differences in pressure, inducing the formation of filopodia or pseudopods, driving the motion of the cell. After the motion, the cell attaches the new pseudopods onto the substrate they are interacting with to then retract the rear part of the cell

where the pseudopods lose their adhesion in the substrate and pull the cell forward [47, 48].

It is for this reason that when a cell is polarized it has a leading edge where the microfilaments form pseudopods to pull the cell body in that direction. These pseudopods can be formed in the absence of external factors in random places to drive a random migration [49]. However, this does not mean that they cannot keep the same direction for some time before turning. In addition, in the presence of an external signal pseudopods are formed facing that signal, triggering a directed random walk [50].

To review, this work is directed toward the study and modeling of polarization in the social amoeba *Dictyostelium Discoideum*, characterized by their motility, most of the time being persistent and extending presudopods towards the presence of a chemoattractant source, and presenting erratic motion and a random extension of pseudopods in the absence of a gradient of chemoattractant [50, 51].

1.2 Physics of Cell Locomotion.

The integration of a biological system is the result of the interaction of its components in time and space. These components are expressed via measurable quantities in the variables and parameters of the system. The kinetics involved in biological processes are often related with changes in the variables, for example a change in the concentration of certain substances, the number of individual cells, the biomass of the organisms, etc. Another characteristic of the kinetics of a system is the presence of additional parameters that remain unchanged in the whole reaction time, such as temperature, humidity, pH, conductivity, etc [52].

An explanation of the principles of this kind of system is a problem that can be solved with the use of correctly chosen mathematical methods. The changes in variables over time are commonly described using differential equations.

Against this background, it is appropriate to construct a general mathematical model representing the system of study by establishing n differential equations of the form:

$$\frac{\partial c_1}{\partial t} = f_1(c_1, ..., c_n), \tag{1.1}$$

$$\frac{\partial c_n}{\partial t} = f_n(c_1, ..., c_n), \tag{1.2}$$

where $c_1(t), ..., c_n(t)$ are unknown functions of time describing the variables in the system, $\frac{\partial c_i}{\partial t}$ are the rate changes of these variables and f_i are functions dependent on external and internal parameters of the system. Another characteristic of this approach is that the equations included in the model usually include nonlinearities, producing complex dynamics.

1.2.1 Active Elements

One simple approach in the mathematical modeling of the kinetics of biological processes is to refuse to find accurate analytical solutions for the differential equations. The idea is to capture qualitative characteristics of the dynamic behavior of the system, for example stable or unstable stationary states, a transition between them, oscillatory regimes and qualitative dependence on critical values of the parameters. These problems are commonly solved using methods of the qualitative theory of differential

equations which allow one to find essential properties of the model without explicit calculation of the unknown functions. The essential feature of a stationary state is stability, which depends on its ability to return spontaneously to the initial or previous state after the introduction of an external disturbance. We take into consideration the Fitz-Hugh Nagumo model (FHNM) [53, 54], a well-known system described as follow:

$$\frac{\partial x}{\partial t} = x - x^3 - y, \tag{1.3}$$

$$\frac{\partial y}{\partial t} = a(x - by - c), \tag{1.4}$$

which is an example of an Activator-Inhibitor system. In other words, x activates the growth of itself and y, while y inhibits the growth of itself and x. At the same time, the Fitz-Hugh Nagumo model captures three classes of active dynamics depending on the parameters used; these scenarios will be described below. Finally, from the equilibrium point at $dx/dt = 0$ and $dy/dt = 0$ it is possible to obtain the nullclines curves which will give information about the dynamics of the system.

Figure 1.7 A shows a small peak characteristic of an excitable system, where after a period of time the system recovers before supporting another perturbation. The equilibrium point for this case is stable; see Figure 1.7 B.

Bistability is a property in dynamic systems of having two stable equilibrium states. A characteristic of this systems is the chance to make a transition between stable states with large enough perturbations; see Figure 1.7 C. In Figure 1.7 D the nullclines show three different intersections

between them, two being stable points in the extremes and separated by the third unstable equilibrium point.

In Figure 1.7 E the system is driven into oscillatory dynamics. Here, the nullclines only shows one intersection between them, this intersection being an unstable equilibrium point.

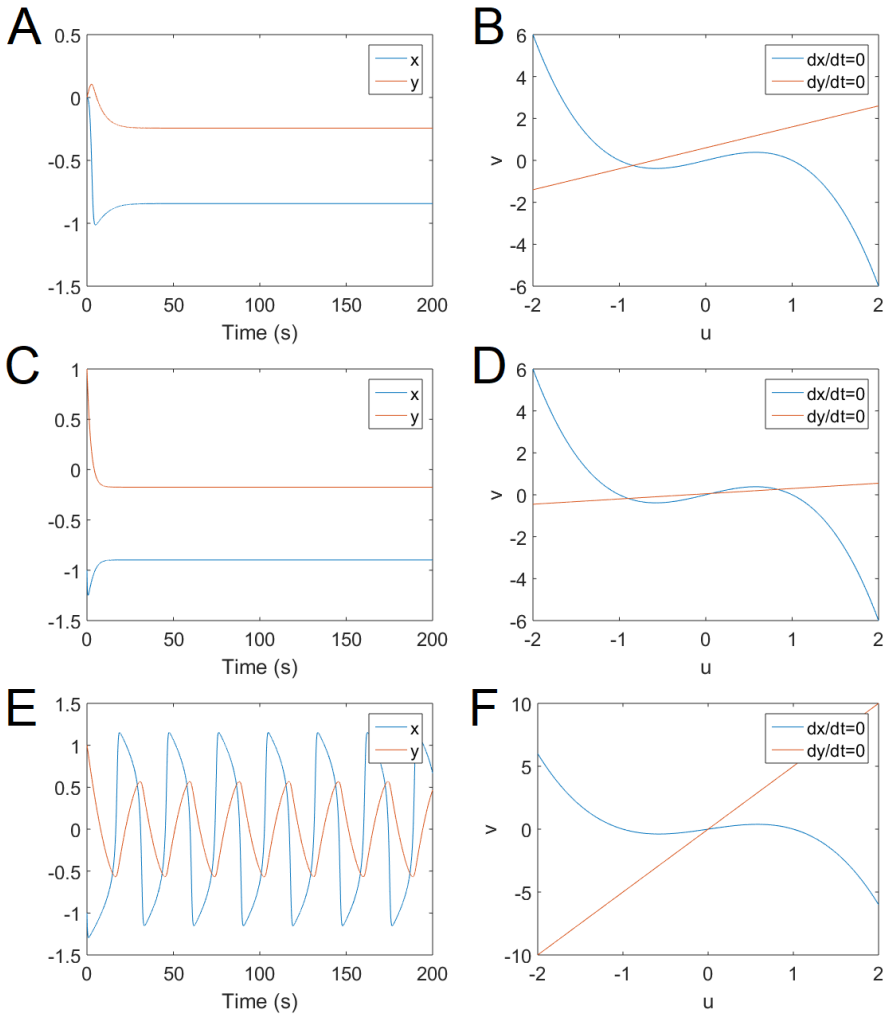

Figure 1.7: Nullclines and evolution of the concentration for the Fitz-Hugh Nagumo model. A) and B) shows excitable dynamics; C) and D) shows bistable dynamics and E) and F) shows oscillatory dynamics.

The previous concepts are very important when we study dynamic phenomena in biology systems, for example in order to understand diverse cell functions such as decision-making processes, cell differentiation, apoptosis [55], homeostasis associated with cancer [56], change in membrane potential

[57, 58], patterns of neural activity in the central nervous system, among others.

1.2.2 Reaction-Diffusion Equations

Now, analyzing models where the variables not only change over time but also change in space as well (known as distributed or spatially models), chemical transformations of substances occur parallel with the diffusion of individual substances from elementary volumes with high concentrations to volumes with low concentrations. Here, the neighboring volumes are connected. Some examples of different biological process in a distributed system are the structure formation in morphogenesis and the propagation of excitable waves in nerve and muscle tissues.

Assuming that in a given volume, the change in the number of particles is equal to the particles that enter or leave the volume

$$\frac{\partial N}{\partial t} = -\int_S \vec{j} \cdot \vec{ds} = -\int_V \vec{\nabla} \cdot \vec{j} dV, \tag{1.5}$$

where $\vec{j}$ is the flux of the particles across the surface. It is also possible to write the total number of particles as a function of the concentration

$$N = \int_V u dV. \tag{1.6}$$

Combining equations (1.5) and (1.6) one can write

$$\int_V \frac{\partial u}{\partial t} dV = -\int_V \vec{\nabla} \cdot \vec{j} dV, \tag{1.7}$$

and

$$\frac{\partial u}{\partial t} = -\vec{\nabla} \cdot \vec{j}. \tag{1.8}$$

Now, assuming Fick's first law [59], which describes the net flux of particles due to a gradient of concentration u and expressed as:

$$\vec{j} = -D\vec{\nabla}u. \tag{1.9}$$

Finally, combining (1.8) and (1.9) one can obtain

$$\frac{\partial u}{\partial t} = D\nabla^2 u, \tag{1.10}$$

which is the diffusion equation for the concentration of particles.

Reaction-diffusion equations are mathematical models used to describe certain physical phenomena. One of the most common descriptions is the spatial and temporal change of a concentration of a single or group of substances when spread out over space [60, 61].

Equation (1.10) describes the time dependent change in the substance concentration when only diffusion affects the system. However, chemical reactions that affect the concentration u also occurs in the system. Thus, the general equation for the concentration u change due to chemical reactions and diffusion is described as

$$\frac{\partial u}{\partial t} = D\nabla^2 u + R(u), \tag{1.11}$$

where $u = u(r, t)$ is the state variable vector that describes the concentration of a substance or a density of a population at the position $r \in R^n$ at time t. The first term on the right hand of equation (1.11) describes the diffusion, D being a diagonal diffusion coefficient matrix and ∇^2 the Laplace operator which acts on the vector u. In the other side, the function on second term $R(u)$ accounts for local reaction kinetics.

As discussed earlier, patterns in biological systems originate from highly nonlinear reactions. These reactions are important for the proper functioning of living organisms, from cells and tissues to organs. For example, despite the heterogeneity of the interior of the cell it is common to use homogeneous reaction diffusion models for the study of the polarization process in diverse types of cells [62, 63].

1.2.3 Phase Field Model

The use of a phase field is a well-established approach to dealing with problems of evolving domains/geometries without the need for explicitly tracking the domain boundaries, which has been exploited to tackle moving boundary problems of different kinds such as crack propagation [64], solidification [65], microstructure evolution [66] and fluid interface motion [67]. The role of a phase field variable is to define a surface between two different regions; to do this, the phase field gradually changes its value, see Figure 1.8. The temporal evolution of a phase field variable is described by partial differential equations where different kinds of forces (e.g, surface tension and active force) are considered and solved numerically. Despite the phenomenological character of phase field equations, based on thermodynamic and kinetic principles, the versatility of this approach has been used for modelling cell-shape evolution and locomotion [68, 69, 70, 71].

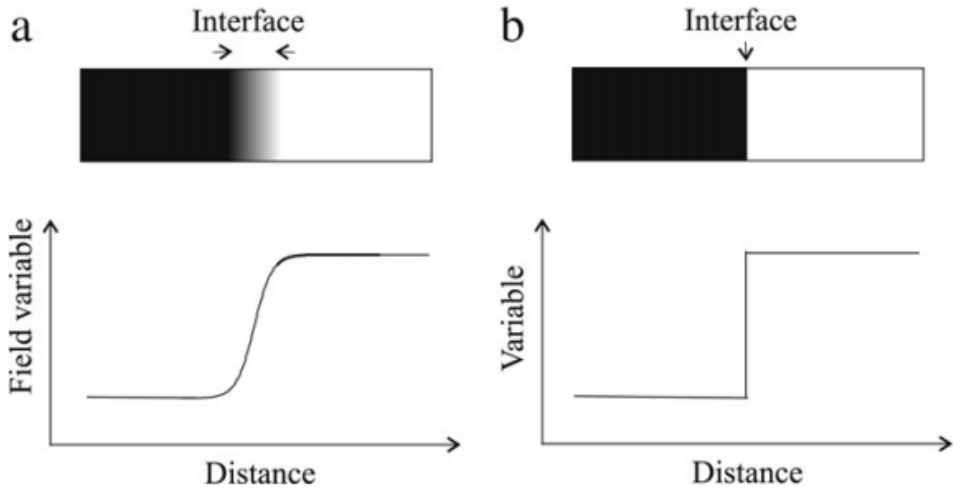

Figure 1.8: Different type interfaces of a phase field variable. a)Diffuse interface evolve. b) Sharp interface are discontinuous at the interface. Image taken from: [66].

There are several mathematical tools to simultaneously model the pattern formation process inside the cell and the dynamics of the cell border, which is required to obtain a full description of a crawling cell. One of the most commonly employed methods to model such a free-boundary problem is the introduction of an additional phase field, whose value is one inside and zero outside the cell and which keeps the no-flux boundary conditions while the borders are moving [72], in the limit of the sharp interface between the interior and the exterior of the cell [73]. The first attempts to employ phase field modeling to study cell locomotion where applied to keratocyte motility [68, 74, 75, 76] because the persistence of motion of these cells facilitates the implementation of the model. These models have also been extended to discuss, for example, the rotary motion of keratocytes [77] and the interactions among adjacent cells [78, 79].

Later, the use of the phase field was extended to model other generic properties of moving cells [80, 81] and, in particular, it has also been employed to describe the random motion of amoeboid cells, such as neutrophils or *D. discoideum*, which can be divided into diffuse and persistent migration de-

pending on the starvation level [82, 83]. The phase field approach has been employed to model the viscoelasticity of the cell [84, 85, 86] and the effect of biochemical waves in the interior of the cell [69], as well as wave-induced cytofission of cells [87]. The random motion of the cell is often modeled by a stochastic bistable process in combination with a phase field [88] to recover fluctuating displacements and shape deformations. Such a stochastic bistable model is able to capture the cell-to-cell variability observed in the motion patterns of amoeboid *D. discoideum* cells by tuning a single model parameter [88, 89, 90, 91].

1.3 Objectives of the work

The aim of this work can be divided into one general (GO) and six specific objectives (SO).

The general objective of the present work reads as follows:

GO1.- To describe spatiotemporal dynamics mimicking the amoeaba *Dictyostelium discoideum* by implementing and designing algorithms based on reaction-diffusion models coupled with an auxiliary phase field. To numerically integrate the models, the method of finite differences was used.

This general aim is addressed by the following list of specific objectives of this work:

SO1.- To extend the general bistable model described in [92] in order to reproduce common features from different phenotypes of moving cells (e.g., amoeboid, fan shape, and unstable).

SO2.- To enlarge the general bistable model to describe the collective mo-

tion of large populations of interacting amoeba by including repulsive interactions among cells.

SO3.- To include static objects with the purpose of reproducing confined cell motion, for example cells inside microchannels.

SO4.- To adapt previous results with alternative bistable and excitable biochemical reaction-diffusion models [51, 93] in one and two dimensions.

SO5.- To implement moving boundaries by the addition of a phase field model in order to couple the membrane shape with the biochemical reaction-diffusion models from SO4, with the intention of reproducing membrane deformation and subsequent motion of the synthetic cell.

SO6.- To increase the robustness of the bistable biochemical model [51] by incorporating a mass conservation constraint via the inclusion of a global feedback in the model generated in SO5.

1.4 Organization of the work

At this point it we are going to establish the line to follow regarding the structure of this work. Each of the following chapters will be organized as follows: first, there is a description of the problem to be studied, together with some references to previous studies that have been done in the field; second, the methodology used will be described; next the results obtained will be presented; and finally the results will be discussed.

In chapter 2 the methods that will be used for the development of this study are presented. We will describe a bistable generic mathematical model employing partial differential equations resembling the motility of

living cells. The non-linearities in the interior of the cell will be represented by reaction diffusion-equations together with stochastic processes. All this is coupled with an auxiliary dynamic phase field. Finally, the integration and numeric methods are considered at the end of the chapter.

As established in SO1 the model and methodology described in chapter 2 will be used; in chapter 3 it will be shown that with a bistable generic model it is possible to investigate different motility scenarios with distinct displacement mechanisms such as amoeboid and fan-shaped. At the end of the chapter a comparison between numerical simulations and live cell imaging experiments of motile Dictyostelium Discoideum cells under different developmental conditions is made.

In chapter 4, as proposed in SO2, a collection of interacting cells without confinement and their effects as patterns or cluster formation are studied. For this purpose, a modified version of the model in chapter 3 is used in which a term for repulsion among cells or external borders was included.

Following SO3, in chapter 5 the interactions of crawling cells in reduced spaces commonly known as microchannels are described, and their effects in the motility under those conditions are considered.

Results from a bistable and excitable model in chapters 6 and 7, respectively, are extended from one to two dimensions as set in SO4. Next, as defined in SO5, two dimensional results for both models are coupled to a dynamic phase field with the objective of mimicking cell locomotion.

In chapter 6, a bistable biochemical mathematical model based on the generation of Ras and pseudopod inducer patches is studied. According to SO6 a global feedback to keep mass conservation was added with the goal of increasing the robustness of the model.

Finally, in chapter 7 an alternative excitable biochemical model is analyzed. This model is composed of the coupling of Ras and P IP3 networks. The combination of the two networks represents the symmetry-breaking process before a cell polarizes and moves.

Chapter 2

Methods

Different types of cell motility will be investigated, based on a minimal model that couples a concentration field accounting for the complex biochemical reactions occurring in the interior of the cell to an auxiliary phase field describing the evolution of the cell shape. The model used here has been previously introduced in [88] and will be summarized below.

In what follows the dynamics of a generic activatory biochemical component at the substrate-attached cell-membrane will be considered. Thus, we restrict ourselves to an idealized 2D geometry. The phase field $\phi(x,t)$ smoothly varies between the values of $\phi = 1$ inside and $\phi = 0$ outside the cell, respectively. The phase field allows us to implicitly impose no-flux boundary conditions at the cell border, which is assumed to be where the phase field takes the value of $\phi = 0.5$. Following the work by Shao *et al.* [68], the phase field evolves according to the equation

$$\tau \frac{\partial \phi}{\partial t} = \gamma \left(\nabla^2 \phi - \frac{G'(\phi)}{\epsilon^2} \right) - \beta \left(\int \phi \, dA - A_0 \right) |\nabla \phi| + \alpha \, \phi \, c \, |\nabla \phi| \ , \quad (2.1)$$

where $G(\phi) = 18\,\phi^2\,(1-\phi)^2$ is a double well potential. The phase field

equation is the result of a force balance involving forces of different nature acting on the cell body. The terms with $|\nabla\phi|$ are restricted to the border of the cell, while the others affect the volume.

The first term on the right hand side of equation (2.1) corresponds to the surface energy of the cell membrane, where γ is the surface tension (note that value is obtained assuming a cell height of 0.15 μm [68]) and ϵ the mathematical definition of the width of the cell boundary.

The second term is a global constant that ensures that the cell's area is kept close to A_0.

The last term represents the active force related with the biochemical field $c(x,t)$ on the cell membrane. The parameters that control the impact of the area conservation constraint and the active force, β and α, respectively, are kept constant in the simulations. The term on the left hand side of equation (2.1) accounts for cell-substrate friction. More complete derivations of equation (2.1) can be found in [74, 88].

2.1 Phase field coupled to a generic bistable reaction-diffusion model for cell motion

Many aspects of cell motility such as cytoskeletal mechanics [94], intracellular signaling dynamics [40, 95], and membrane deformation [96] have been modeled using mathematical and computational methods. Cell polarity formation, which is a key feature of motility mechanisms to determine the front and back of the cell, often can be described by bistable dynamics. A reaction-diffusion system with bistable kinetics is thus a common choice to model intracellular polarity [97]. Bistable conditions of an intracellular dy-

namic process can be obtained with a mass-controlling mechanism between the cytosolic and membrane-attached concentrations of biochemical components [62, 98]. This may be relevant at different levels of the cytoskeleton, for example, when different forms of actin are involved [99, 100, 101] or at the level of the related signaling pathways, involving phospholipids and enzymes at the cell membrane [102, 103]. Cell polarity may also be imposed by an external chemical gradient [104, 105].

Cell polarization is implemented here by assuming noisy bistable dynamics resulting from a non-linear reaction-diffusion equation for the concentration $c(x,t)$. The biochemical field $c(x,t)$ represents a dimensionless generic concentration variable that accounts for different subcellular components that promote the growth of filamentous actin (F-actin) such as active Ras, PI3K and PIP_3 [106]. This is related to the intensity of the Lifeact-GFP marker for F-actin which is typically shown in the experiments.

Imaging experiments with *D. discoideum* typically show rich dynamical patterns in the cell cortex and at the cell membrane. The derivation of a detailed model that captures the full complexity of the underlying biochemical reactions is unfeasible. To overcome this difficulty in deriving a detailed model of the reactions inside the cell and aiming for mathematical simplicity, here it was taken a similar approach as in previous studies [62, 70, 88] and formulated a simple reaction-diffusion equation, where the non-linear reaction kinetics leading to bistability is modelled by a cubic polynomial in the variable $c(x,t)$. In addition, a term accounting for degradation of the biochemical component c was introduced. The equation reads

$$\frac{\partial(\phi c)}{\partial t} = \nabla\left(\phi D \nabla c\right) + \phi[k_a\, c\,(1-c)(c-\delta(c)) - \rho\, c] + \phi\,(1-\phi)\,\xi(x,t), \quad (2.2)$$

where k_a is the reaction rate, ρ the degradation rate, and D the diffusiv-

ity of the biochemical component. The last term on the right hand side introduces noise at the cell membrane, which allows us to account for the stochastic nature of the reaction-diffusion processes occurring within the cell. The noise intensity along with the reaction rate are key parameters in the model that allow the transition between different forms of cell motility. The stochastic variable $\xi(x,t)$ follows an Ornstein-Uhlembeck dynamics, described in the following stochastic partial differential equation

$$\frac{d\xi}{dt} = -k_\eta\,\xi + \eta\,, \tag{2.3}$$

where η is Gaussian white noise with zero mean average $\langle\eta\rangle = 0$ and a variance of $\langle\eta(x,t)\eta(x',t')\rangle = 2\sigma^2\delta(x-x')\delta(t-t')$.

The reaction-diffusion equation aims at reproducing the pattern activity on the substrate-attached cell membrane observed in the experiments. Control of the size of the patterns is important since the patterned area rarely covers the entire cell membrane. Previous experiments with giant *D. discoideum* cells revealed that, after a critical size is reached, wave patterns tend to modify their shape rather than actually growing into larger areas [107]. Therefore, dynamic control in the form of a global feedback on the parameter $\delta(c)$ is implemented. This affects the pattern dynamics and prevents the system from being covered completely by c depending on the value of C_0. The control term reads

$$\delta(c) = \delta_0 + M\left(\int \phi\, c\, dA - C_0\right)\,, \tag{2.4}$$

where the parameter C_0 represents the average area covered by component c. The control mechanism shown in equation (2.4) dynamically changes the value of the unstable fixed point of the system. This ensures that the amount of component c inside the cell is constant on average. There

is a clear dependence of the cell trajectories on the parameter C_0 in the numerical simulations.

2.2 Numerical solution of the model

Normally, reaction-diffusion equations are nonlinear. This lead to difficulty in finding an analytical solution and it is here where numerical simulations help. For example, a typical numerical method consists in approximate derivatives with finite differences.

2.2.1 Finite differences method

In one dimension the way to approach the first and second order spatial derivatives is given as:

$$\frac{\partial f}{\partial x} \approx \frac{f(x+\Delta x) - f(x-\Delta x)}{2\Delta x}, \tag{2.5}$$

$$\frac{\partial^2 f}{\partial x^2} \approx \frac{f(x+\Delta x) - f(x-\Delta x) - 2f(x)}{\Delta x^2}, \tag{2.6}$$

respectively, while for the case of a two dimensional lattice, the discretization expressions for the first order derivative read as:

$$\frac{\partial f}{\partial x} \approx \frac{f(x+\Delta x, y) - f(x, y)}{\Delta x}, \tag{2.7}$$

$$\frac{\partial f}{\partial y} \approx \frac{f(x, y+\Delta y) - f(x, y)}{\Delta y}, \tag{2.8}$$

and the second order derivatives are given by:

$$\frac{\partial^2 f}{\partial x^2} \approx \frac{f(x+\Delta x, y) - f(x-\Delta x, y) - 2f(x,y)}{\Delta x^2}, \tag{2.9}$$

$$\frac{\partial^2 f}{\partial y^2} \approx \frac{f(x, y+\Delta y) - f(x, y-\Delta y) - 2f(x,y)}{\Delta y^2}, \tag{2.10}$$

If $\Delta x = \Delta y$ equations (2.9) and (2.10) can be rewritten in the following form:

$$\nabla^2 f \approx \frac{f(x+\Delta x, y) - f(x-\Delta x, y) + f(x, y+\Delta x) - f(x, y-\Delta x) - 4f(x,y)}{\Delta x^2}. \tag{2.11}$$

The numeric derivative expressions of the form of equations (2.5)-(2.11) can be employed to solve ordinary differential equations. One of the most common methods for solving differential equations is the Euler method where a nonlinear equation of the form $\frac{dx}{dt} = F(x,t)$ is approached as follow:

$$x(t+\Delta t) = x(t) + \Delta t\,(F(x(t),t))\,. \tag{2.12}$$

.

2.2.2 Integration of Ornstein-Uhlenbeck process

Considering the following equation:

$$\frac{dx}{dt} = F(x(t)) + B\xi(t)\,, \tag{2.13}$$

where $F(x(t))$ is a function of the state x while B could represent a constant or a function that depends on the state of the system ($B = B(x)$).

One interesting question is to address what happens if the term $\xi(t)$ is a random noise. If B takes a constant value, equation (2.13) has an additive noise; on the other hand, if B represents a function of the state of the system $B = B(x)$, the equation has the presence of multiplicative noise. Expressions such as equation (2.13) are known as stochastic differential equations and are characterized by having one or more terms as a stochastic process [108]. Some of the most widely studied stochastic differential equations are the heat, wave and Schrödinger equations [109].

Normally this type of equation contains one variable representing pure random white noise, which is calculated as the derivative of Brownian motion or a Wiener process.

Trying to solve numerically equation (2.13) one can rewrite it as follow:

$$x(t + \Delta t) = x(t) + \Delta t F(x(t)) + B \int_t^{t+\Delta t} \xi(t')dt', \tag{2.14}$$

using the expression for the white noise $\xi(t)dt = dW(t)$, equation (2.14) goes to

$$x(t + \Delta t) = x(t) + \Delta t F(x(t)) + B \int_t^{t+\Delta t} dW(t'), \tag{2.15}$$

$$x(t+\Delta t) = x(t) + \Delta t F(x(t)) + B\sigma N(0,\Delta t), \tag{2.16}$$

$$x(t+\Delta t) = x(t) + \Delta t F(x(t)) + B\sigma\sqrt{\Delta t} N(0,1). \tag{2.17}$$

where σ is the standard deviation of the white noise, $\int_t^{t+\Delta t} dW(t') \approx \sigma N(0,\Delta t)$ and $N(0,\Delta t)$ is white noise with zero mean and variance Δt.

Equation (2.17) is an extension of the Euler method for ordinary differential equations to stochastic differential equations. This is known as the Euler-Maruyama method and is useful to approximate a numeric solution of a stochastic differential equation [110].

Returning to the stochastic differential equation (2.3) which describes an Ornstein-Uhlenbeck noise dynamics, it was numerically solved as follows:

$$\xi(t+\Delta t) = \xi(t)\exp(-k_\eta \Delta t) + \left((\frac{\epsilon}{k_\eta})(1 - exp(-2k_\eta \Delta t))\right)^{1/2} \eta, \tag{2.18}$$

where k_η and ϵ are the correlation time and the noise amplitude of η [111].

In the following sections, different cell motility modes will be studied and analyzed. The transitions between these modes are obtained by varying three parameters: the noise intensity, the average membrane coverage with the activatory component c, and the activity rate of the biochemical field. In general, the bistable kinetics of c will drive the formation of patches of high concentration of c on a background of low c concentration. The coherent effects of these patches on directed cell locomotion will be disturbed and interrupted by the impact of noise, which will favor nucleation events and the formation of new patches in other regions of the membrane.

Therefore, the dynamics of the model can be qualitatively understood as a competition between the coordinated effects of pattern formation and the randomizing impact of noise on cell locomotion.

Chapter 3

Modeling cell crawling dynamics: from amoeboid to fan-shape motion

3.1 Introduction

The biochemical and biophysical mechanisms involved in cell motility have been extensively studied during the past years. They are among the most intriguing problems in cell biology, ranging from single cells to multicellular organisms. As mentioned in previous chapters, before the cell begins to move, it needs to polarize, which means that has to define a front and a back to specify an axis of propagation [112]. It sets the direction in which protrusions are formed that drive the cell forward. Cell locomotion has been extensively studied using keratocytes, which move in a highly persistent fashion and adopt a characteristic fan-like shape [113]. Also neutrophils have been intensely investigated. They display a less persistent movement with more frequent random changes in direction that is known

as amoeboid motility [114]. Here is where the well-established model of the social amoeba *Dictyostelium discoideum* (*D. discoideium*) system is used to study actin-driven motility in eukaryotic cells is [115]. The cells of this highly motile single-celled microorganism typically display pseudopod-based amoeboid motility but also other forms, such as blebbing motility or keratocyte-like behavior have been observed.

However, *D. discoideum* cells are also known to show a more diverse spectrum of motility modes, for example when certain genes are knocked out, when phosphoinositide levels are artificially altered, or under specific developmental conditions. This includes a phenotype which is reminiscent of keratocyte motility, where the cell adopts a fan-like shape and moves persistently, perpendicular to the elongated axis of the cell body – the so-called fan-shaped phenotype – and a form where cells adopt a pancake-like shape, moving erratically without a clear direction of polarization [91, 116, 117].

In this chapter is introduced a systematic analysis of a previously introduced model that is based on a stochastic bistable reaction-diffusion system in combination with a dynamic phase field [88]. Such phenomenological model may provide a better understanding of how to relate the experimental parameters to specific cellular behaviors, because cell-to-cell variability often masks such relation. Along with the model, experimental data of a non-axenic *D. discoideum* wildtype cell line (DdB) that carries a knockout of the RasGAP homologue NF1 (DdB NF1 null cells) is analyzed. In this cell line, amoeboid and fan-shaped cells are observed, depending on the developmental conditions. A detailed comparison of the experimental data to simulations of the stochastic bistable phase field model is presented. By tuning the intensity of the noise and the area covered by the bistable field, the model simulations recover similar motility phenotypes as observed in experiments, ranging from highly persistent fan-shaped cells to standard

amoeboid motion. Furthermore, the simulations predict intermediate unstable states and also a transition from straight to rotary motion of the fan-shaped cells. These forms of motility that have so far been neglected in *D. discoideum*, were also observed in the experimental data and are systematically studied in the framework of a mathematical model described below with more detail.

3.2 Experimental Methods

All experiments were performed in the lab of the Biophysics group in the University of Potsdam with non-axenic *D. discoideum* DdB NF1 KO cells [118], which were cultivated in 10 cm dishes with Sorensen's buffer (8 g KH_2PO_4, 1.16 g Na_2HPO_4, pH 6.0) supplemented with 50 μM $MgCl_2$, 50 μM $CaCl_2$ and *Klebsiella aerogenes* at an OD_{600} of 2. The cells expressed Lifeact-GFP via the episomal plasmid SF99, which is based on a new set of vectors for gene expression in non-axenic *D. discoideum* strains [119]. Plasmids were transformed as described before [119] with an ECM2001 electroporator using three square wave pulses of 500 V for 30 ms in electroporation cuvettes with a gap of 1 mm. G418 (5 μg/ml) and Hygromycin (33 μg/ml) were used as selection markers.

The phenotype of DdB NF1 KO cells differs between individual cells of a population and especially between different developmental stages. When cultivated in buffer supplemented with bacteria, cells are in the vegetative state and the predominant phenotype is amoeboid with very little movement due to the abundance of bacteria. After several hours of starvation, cell enter the developed state and the probability to observe a fan-shaped phenotype is increased. Preparation of the cells for experiments therefore

differed between experiments. Cells were washed to remove the bacteria and (i) suspended in Sörensen's Buffer immediately after washing to obtain mainly amoeboid cells with high motility or (ii) starved for 3-6 hours to obtain a high percentage of fan-shaped cells. After starvation, cells were seeded in microscopy dishes at low density for imaging. Usually in the beginning of an experiment, many cells showed the amoeboid or the intermediate phenotype with regular switches from amoeboid to fan-shaped motility and vice versa. The percentage of fan-shaped cells increased over time and the fan-shaped phenotype became more stable. An increase in the number of fan-shaped cells during development has also been described for the D. discoideum Ax2 AmiB knockout strain [116]. Note however, that the effects of cell development on the phenotype of DdB NF1 KO cells showed a high day-to-day variability and best results were accomplished with fresh *K. aerogenes* cells. The cells were transferred to a 35 mm glass bottom microscopy dish (FluoroDish, World Precision Instrumnets) and diluted to a concentration enabling imaging of single cells. For imaging an LSM 780 (Zeiss, Jena) with a 488 nm argon laser and a 63x or a 40x oil objective lens were used.

3.3 Computational results of the motility scenarios obtained by the bistable model

A systematic study of the model described in the previous section will be shown below.

Using numeric methods described in the previous section, Eqs. 2.1-2.4 were integrated on a square domain of 300×300 pixels with periodic boundary conditions using standard finite differences. The pixel size is given by

$\Delta x = \Delta y = 0.15\,\mu$m and the integration time step is $\Delta t = 0.002\,$s. The values and definitions of the parameters of the model can be found in Table A.1. Cell trajectories and velocities were obtained by finding and tracking the center of mass of cells from the numerical simulations.

By modifying the values of the biochemical reaction rate k_a, the intracellular area covered by the concentration c, defined as C_0, and the noise strength σ, a wide diverse set of cell shapes, trajectories, and speeds were obtained. An overview of the studied cases is presented in Figure 1, where different cell shapes and average speeds are shown in the plane spanned by the parameters σ and C_0. Four different types of motility with distinct shapes and trajectories were identified: Amoeboid cells, characterized by a motion parallel to the elongation axis, fan-shaped cells that move perpendicular to the elongation axis, intermediate states that combine features of both amoeboid and fan-shaped types, and oscillatory cells, where the concentration c is almost homogeneously distributed inside the cell with only small fluctuations at the border.

The transitions between the four cell types, summarized in Figure 3.1, are presented in more detail in Figure 3.2, where cell shapes are shown for $k_a = 2s^{-1}$ and $k_a = 5s^{-1}$ separately as a function of the parameter C_0, which is changed in smaller increments here. In both diagrams, the simulations in the left top panels show cell types that mimic the vegetative and starving states of *D. discoideum*, analyzed in more detail in [88]. The right bottom panels in Figure 3.2 A and B correspond to stable fan-shaped and rotating fan-shaped cells, respectively, which are shapes related to particular mutations of *D. discoideum* [116, 117]. In between these two limits, different dynamical regimes have been obtained during the computational study of the model, some of which have been also observed in the experiments with *D. discoideum*, as it is described below.

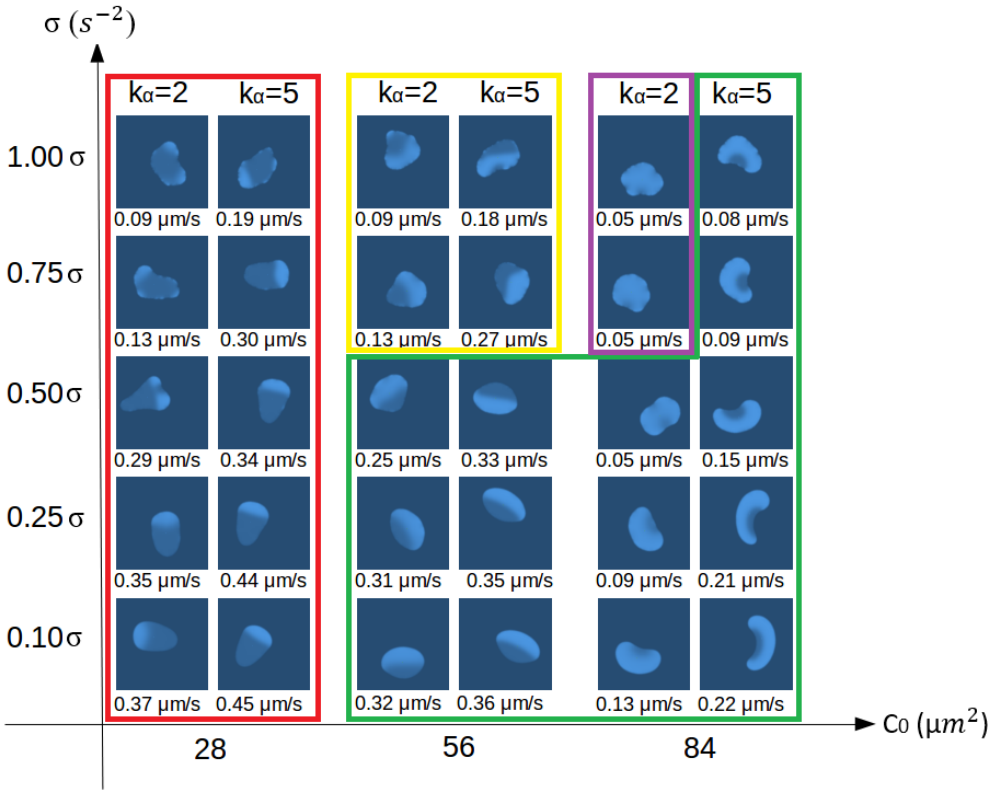

Figure 3.1: Phase diagram of the cell shapes obtained from the model and their respective average speeds for different values of the spatio-temporal noise, the reaction rate, and the maximum area coverage of the concentration c. The intracellular concentration c is proportional to the intensity of sky blue color. Cell speed was computed as the sum of the velocities at each time step divided by the number of time steps. Colored boxes classify cells into four types: Amoeboid cells inside the red box, fan-shaped and similar cases inside the green box, intermittent cases at the transition from the amoeboid to the fan-shaped regime inside the yellow box, and oscillatory cells inside the purple box.

3.3.1 Amoeboid motion

When C_0 was set to $C_0 = 28\ \mu m^2$, the biochemical component c roughly occupies one quarter of the total cell area, fixed at 113 μm^2 (corresponding to a circular cell with radius 6 μm). Under these conditions, the concentration c accumulates in the front part of the cell reminiscent of the typical amoeboid shape of *D. discoideum* cells. In this scenario, one can observe different trajectories depending on the noise intensity. A large noise intensity translates into slow and random cell motion, whereas low intensity

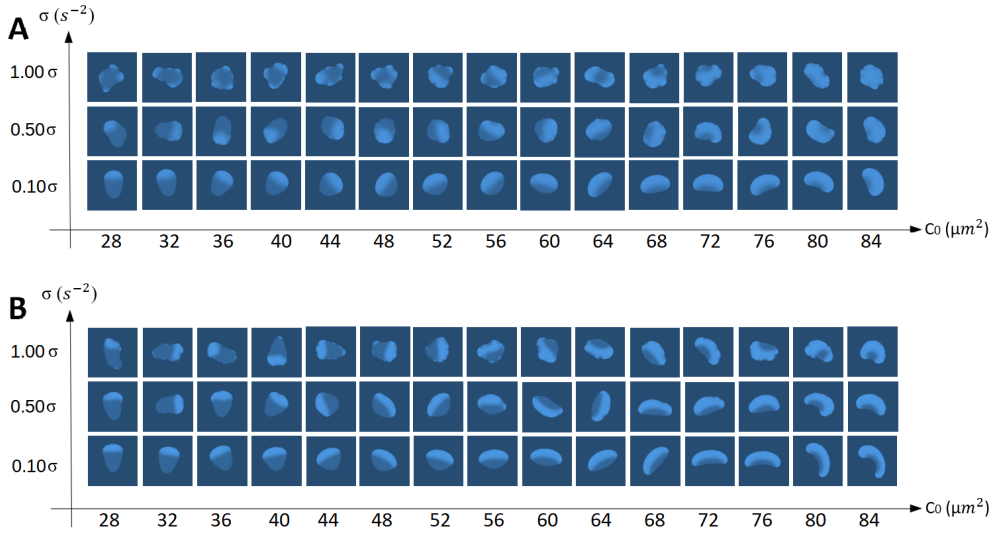

Figure 3.2: Phase diagrams of the cell shape obtained from the model simulations when varying area coverage and noise intensity. The computational cells are obtained for $k_a = 2s^{-1}$ (A) and $k_a = 5s^{-1}$ (B). The intracellular concentration c is proportional to the intensity of sky blue color.

leads to faster and much more persistent motion.

A comparison between the dynamics of living *D. discoideum* cells under amoeboid conditions and cell dynamics generated by the model is shown in Figure 3.3. The numerical simulations shown in Figure 3.3A and C correspond to low values of C_0 and a noise intensity of 100% of the total given in Table 1. Figure 3.3C, showing trajectories for $k_a = 2s^{-1}$ and $k_a = 5s^{-1}$, demonstrates that the parameter k_a controls cell polarization [88]. A value of $k_a = 2s^{-1}$ induces a diffuse trajectory in a small area of space and a random appearance of protrusions formed by fluctuating amounts of concentration c along the cell membrane. For $k_a = 5s^{-1}$ the cell explores larger areas due to a continuous and more stable accumulation of c in one region of the membrane that sets in the direction of motion (see Figure 3.3A). A representative sequence of snapshots of an experimental observation of amoeboid motion of a *D. discoideum* cell is shown in Figure 3.3B, where the accumulation of actin is clearly appearing in the cell front. In addition, it was presented some examples of individual experimentally

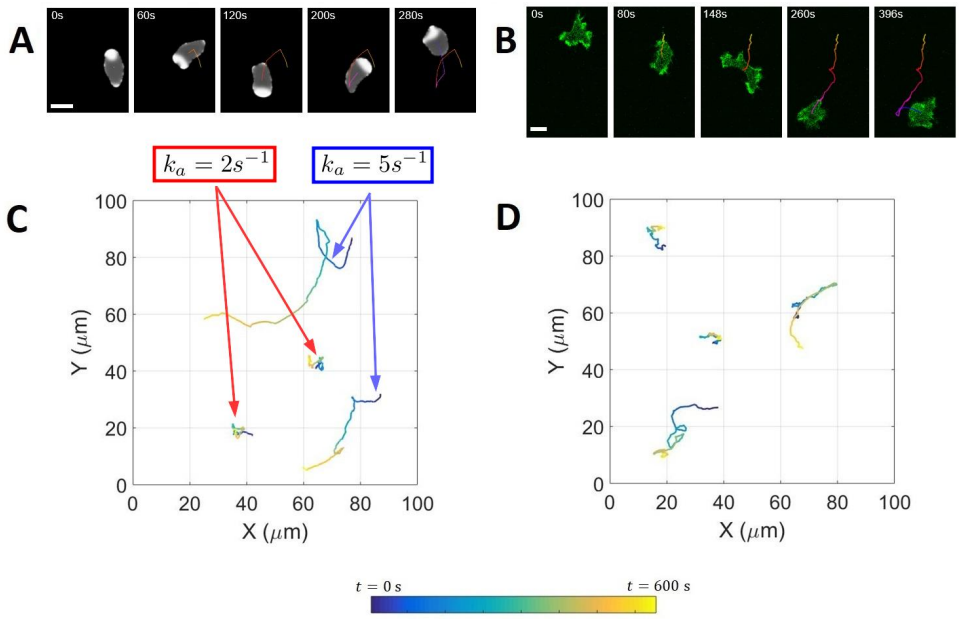

Figure 3.3: Numerical and experimental results for amoeboid motion. (A) Sequence of several snapshots of a numerical simulation with $C_0 = 28\mu m^2$ and $k_a = 5s^{-1}$. (B) Sequence of several snapshots of a vegetative DdB NF1 KO cell showing the amoeboid phenotype. (C) Example cell trajectories tracked from four simulations over 600 s (two simulations with $k_a = 2s^{-1}$ and two with $k_a = 5s^{-1}$) It is important to mention that the two small trajectories correspond to $k_a = 2s^{-1}$, while the two larger trajectories to $k_a = 5s^{-1}$. Both cases also with $C_0 = 28\mu m^2$, (D) Examples of cell trajectories tracked from four vegetative DdB NF1 KO cells showing the amoeboid phenotype in experiments over 600 s.

recorded cell trajectories that cover the behavioral diversity of amoeboid *D. discoideum* cells Figure 3.3D.

3.3.2 Intermediate dynamics

By increasing the parameter C_0 to 56 μm^2, which corresponds to half of the total area of the cell covered by the biochemical species c, and maintaining the noise intensity between 75% and 100% of the total given in Table 1, it was found a different motile behavior in the model simulations. Under theses conditions, the results of the numerical simulations resemble the amoeboid shapes described in the previous section, however the re-

peated appearance of an additional large protrusion strongly modifies the trajectories of the simulated cells, see Figure 3.4A. Initially, the amount of c is concentrated in one region at the cell border, clearly defining a leading edge. From time to time, a part of the total amount of c changes position at the cell border thus triggering an instability of the initial leading edge. This drives the formation of a new protrusion, where eventually most of the total amount of c will accumulate and define a new cell front. In Figure 3.4B, it is shown an example of similar intermittent behavior that was observed in the experiments with *D. discoideum* cells which frequently switch from amoeboid to fan-shaped motility and vice versa. Figure 3.4C, where is present a comparison between an experimental trajectory and three trajectories obtained from numerical simulations, demonstrates how this dynamics generates trajectories with abrupt changes in direction.

By further increasing the parameter C_0 to 84 μm^2, corresponding to 75% of the total area of the cell covered by concentration c, another distinct behavior is obtained in the numerical simulations, see the purple box in Figure 3.1. Keeping $k_a = 2s^{-1}$ and a noise intensity similar to the previous case, an oscillatory behavior of the cell border is observed due to saturation of c inside the cell. Noise-driven small displacements and a *circular* cell shape characterize this regime. It resembles previous experimental observations of a so-called pancake phenotype [120].

3.3.3 Fan-shaped motion

For the values of C_0 employed in the previous section but low noise intensity, the shape of the numerically obtained cells becomes more elongated perpendicular to the direction of motion than parallel to the direction of motion of the cell. Moreover, their elongated shape is stable over time,

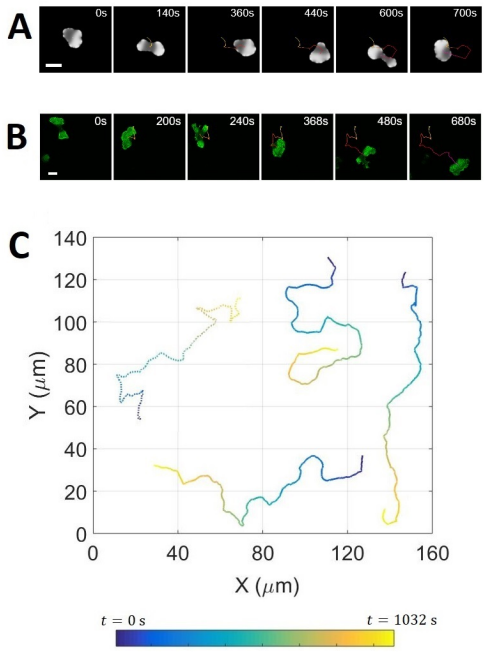

Figure 3.4: Numerical and experimental results for the intermediate unstable case (A). Sequence of six snapshots of a numerical simulation with $C_0 = 56\mu m^2$, $k_a = 5s^{-1}$. (B) Sequence of snapshots of a DdB NF1 KO cell starved for 4 hours prior to imaging, showing the intermediate phenotype. (C) Comparison between the trajectories of the center of mass of three numerical simulations (solid lines) and a trajectory of the center of mass of the DdB NF1 KO cell shown in B (dotted line). In all four cases, cells were tracked over $1032s$.

and they move in a highly persistent fashion. Together these features characterize the so-called fan-shaped motion of *D. discoideum* cells [117]. The overall appearance and motion characteristic of fan-shaped cells share many similarities with keratocytes, even though the internal organization of the motility apparatus is clearly different.

For $C_0 = 56\,\mu m^2$, corresponding to a concentration c covering half of the total cell area, and a noise intensity that is reduced to 50% or less of its maximal value, a rounded elongated shape, reminiscent of a keratocytes, is observed in the numerical simulations, see for example the results in Figure 3.1. The trajectories are straight and persistent for lower noise intensities and become more erratic for high noise levels.

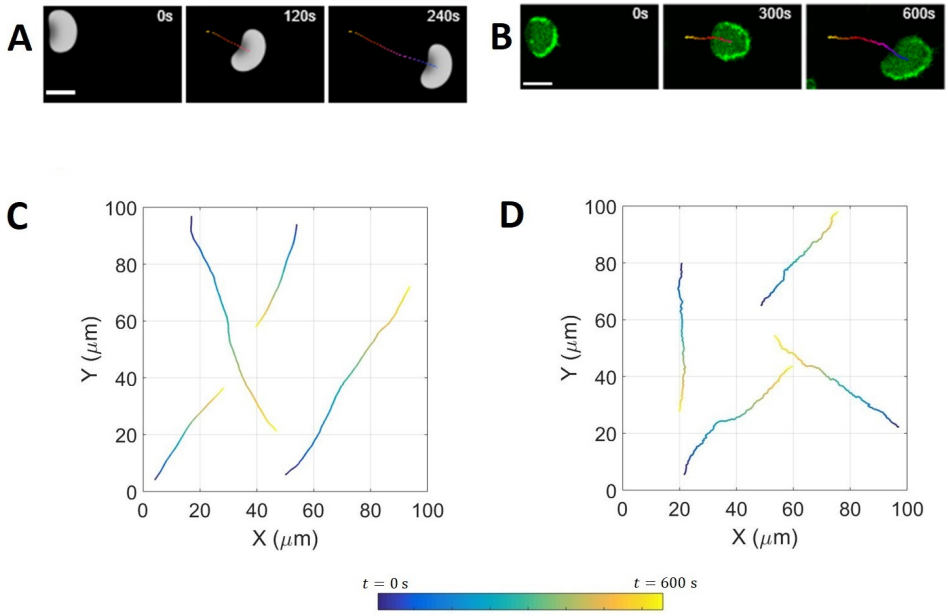

Figure 3.5: Numerical and experimental results for fan-shaped motility. (A) Sequence of three snapshots taken from a numerical simulation of the computed cell with parameter values $C_0 = 84\mu m^2$, $k_a = 2s^{-1}$ and noise intensity set to 10 percent. (B) Snapshots of a DdB NF1 KO cell starved for 4 hours prior to imaging, showing the fan-shaped phenotype. (C) Four examples of trajectories of the center of mass of numerically simulated fan-shaped cells tracked over 600 s. (D) Four trajectories of the center of mass of DdB NF1 KO cells starved for 4 hours prior to imaging, showing the fan-shaped phenotype tracked over 600 s in experiments.

By further increasing the covered area to $C_0 = 84\,\mu m^2$, similar fan-shaped cells were recovered. For $k_a = 2s^{-1}$ the simulation produces rounded cell shapes that move at a reduced speed in a highly random fashion. Comparing Figure 3.5A and B reveals the qualitative similarities between fan-shaped cells obtained from simulations under these conditions and the experimentally observed dynamics of fan-shaped *D. discoideum* cells. The model satisfactorily reproduces the experimental features of the cell motion. The four different realizations of trajectories, generated in numerical simulations and presented in Figure 3.5C, display a similar persistent motion as the straight cell trajectories observed in experiments, see Figure 3.5D. These trajectories resemble the trajectories of fan-shaped cells with $C_0 = 56\mu m^2$ and intermediate noise intensity as discussed previously.

Thus, depending on the value of the reaction rate and the noise intensity, it can be seen the remarkable differences between cell shapes and trajectories.

3.3.4 Rotational trajectories of fan-shaped cells

Numerical simulations with $C_0 = 84\mu m^2$ and $k_a = 5s^{-1}$ produce fan-shaped cells with a more elongated and curved shape. Depending on the noise intensity, different scenarios are obtained ranging from irregular shapes and trajectories at high levels of noise to regular shapes and circular trajectories for lower noise levels (see Figure 3.1). Under these conditions the trajectories may also reveal rotational dynamics. In Figure 3.6A and B, it is shown some representative examples of rotational dynamics observed in a simulation and in an experiment, respectively, finding a qualitative similarity between them. The corresponding trajectories are displayed in Figure 3.6C for comparison, along with a third trajectory of another simulation. Despite the differences in radius and frequency of rotation between simulations and experiment, the main characteristics of a periodic rotary motion are reproduced. Note that the concentration patterns inside the simulated cells resemble a half-moon shape, which is typical for fan-shaped cells with both straight and rotational trajectories.

The transition from straight to rotational motion for different values of C_0 and k_a is shown in a phase diagram in Figure 3.7. The noise intensity was kept constant at 10% in all cases. For low values of C_0 the trajectories of the simulated cells are straight and only sometimes exhibit a slight curvature, depending on the realization and the parameter values. With increasing parameter C_0, irregular trajectories are observed combining straight pieces with rapid rotations giving rise to a highly erratic motion. For values of C_0 between $80\mu m^2$ and $90\mu m^2$ and k_a larger than $3s^{-1}$, the simulations

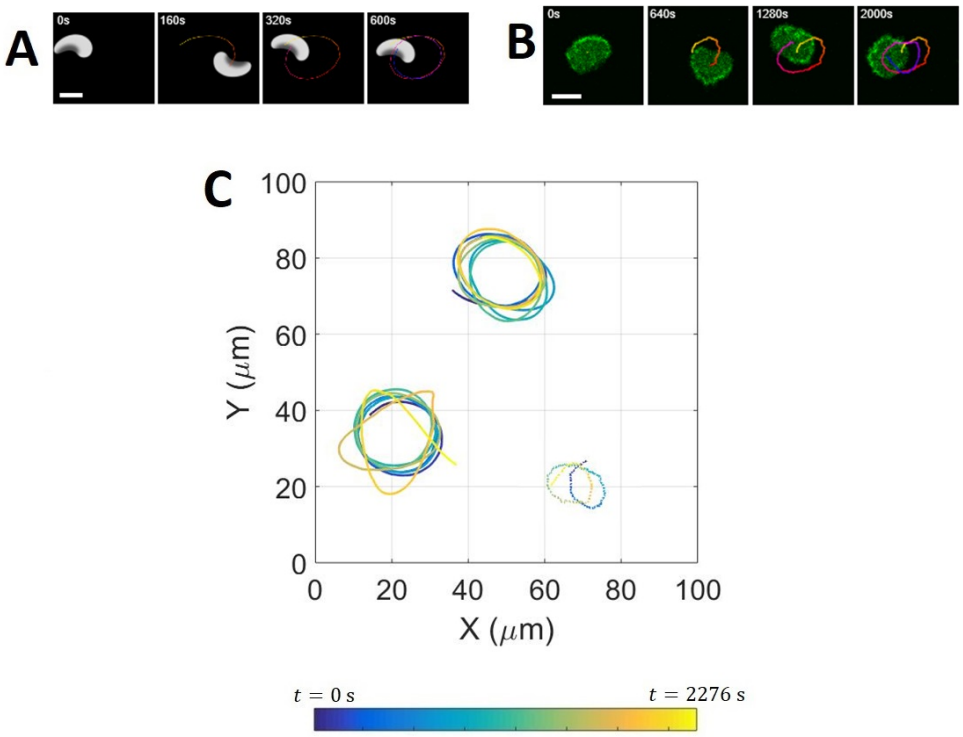

Figure 3.6: Numerical and experimental results for the rotational fan-shaped case. (A) Sequence of four snapshots obtained in the numerical simulations for $C_0 = 84\mu m^2$, $k_a = 5s^{-1}$ and noise intensity set to 10 percent. (B) Sequence of snapshots of a DdB NF1 KO cell starved for 5 hours prior to imaging, showing a fan-shaped cell with rotational movement. (C) Comparison of the trajectories of two simulations (solid lines) and one experimental realization (dotted line). The three lines correspond to trajectories tracked over more than $2000s$.

produce rotating cells as shown in Figure 3.6. For even higher values of C_0, after a small region with curved trajectories, the cell surface is almost saturated with the concentration c, and due to the low noise intensity, no significant net motion is observed.

Thus, it was found that rotational trajectories arise for specific combination of the reaction rate and the area coverage, and that they are favoured by low values of the noise intensity. Finally, an analysis was made to investigate if rotational trajectories can be induced by other factors. In Figure 3.8, is displayed a trajectory phase diagram spanned by the diffusion coefficient

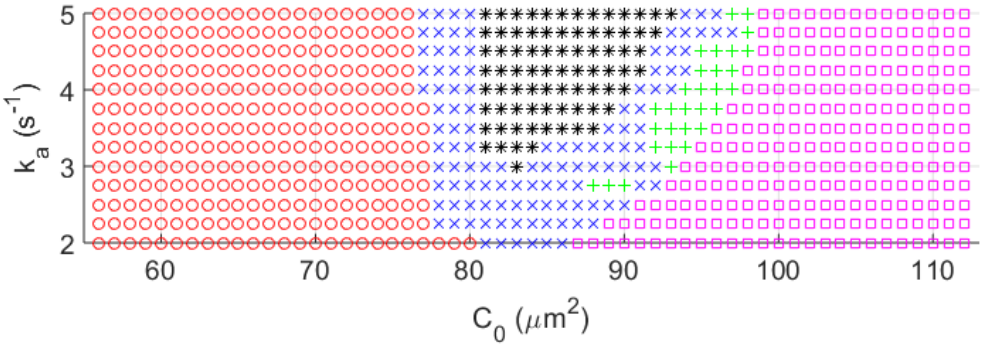

Figure 3.7: Phase diagram representing the entire range of different dynamics obtained from the model at low noise intensity and as a function of the reaction rate k_a versus the maximum area coverage C_0. Red circles represent trajectories that combine straight and curvature paths (fan-shaped cells). Blue crosses indicate irregular circling trajectories. Black dots show the region where regular circular trajectories are found. Green marks represent curved paths. Pink squares represent trajectories of almost stationary cells (pancakes). The noise intensity was set to 10%.

(D) and the surface tension (γ). The simulations indicate that rotational modes giving rise to circular trajectories are obtained by increasing the diffusion coefficient and by reducing the surface tension. This analysis agrees with the results obtained with a similar model for keratocyte dynamics described in [70].

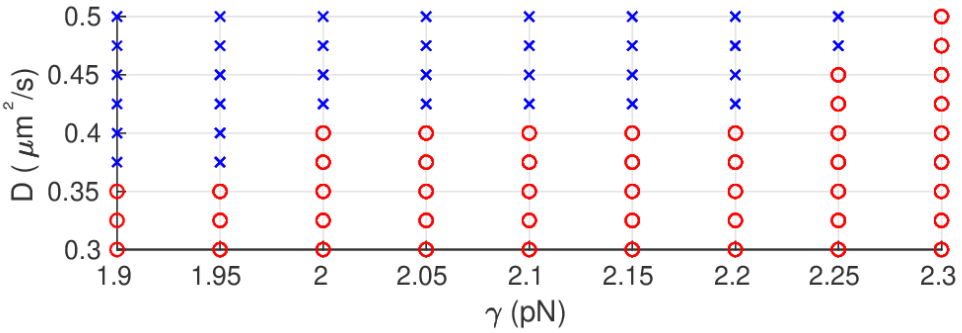

Figure 3.8: Phase diagram in the plane spanned by the diffusion coefficient (D) and the surface tension (γ) of the numerical simulations of fan-shaped cells with straight and circular trajectories corresponding, respectively, to red circles and blue crosses. Parameter values are: reaction rate $k_a = 5s^{-1}$, coverage area $C_0 = 84\mu m^2$, and a low level of noise intensity (10%).

3.4 Cell shapes and velocities in numerical simulations are comparable to experimental values

As described in the previous sections, shapes and trajectories of the cells vary strongly from one case to another. Amoeboid cells produce fluctuating displacements, fan-shaped cells exhibit also persistent and rotational motion. Finally, an intermediate case between amoeboid and fan-shaped phenotypes produces motion with characteristic features of both cases. The great majority of shapes and dynamics have also been observed in experiments, and a good qualitative agreement between experimental and numerical results was found.

In this section a more quantitative comparison between the experimental and the numerical results will be perform. A definition of an index will be helpful to clearly differentiates the amoeboid and fan-shaped cells and with this permit to characterize the transition between both cases. There are several indices that are commonly used in the studies of cell migration [121], such as the directionality ratio, the mean square displacement (MSD), and the directional autocorrelation. Here, the results of computing the directionality ratio to characterize the transition between amoeboid and fan-shape will be shown. Directionality is defined as the distance between the starting point and the endpoint of the cell trajectory, divided by the length of the real trajectory. Mathematically is defined as follows:

$$DR = \frac{\left|\vec{X_N} - \vec{X_0}\right|}{\sum_{n=0}^{N-1} \left|\vec{X_{n+1}} - \vec{X_n}\right|}, \tag{3.1}$$

where X_0 and X_N are the initial and final positions, respectively.

This ratio is close to 1 for a straight trajectory and close to 0 for a highly curved trajectory.

In the following results DR was computed for every Δt using the positions of the cell trajectories. First, it was made a comparison for a set of simulations corresponding to vegetative amoeboid cells ($k_a = 2s^{-1}$), which produce low values of the directionality and low velocities because of their random dynamics. Here, the relation between random motion and velocity can be interpreted as follows. A low noise intensity or large activity rate will lead to less nucleation events of new patches of c at the membrane, favoring stable movement in one particular direction which will result in higher velocities. On the contrary, a high noise or small activity rate will generate more nucleation events at different positions of the membrane, that will compete with each other, thus pushing the cell membrane in different directions, resulting in lower instantaneous velocities.

Second, a set of simulations corresponding to starvation-developed amoeboid cells ($k_a = 5s^{-1}$) is considered, which produce intermediate values of the directionality ratio because of their more persistent motion. Finally, it was analyzed a set of fan-shaped cells, which produce large directionality ratios because of their highly persistent movement. All these results are presented in Figure 3.9A, where it can be seen that the three types of cells are located in different regions of the parameter space.

The numerical results of the directionality ratio are in good agreement with the experimental measurements of this quantity, see Figure 3.9B, where the experimental data is plotted for a similar amount of cells. Fan-shaped cells in both cases have large directionality ratios due to their persistent motion. The set of amoeboid cells naturally divides into two subsets: one with low

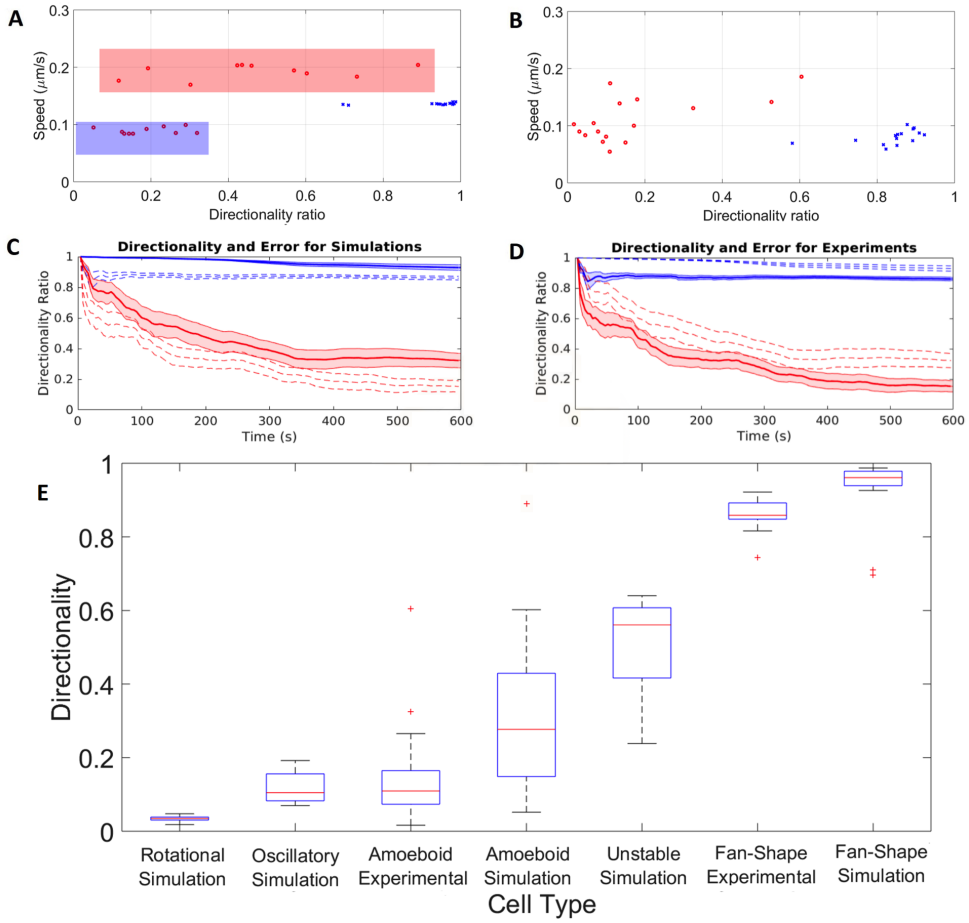

Figure 3.9: Directionality ratio from simulations and experiments over $600s$. (A) Cell speed versus directionality ratio obtained from numerical simulations of a sample of 20 amoeboid cells (red circles): 10 cells corresponding to $k_a = 2$, $C_0 = 28\mu m^2$, and 100% noise intensity (blue shaded area) and 10 corresponding to $k_a = 5$, $C_0 = 28\mu m^2$, and 100% noise intensity (red shaded area); and 15 fan-shaped cells (blue crosses). (B) Cell speed versus directionality ratio obtained from experiments with a sample of 16 amoeboid cells (red circles) and 15 fan shape cells (blue crosses) . (C) The mean value of the directionality ratio and standard error is plotted over time for amoeboid (red solid lines) and fan-shaped (blue solid lines) cells obtained from numerical simulations. Experiments curves from panel (D) are shown as dotted lines. (D) The mean value of the directionality ratio and standard error is plotted over time for amoeboid (red solid lines) and fan-shaped (blue solid lines) cells obtained from experiments. Simulation curves from panel (C) are shown as dotted lines. (E) Box plot of the directionality ratio for the data of several simulations and experiments over $600s$.

directionality ratios and low speeds and the other one with larger directionality ratios (although lower than in the fan-shaped cases) and speeds spreading over a wide range. In the numerical simulations, equivalent sub-

sets by changing the parameter k_a were produced.

Further similarities between the numerical results and the experimental realizations are found when comparing panels C and D in Figure 3.9. Here, the average of the directionality ratio over time with their respective errors for the amoeboid and the fan-shaped cells are shown for the numerical simulations in Figure 3.9C and the experimental recordings in Figure 3.9D. It is important to mention that for a better comparison it was included experiments curves from panel D in C and curves from panel C in D, in both cases as dotted lines and also with their respective errors. The good agreement between the two cases is remarkable although a systematic slight decrease of the directionality ratio appears in the experimental case, which may be related to the more noisy dynamics of the cell outline in the experimental measurements.

In Figure 3.9E it is displayed the directionality ratio for several cases obtained in the simulations and for the two experimental cases discussed above. A comparison of the directionality ratios was made in a box plot representation for the different cases. The first observation is that the circular motion of fan-shaped cells gives rise to the smallest value of the directionality ratio as expected, because the motion is confined to a small region of space. The second observation is that intermediate cases, discussed in the previous sections, give rise also to intermediate values of the directionality ratio. The largest directionality ratios are observed for the stable fan-shaped cells. Note that it was not taken into account other experimental cases because of the low number of recordings available in some of the experiments.

Finally, due to the cell shape diversity in experiments and simulations it was also analyzed the shape in a quantitative way. Computing quanti-

ties such as aspect ratio, ellipticity, or circularity are commonly computed when comparing cell shapes. There exist some earlier works, where cell morphology has been analyzed [122, 123, 124, 125]. This work focused on the circularity measure, which quantifies how closely the shape of a marked region approaches that of a circle. Circularity can be valued between 0 and 1, where 1 represents the value of a perfect circle. Mathematically the circularity is defined as follows: $CR = \frac{4\pi A}{P^2}$, where A is the area and P is the perimeter of the cell. With the use of the images of amoeboid and fan-shaped cells obtained from simulations and experiments the value of the circularity was calculated in each frame along the trajectories of the cells.

In Figure 3.10 it is shown a box plot representing the circularity ratio for the cases mentioned above. Here one can see the tendency of fan-shape cells to oscillate around values close to 1 due to their rounder shape. On the other hand, amoeboid cells present a larger variation in the value of their circularity parameter because of their irregular fluctuating shape. From the results it is also noticeable the good agreement between simulations and experiments for both scenarios. Just a small difference is marked in the fan-shaped case, where it was obtained a larger amount of outliers in the analysis of the experimental data.

3.5 Discussion

This section studied a mathematical model that consist of biochemical dynamics in the form of a bistable reaction-diffusion equation including a noise description based on an Ornstein-Uhlenbeck process. The biochemical dynamics is coupled to a phase field to account for the deformable cell

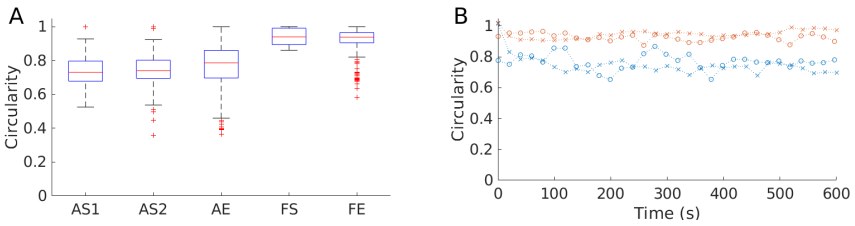

Figure 3.10: (A) Circularity box plot representation of amoeboid and fan-shaped cells from simulations and experiments. Values of circularity for the results of 11 simulations and 10 experiments are shown: amoeboid simulation $k_a = 2s^{-1}$ (AS1, n=3), amoeboid simulation $k_a = 5s^{-1}$ (AS2, n=3), and fan-shaped simulations (FS, n=5), amoeboid experiments (AE, n=5), and fan-shaped experiments (FE, n=5). (B) Represents the mean value of circularity over time for the studied cases. Amoeboid and fan-shape simulations are represented in blue and red crosses, repectively. Red and blue circles corresponds to experiments of amoeboid and fan-shape cell, respectively. The time for all the trajectories is $600s$.

border. The model was previously introduced in [88] to characterize the dynamics of vegetative and starvation-developed amoeboid *D. discoideum* cells. In that case, it was found a good agreement between the cell shape evolution, the intracelullar patterns, and the center of mass movement.

Until now, it was systematically explored the entire relevant range of the parameter space and qualitatively reproduced different motility regimes observed in *D. discoideum* cells. The phase diagram of the model was explored by changing parameters such as the noise strength, the coverage area, and the rate responsible for cell polarization, giving rise to a series of different motility scenarios as presented above. The numerical results reproduced the dynamics of *D. discoideum* cells, which were difficult to catalog for the experimentalists. In general, the comparison of trajectories, cell shapes, and cell speeds between numerical simulations of the model and experimental data showed good agreement.

The behavior of the model critically depends on the choice of the model parameters. Together with noise, realistic dynamics of intracellular patterns and cell shape changes are produced, when correct characteristic temporal

scales are used. The parameter C_0 corresponds to the area covered by the biochemical component c. It takes into account membrane deformations due to local accumulation of the biochemical component and, together with the reaction rate, reproduce variations in cell speed and persistence of motion.

The model shows similarities to the bistable reaction-diffusion model coupled to a phase field described in [70], where the motion of keratocytes is investigated. In particular, a systematic study of the transition between straight and circular motion of cells moving in a keratocyte-like fashion, equivalent to the fan-shaped cells, was done: a high tension tends to stabilize the cell motion to a straight trajectory, whereas large diffusion coefficients or small velocities tend to push the cell towards rotation [70]. In the study presented here, it was investigated the connection of keratocyte-like behavior and amoeboid motility, apparently associated to different mechanisms and cell types. Also, it was studied the transition between the persistent fan-shaped phenotype (keratocyte-like) and the amoeboid case, also showing intermediate dynamics and to directly compared the model to experimental data obtained from recordings of *D. discoideum*. With respect to the transition between straight and circularly moving fan-shaped cells, the results shown in Figure 3.8 are consistent with the earlier predictions [70]. Transitions between amoeboid and fan-shaped motility modes have also been described recently in a wave-generating two-component reaction-diffusion model by Cao *et al.* [91] that specifically emphasizes the role of cell deformation mechanics. While the results are compatible with the findings of Cao *et al.*, the model present here clearly shows that the richness of different motility modes does not require intracellular traveling waves but can be already observed for intracellular kinetics that relies on a single dynamical variable only.

In contrast to these simple modeling approaches based on generic reaction-diffusion systems, there are also more complex descriptions following a different biophysical approach including more detailed biochemical reactions and mechanical forces. For example keratocyte motion has been extensively studied in [126] combining biochemical and mechanical aspects to model how epidermal fish keratocytes form a leading edge, polarize, and maintain their shape and polarity. There are also more complex models where the transitions between straight and circular trajectories have been studied, see for example [127], where a minimal mechanical model is presented consisting of two equations, one for the force balance of the actin network and a second one consisting of a reaction diffusion equation that describes the concentration of myosin, demonstrating that transitions occurs for small values of the Peclet number.

On the other hand, there are reductionist approaches to keratocyte motion, see for example [70] and [75], which display similar levels of complexity as the model presented here. Both types of descriptions contribute to a better understanding of the experimentally observed dynamics and can be readily extended in different directions. For example, on the implementation of more complex biochemical models into the phase field description. In particular, it is possible to extend the model to more closely recover the detailed dynamics of certain intracellular reactions, such as, for example, the phosphorylation of PIP_2 to PIP_3 or the dynamics of the associated kinases and phosphotases that affect cell polarization, membrane deformation, and pseudopod formation [51, 93]. Furthermore, the phase field framework will also allow us to implement cell-cell interactions [128], the behavior of cells under confined stimuli [129], in enclosed environments [130, 131], in the presence of external chemical gradients [80], and also in three dimensions [90].

Despite the restriction of the model to the only comparison with *D. discoideum* cells, the model is also able to describe more diverse situations observed, for example, in keratocytes, where close to the transition to circular motion, bipedial motion was observed that relies on local alternation of cell displacements during persistent motion [132].

In summary, it was studied a model based on a bistable reaction-diffusion equation with Ornstein-Uhlenbeck noise for the intracellular biochemistry, coupled to a dynamical phase field to describe the cell membrane dynamics. The results obtained from the numerical integration of the model show that essential features of amoeboid and fan-shaped motion observed in experiments of motile *D. discoideum* cells are reproduced by the bistable model. A close qualitative agreement between the numerical simulations and the experiments was found, and in some cases, motility measures such as the directionality ratio even showed quantitative agreement.

Based on the simulations one conclusion is that a continuous transition between amoeboid and fan-shaped motions is a realistic scenario, as some of the predicted intermediate states observed in simulations have been confirmed in experiments with *D. discoideum* cells. It can be speculated that the same model can be also employed to describe the motion of other cell types with different motion strategies such as keratocytes or fibroblasts.

Chapter 4

Computational study of interacting cells

4.1 Introduction

Collective migration has been studied extensively in bird flocks, fish schools or cell colonies. However, the mechanisms by which large groups of entities can organize and move remains unclear. Specifically, due to cellular studies, some of the properties behind the movement of a single cell on a flat surface are well understood. Actin filaments inside the cell continuously polymerise and depolymerise to form lamellopodia and protrusions, which are the responsible to push the cell forward [43, 133].

In other hand, it has been studied that in some scenarios cells move in a collective way which drives to the development of many processes [134]. One of these processes is wound healing [135], which is characterized by a group of cells moving towards the wound to remove the presence of any bacteria and with the objective to close the tissue. Another example is

related to embryo genesis [136], where groups of cells migrate to distinct locations to realize specific tasks [137, 138]. One more example which is not beneficial to the organism is the cancer metastasis [139, 140], where groups of cancer cells migrate through tissue and generate the formation of tumors. Clearly, being able to study collective dynamics of cells could give us a better understanding of how these groups coordinate their movement and also to develop therapies against cancer. Recent advances in microscopy techniques combined with cell tracking methods permit us to study collective migration patterns of a large number of cells over extended periods of time with an acceptable cell-level resolution.

In most of the cases, cell collective motility is not simply cells moving freely. Instead, cells move in a coordinated way, different than the one observed in an individual way. One case is when cells forms a mono-layer [141] or when groups of cells are governed by a few leader cells [142]. As long as the cells are not too tightly packed they can continue moving around forming clusters that shows certain patterns and localised burst of velocities [143].

Starting from this point is when physics, in concrete, physical modeling enter to the process of collective cell motion. Describing the motion of cells in a quantitative manner requires solving equations that incorporates different reactions inside the cell and in the environment. There are some reviews [144, 145] where different physical methods that have been used to model this phenomenon were used. A well known method is the Vicsek models [146] of self propelled particles in active matter with or without inter-particle adhesion are commonly used. But to model more realistic cell-cell interactions it is necessary to take into account the spatial extension and the dynamic change in the shape of cells, task that cannot be performed by describing cells by simple point particles. Cellular Potts Model [147, 148], based in lattice models is another successful approach to study this systems.

Here, the cell is represented as a group of pixels of a given size where every pixel is updated one at a time according to certain probability rules. The main limitation of this method is that the dynamics of pixel updates are some somehow artificial and hard to relate with real dynamics of cells. Active Network models, where Vertex [149, 150] and Voronoi [151, 152] models belong are also used to study cell migration, describing tissues as a network of polygonal cells [153]. A limitation of these models is that they do not take into account the internal processes in the cell and anisotropic active stresses in the tissue.

In particular, the social ameoboa *Dictyostelium discoideum* organizes its colonies with chemical waves which produce the aggregation of the cells due to chemotactic motions of the cells. The whole set of interactions is complex and although there are several models studying its properties there is a lack on the link between the interior of the cells and the collective dynamics. For this reason, here, one more time is applicable the deformable properties of the phase field models to study numerically the interaction among deformable objects representing several *Dictyostelium discoideum* cells. The mathematical model used here is described in the previous section and is formed by a reaction-diffusion system embedded into the evolving shape of the cell, fitted to reproduce the dynamics of such cells under different conditions [88, 89]. First, the interactions between two cells is study and later the same analysis is done by increasing the density of cells to promote the cell cell interactions.

In the same was as a study of a single cell, there are also some works related to the use of a phase field model to study the collective motion of eukaryotic cells. One early stage for this study considered the shape change due to the interactions [154] and the rearrangement of cells in clusters [155]. Other works consider a monolayer of deformable motile cells where a solid-liquid

transition is exposed and with this the motility of the cells gets affected [156, 157, 158, 159, 160]. Also the effect of collisions between deformable cells lead to an alignment and collective motion [81, 161, 162].

4.2 Phase field description for a multi cellular system

The computational model used here is the extension of the phase field model coupled with a stochastic bistable process for an individual *Dictyostelium discoideum* cell which has previously studied in section 3. Unlike in the previous section, a distinction in the model has to be done, for every simulation each cell is represented by its own concentration c_i and phase field ϕ_i. Again, the phase field defines the area of the cell and varies from $\phi_i = 1$ inside and $\phi_i = 0$ outside the cell, respectively. A part from the considerations previously mentioned, the model also couples the repulsion among cells to prevent overlap or adhesion. The phase filed with the addition of the repulsion term evolves according to the next equation:

$$\tau \frac{\partial \phi_i}{\partial t} = \gamma \left(\nabla^2 \phi_i - \frac{G'(\phi_i)}{\epsilon^2} \right) - \beta \left(\int \phi_i \, dA - A_0 \right) |\nabla \phi_i| + \alpha \, \phi_i \, c_i \, |\nabla \phi_i| - m_{rep} \sum_{j=1, i \neq j}^{N} \phi_i \phi_j \, |\nabla \phi_i| \, . \tag{4.1}$$

Where in the fourth term in the right side of the equation the cell-cell interactions are modeled, promoting a membrane-membrane contact between cells but at the same time excluding cell overlap, in this term N corresponds to the total number of cells in the system.

Even though the equation corresponding to the dynamics of the biochemical component did not undergo modifications now every cell has its own concentration denoted as c_i. Such concentration diffuses and reacts inside the cell following the next equation

$$\frac{\partial(\phi_i c_i)}{\partial t} = \nabla\left(\phi_i D \nabla c_i\right) + \phi_i[k_a\, c_i\,(1-c_i)(c_i-\delta(c_i)) - \rho\, c_i] + \phi_i\,(1-\phi_i)\,\xi_i(x,t), \tag{4.2}$$

where the the noise at the cell membrane ($\xi(x,t)$) and the parameter controlling the evolution of the concentration (δ) are compute for each cell following the same dynamics as equations (2.3) and (2.4), respectively.

Simulations were performed using finite differences with a spatial and temporal resolution of $\Delta x = 0.15\,\mu m$ and $\Delta t = 0.002\,s$, respectively. The Euler-Maruyama method was used for the stochastic integration of the partial differential equations. The total area considered for each cell was kept constant at $A_0 = 113\ \mu m^2$ corresponding to a circular cell with radius $r = 6\,\mu m$. The area covered by the biochemical component c_i was maintained at $C_0 = 28\ \mu m^2$, corresponding to a quarter of the cell area. The size of the grid and the number of cells were varied to explore different packing fractions NA_0/L^2 in the range from 0.24 to 0.78. Initial conditions of the intracellular concentration fields are chosen to produce polarized cells and promote collisions in the case of binary interaction scenarios, and isotropic in the case of multi-particle simulations.

4.3 Defining polarity and velocity vectors of migrating cells

Some characteristic cell morphologies as observed in numerical simulations are displayed in Figure 4.1. Patches of high concentration of the biochemical component c_i that typically result in extensions/protrusions of the cell boundary are shown in green color in the respective images (cf. Figure 4.1A). Similar to earlier experimental work, where fluorescently marked patches of PI3K were used to quantify the polarization of cells [163], it was taken the advantage of the distribution of the biochemical field c_i for that purpose here as follows. The total area of the cell (A_T) was measured in order to obtain the corresponding centroid coordinates (x_T, y_T). The total area(s) of the patches covered by high values of the field c_i (A_{Ci}) were also measured to obtain the centroid coordinates (x_{C_i}, y_{C_i}) of these area(s). If multiple patches exist, it was taken the weighted average of the individual centroid coordinates to obtain the coordinate (x_{CT}, y_{CT}). Eventually, a polarization vector $\vec{P}$ is defined as the distance between the centroid coordinates (x_T, y_T) and the coordinates (x_{CT}, y_{CT}). Moreover, a velocity vector of cell propagation $\vec{V}$ is defined as the distance between the centroids of the cell at time t and at subsequent time $t + \Delta t$ divided by the numerical time step Δt. In addition, the angle θ between the two vectors $\vec{P}$ and $\vec{V}$ was calculated. In Figure 4.1B-D, the corresponding definitions of the coordinates, vectors, and the angle are shown.

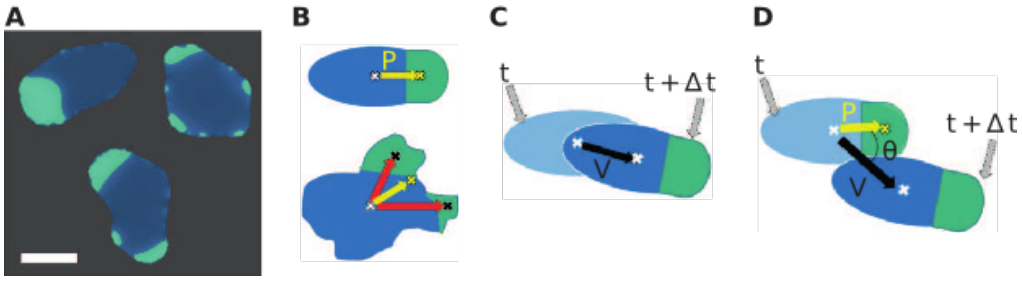

Figure 4.1: (A) Snapshots of the different cell phenotypes as observed in numerical simulations. Green patches indicate the presence of the biochemical component c. Scale bar: $10\mu m$. (B) Illustration of the calculation of the cell polarity vector $\vec{P}$ in the presence of one patch (top) or several patches (bottom). In the latter case, it was considered the weighted averaged of the vectors $\vec{p}_i$ shown in red. The weights are determined by the respective patch size. (C) Illustration of the spatial displacement of a cell in the time interval from t to $t + \Delta t$. (D) Graphical representation of the angle θ between cell polarity $\vec{P}$ and velocity vector $\vec{V}$.

4.4 Protocol of the interaction between two cells

All the possible collisions between two cells that can be generated in the numerical simulations were divided into two specific types: frontal and glancing collisions, see Figure 4.2A. For both types, it is observed three main interaction scenarios with different outcomes as illustrated in Figure 4.2. In the first scenario, which is defined as *alignment* (Figure 4.2B), both cells face and migrate into the same direction after the collision. In the second case, the *anti-alignment* scenario (Figure 4.2C), cells repel each other and move away in opposite directions after the collision. Finally, upon collision, the motion of the two cells may also stall and both cells may remain on the spot, pushing head-on against each other for an extended period of time, before they eventually get released by a random fluctuation. Calling this scenario as *stuck/push* interaction (Figure 4.2D).

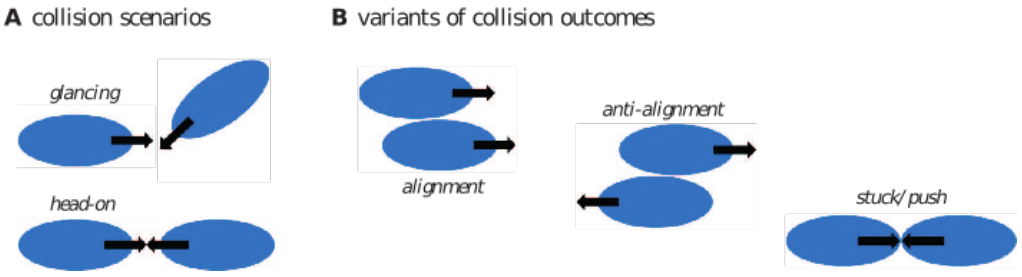

Figure 4.2: (A) Graphical illustration of the different collision scenarios and (B) the respective outcome of the interaction. Initial conditions for binary collision are glancing (top) and head-on collision (bottom). The interaction may result in alignment of cells, anti-alignment of velocities and cell polarities or cells may stuck/push head-on, thereby impeding each others motion.

4.5 Motion of single cell depends on polarization

Cell polarity is a fundamental feature that plays a key role in many cellular functions, such as cell growth, division, and migration. In particular, depending on their degree of polarity, motile cells can display several different motion patterns, such as random, oscillatory or persistent movement. For a motile cell, polarity is typically defined based on the leading and trailing edge (head and tail) of the moving cell. In the model used here, it is the biochemical component c_i which triggers the formation of membrane protrusions (pseudopods) at the cell boundary, and is thus responsible for setting the sense of orientation of the moving cell. For this reason, it is quantified polarity based on a polarity vector $\vec{P}$ that measures the asymmetry in the subcellular distribution of the biochemical component c_i, see Section 4.3 for details. To what extent the displacement of the cell is governed by the direction of the polarity vector is the subject of study of this section.

A wide range of cell motion patterns was studied in numerical simulations

of the present model previously [88]. It was shown that the transition from random to persistent motion is controlled by the model parameter k_a, see Eq. (4.2). Small values of k_a give rise to an erratic trajectory that is caused by the random appearance of protrusions all around the cell. On the other hand, large values of k_a produce a more persistent trajectory due to the accumulation of protrusions in one region of the membrane that sets the overall direction of motion. Those scenarios were associated with the vegetative and the starvation-developed states of *D. discoideum* cells [88], respectively.

Here, is studied cell migration patterns for different values of the parameter k_a, focusing on the dynamics of the displacement and polarity vectors to quantitatively analyze the role of cell polarization for the different modes of locomotion (see Figure 4.3). For every row in Figure 4.3, the panel in the first column shows a snapshot of a simulated cell with a superposition of the polarization vector $\vec{P}$ (in black) and the cell propagation vector $\vec{V}$ (in red). The second column presents the cell trajectories in space. Here, a pronounced change from random to persistent motion can be seen from top to bottom with growing k_a, in line with earlier results [88]. Thus, cells perform larger explorations in space as they become more persistent for high values of the parameter k_a. In the third column, the correlation of the normalized magnitude of the vectors $\vec{P}$ and $\vec{V}$ is displayed, revealing a high degree of correlation for large values of k_a, whereas correlations are low for small k_a. In the fourth column, circular histograms of the angle θ between the vectors $\vec{P}$ and $\vec{V}$ are displayed. For small values of k_a both vectors are typically misaligned, while alignment is observed for high values of k_a. The corresponding probability distribution exhibits a peak around zero that becomes increasingly pronounced for growing values of k_a. These results show that the vectors $\vec{P}$ and $\vec{V}$ are more likely to align for growing

values of k_a, resulting in an increased probability for values of θ close to zero.

In short, the dynamics of the cell propagation vector $\vec{V}$, the polarization vector $\vec{P}$ and the angle θ between them reflects the more persistent and less random motion of cells as the parameter value of k_a increases. To summarize the dependencies on the parameter k_a, it is shown the mean of the absolute values of the vectors $\vec{P}$ and $\vec{V}$ as well as the angle θ between them as a function of k_a in Figure 4.4. With increasing parameter k_a, larger mean values of the polarization vector $\vec{P}$ are observed in Figure 4.4A. This is associated with increasing mean values of the velocity of polarized cells, see the magnitudes of the vector $\vec{V}$ in Figure 4.4B. Figure 4.4C finally shows that not only the absolute values of $\vec{P}$ and $\vec{V}$ increase, but also their alignment is more pronounced with increasing k_a, so that the mean angle θ decreases. For a better comparison, box plots of the angle θ are presented in Figure 4.4D. In summary, persistent motion (high values of k_a) is characterized by larger magnitudes of the vectors $\vec{P}$ and $\vec{V}$ and by smaller angles θ between them, i.e. by increased alignment of the polarity and the displacement directions. On the other hand, random motion (small values of k_a) results from smaller magnitudes of $\vec{P}$ and $\vec{V}$ and larger angles θ, indicating the absence of alignment due to the irregular distribution of patches of c_i that trigger random protrusion all around the cell boundary.

4.6 Simulation results of the interactions between two cells

Before addressing the dynamics of multiple interacting cells, is better to focus first on the interactions between two cells. As detailed in the Sec-

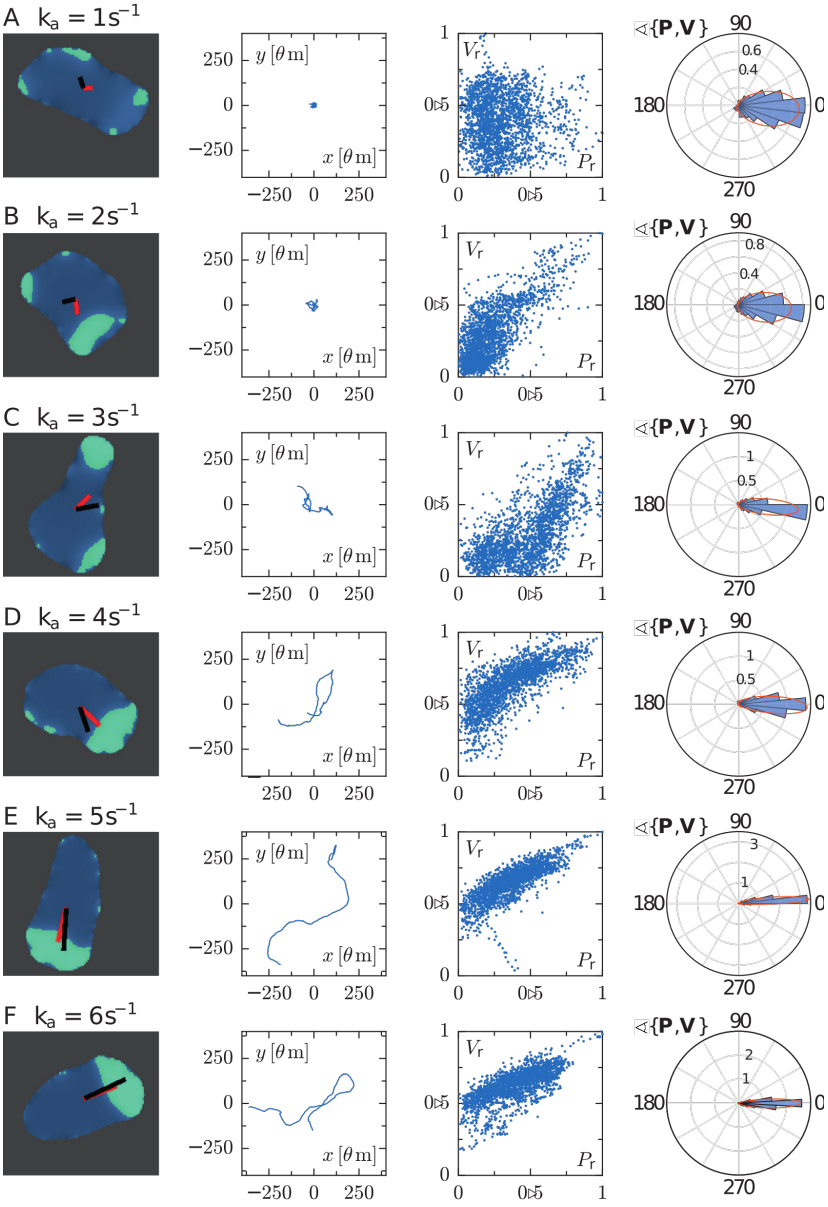

Figure 4.3: Each row corresponds to a particular single cell phenotype for increasing values of the parameter k_a. In the first column, snapshots along with the polarization and velocity vectors $\vec{P}$ and $\vec{V}$ are depicted in black and red, respectively. The corresponding trajectory is shown in the second panels. Third panels represent the correlation of the magnitudes of vectors $\vec{P}$ and $\vec{V}$, which were normalized with respect to the maximal value observed during a simulation. The fourth column panels represent circular histograms for the angle between the vectors $\vec{P}$ and $\vec{V}$. Parameter values: (A) $k_a = 1\,\mathrm{s}^{-1}$, (B) $k_a = 2\,\mathrm{s}^{-1}$, (C) $k_a = 3\,\mathrm{s}^{-1}$, (D) $k_a = 4\,\mathrm{s}^{-1}$, (E) $k_a = 5\,\mathrm{s}^{-1}$, (F) $k_a = 6\,\mathrm{s}^{-1}$.

tion 4.2, it was extended the phase field description of a single amoeboid cell by including a repulsive force between them; any kind of adhesive force

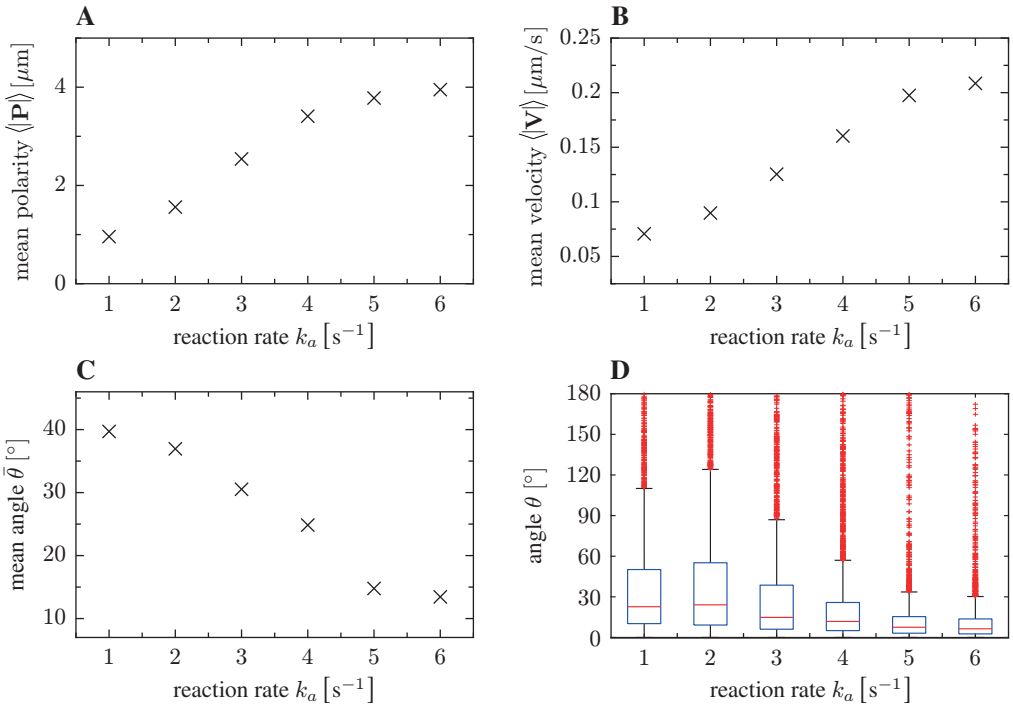

Figure 4.4: (A) Magnitude of mean polarity $\langle\left|\vec{P}\right|\rangle$, (B) mean velocity $\langle\left|\vec{V}\right|\rangle$ and (C) the mean angle for different values of the reaction rate parameter k_a. Accordingly, this parameter controls the polarity of single cells. (D) Box plots of the angle θ as a function of the reaction rate parameter k_a. For high k_a, velocity and cell polarity tend to be aligned.

is neglected. For the following simulations, it was chosen the model parameters in the regime of persistent motion, in particular, the reaction rate was set to $k_a = 5s^{-1}$. A pair of cells close to each other on a square grid for a period of 90 s were simulated with the purpose of making them interact and analyzing the collision dynamics between them. From the simulations, it is possible to distinguish three types of collision scenarios that were termed *alignment*, *anti-alignment* and *stuck/push*, illustrated in Figure 4.2 (see also Section 4.4). In Figure 4.5 are displayed a representative series of snapshots for each of the three scenarios observed in simulations of glancing collisions (Figure 4.5A-C) as well as for head-on collisions (Figure 4.5D-F). It was found that the avoidance between cells (anti-alignment) was the most frequently observed case in the simulations, see Figure 4.5B and E.

The second most frequent scenario was the alignment of cells, as can be seen in Figure 4.5A and D. Finally, the stuck/push scenario was only rarely observed, see Figure 4.5C and F. The two cells, which get stuck upon collision, push against each other for an extended period of time, before the shape of one of them is strongly distorted, as a consequence of which the heads-on pushing configuration is destabilized and they continue moving in different directions. However, as will be show in the next sections, this case will be more frequently observed when the density of cells is increased.

Additionally, it was analyzed the collision-induced dynamics of the cells in more detail in Figure 4.6, following the same order as in Figure 4.5. In the first column are displayed snapshots of the two interacting cells for every studied case, including the polarity vector $\vec{P}$ and velocity vector $\vec{V}$ for each cell. In the second column, representations of the cell trajectories are shown, revealing clear differences between the different collision scenarios. In the alignment case (A and D), for example, trajectories tend to be parallel, while a crossing of tracks is seen for the anti-alignment scenario (B and E). Only small displacements are obtained in the stuck/push case (C and F) as cells impede each others motion upon head-on collision. The third column displays again the correlation of the normalized magnitudes of the vectors $\vec{P}$ and $\vec{V}$. The fourth column shows the distributions of the angle θ between the polarity and velocity vectors $\vec{P}$ and $\vec{V}$ for the two interacting cells – wider distributions for the angle are seen in the stuck/push scenario.

For all the cases, the magnitude of both vectors tend to correlate, regardless of the orientation of the cells. This behavior is more clearly observed in the alignment and anti-alignment cases, while in the stuck/push case this tendency is weaker. As mentioned before, these distributions are wider for the stuck/push case, indicating stronger fluctuations and less correlations

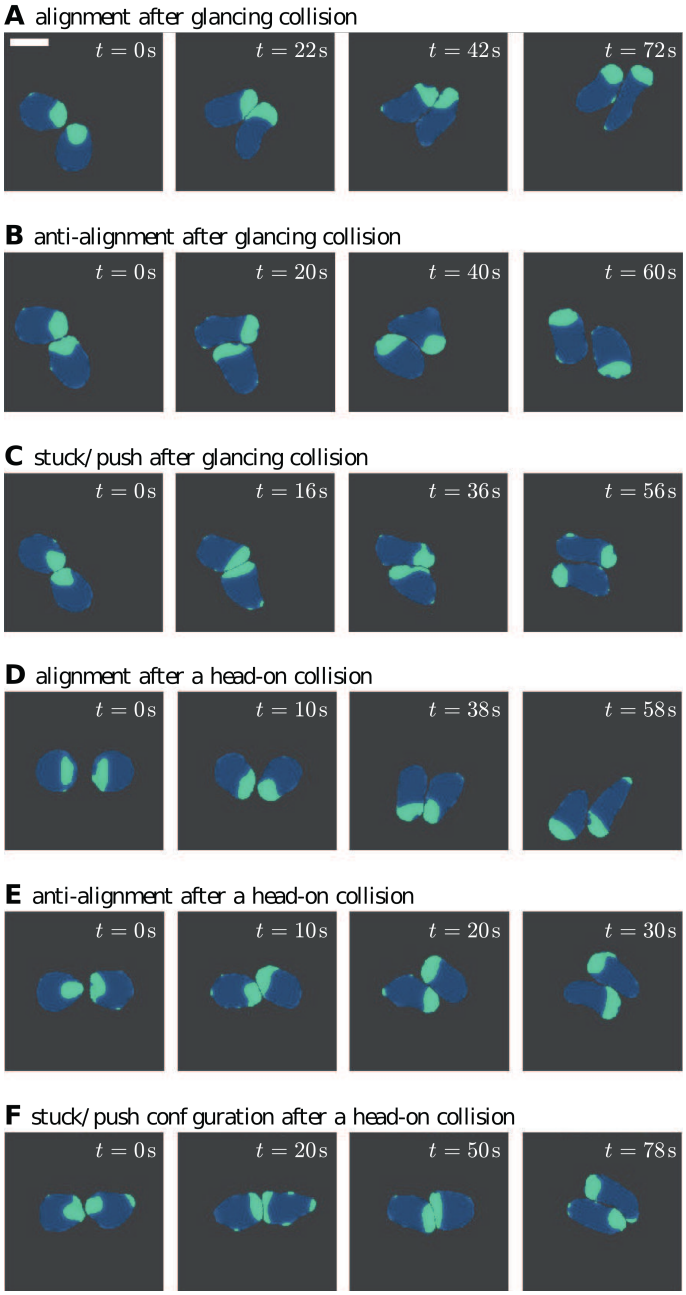

Figure 4.5: Sequence of snapshots of a binary interaction of cells, representing (A) alignment, (B) anti-alignment and (C) stuck/push scenarios for a glancing collision. Panels (D), (E) and (F) show the alignment, anti-alignment and stuck/push scenarios, respectively, corresponding to head-on collision. Scale bar: $10\mu m$.

in the orientations of the polarity and velocity vectors $\vec{P}$ and $\vec{V}$.

The results discussed in Figure 4.6 are summarized by box plots of the angle θ between $\vec{P}$ and $\vec{V}$ for the different scenarios shown in Figure 4.7.

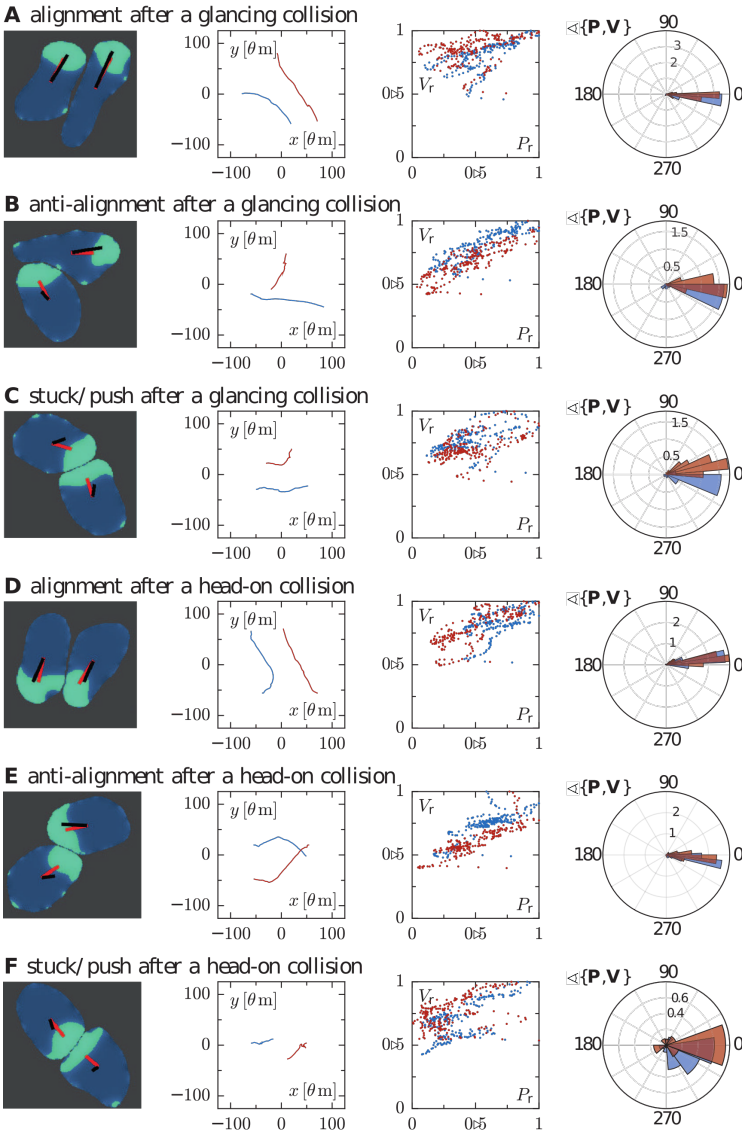

Figure 4.6: Quantitative analysis of binary cell interactions in terms of the cell polarity and velocity vectors for different interaction scenarios, cf. Figure 4.5. For every row (A-F), the first column panels show the snapshots of cells where a representation of the vectors $\vec{P}$ and $\vec{V}$ is included. The second column shows the corresponding trajectories. Analogously to Figure 4.2, the third column represents the correlation of the rescaled magnitudes of vectors $\vec{P}$ and $\vec{V}$ of the two interacting cells. The panels in fourth column show circular histograms of the angle θ enclosed by cell polarity $\vec{P}$ and velocity $\vec{V}$. The collision scenarios in (A-C) correspond to glancing collisions, resulting in (A) alignment, (B) anti-alignment and (C) stuck/push configurations. In contrast, panels (D-F) correspond to head-on collisions, likewise resulting in (D) alignment, (E) anti-alignment and (F) stuck/push configurations.

The alignment and anti-alignment scenarios generate only small differences in the orientations of the vectors $\vec{P}$ and $\vec{V}$ during the interactions and, therefore, $\vec{P}$ and $\vec{V}$ are typically aligned. In contrast, larger deviations of the relative orientation of the vectors and, consequently, larger values of θ occur in the stuck/push scenario, indicating that vectors $\vec{P}$ and $\vec{V}$ are not aligned.

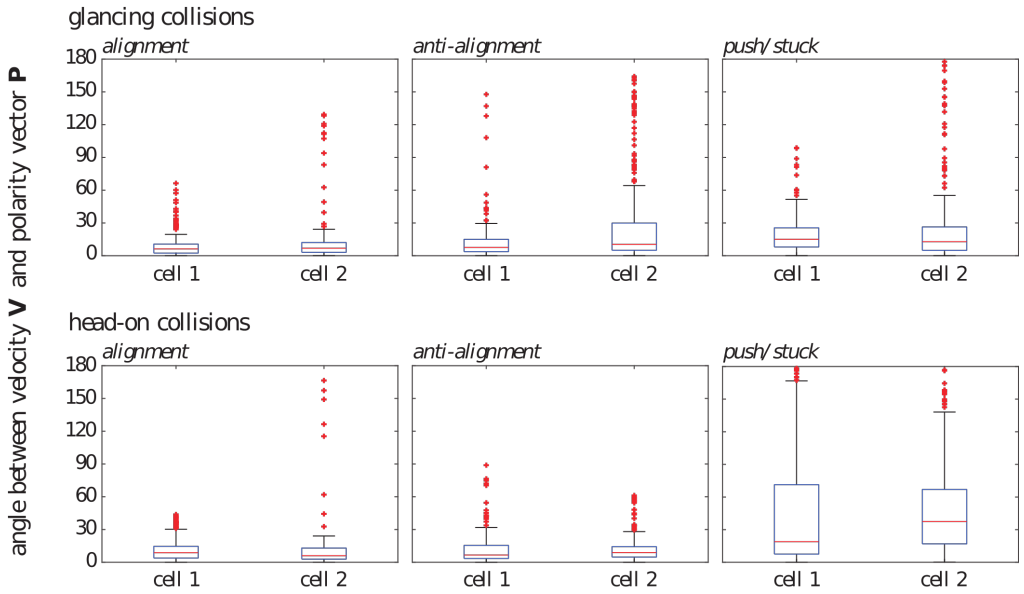

Figure 4.7: Boxplot representations of the measured angles θ during the interaction of two cells. The panels correspond to alignment, anti-alignment and stuck/push cases for the glancing collisions (A1-A3) and head-on collisions (B1-B3), respectively.

4.7 Simulation results with larger set of cells

The increase of the number of cells implies an increase of the computational cost and, more complex dynamics is observed for the interactions among the cells.

First, it was considered a system formed by 25 cells moving and interacting freely in a system formed by a square region of length $L = 108\ \mu m$.

From the resulting dynamics, the previous three types of collision (aligning, avoiding and pushing) were identified.

Several snapshots of such simulations are shown in Figure 4.8. The twelve snapshot shown in the figure show a large system where the 25 cells interact. During the simulation the different types of two cells collisions are observed and some of them are highlighted inside a red circle in the figure. Images in Figure 4.8A begin with the situation where two cells are close to collide between them. Once they get in contact, they start to align respect to each other to continue their trajectories. In the snapshots in Figure 4.8B, the two cells marked avoid each other to continue following different trajectories. Finally, Figure 4.8C shows two cells which collide and stay stuck and pushing each other for a period of time, after such time, both suddenly dis-aggregate and continue following different paths.

4.8 Increase of density decreases mobility and misalign polarization and motion

From here, larger numbers of interacting cells will be considered. From the various cell-cell interactions within the ensemble of cells, it is possible to identify the previously observed three collision scenarios: alignment, anti-alignment and stuck/push, see Figure 4.8.

The system size L was varied, keeping the number of cells $N = 25$ fixed, to assess the density dependence of motility characteristics, the relevance of collision scenarios and the resulting collective pattern formation. The cell density $\rho_R = NA_0/L^2$ is determined by the number of cells per unit area in the simulation box. At high cell densities, jamming is expected to be

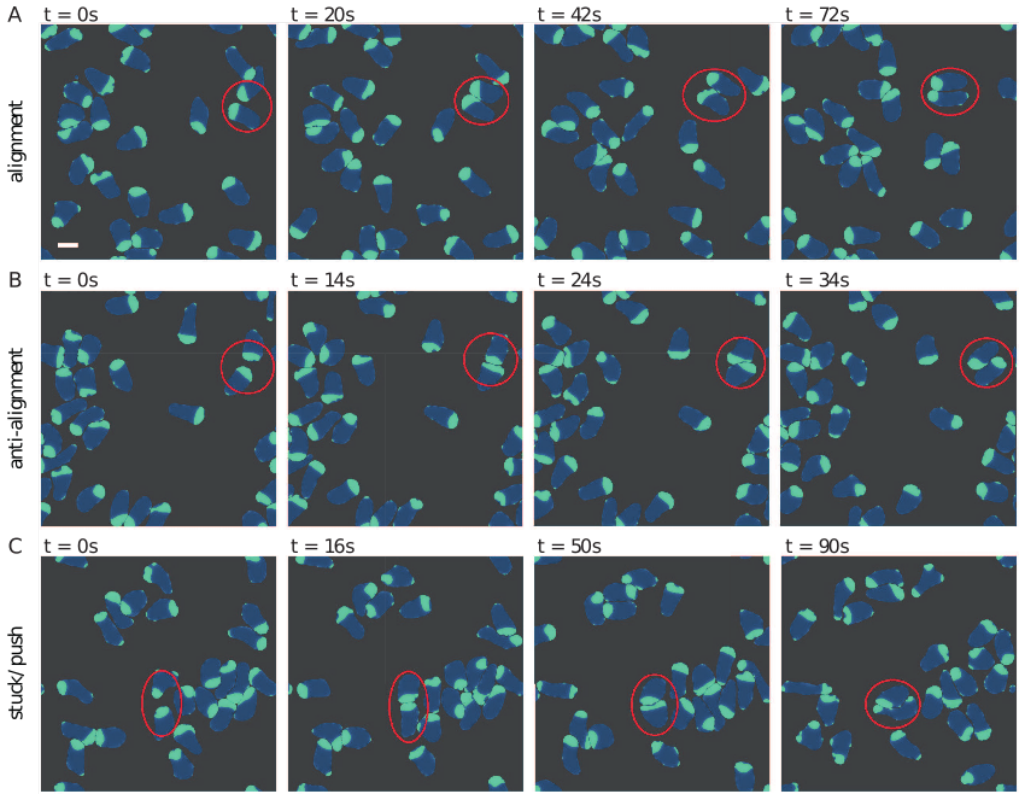

Figure 4.8: Snapshots of binary interactions in an ensemble of cells (periodic boundary conditions). The red marks highlights characteristic collision scenarios: (A) alignment, (B) anti-alignment and (C) stuck/push configurations. Scale bar: 10 μm.

more relevant as the probability of cell-cell collisions increases. To study these effects, five different domain sizes were simulated; Figure 4.9 shows exemplarily the gradual transition from a dilute (Figure 4.9A and Supplementary Movie SM7) to a dense system (Figure 4.9E and Supplementary Movie SM8).

In high density scenarios, stuck/push interactions are more commonly observed as cells trying to follow their own trajectory collide with others, thereby competing for free space. This behavior is expected due to the higher packing fraction. For the chosen model parameters, cells tend to remain fairly polarized – the mean magnitude of the polarity vector does only weakly depend on the cell density (cf. Figure 4.9F). The mean velocity, however, decreases significantly as the cell density is increased (see

Figure 4.9G) due to the lack of free space in a dense system. As a result of frequent cell-cell collisions, the angle between polarity and displacement vectors increases on average as a function of the density ρ_R as shown in Figure 4.9H. This is in line with a previous observation that velocity $\vec{V}$ and cell polarity vector $\vec{P}$ tend to be misaligned as a result of stuck/push interactions (see Figure 4.6F and the corresponding discussion in Section 4.6). As cells remain polarized – most of the biochemical component c_i is con-

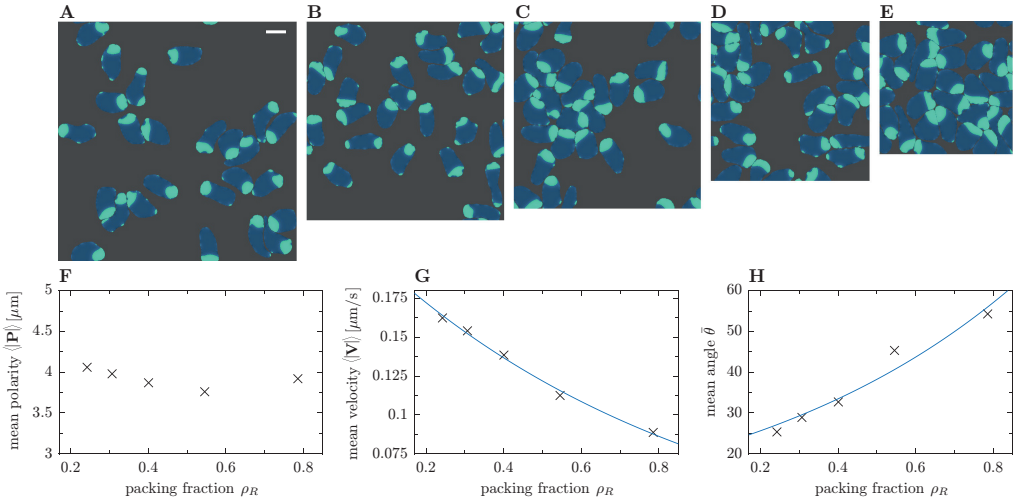

Figure 4.9: Snapshots of simulations with constant cell number $N = 25$ and varying system size with a difference in side length of $L = 12\mu m$ between consecutive panels. The side length L of the simulation box and the packing fraction $\rho_R = NA_0/L^2$ are: (A) $L = 108\mu m$ and $\rho_R = 0.24$; (B) $L = 96\mu m$ and $\rho_R = 0.30$; (C) $L = 84\mu m$ and $\rho_R = 0.40$; (D) $L = 72\mu m$ and $\rho_R = 0.54$; (E) $L = 60\mu m$ and $\rho_R = 0.78$. (F) Mean polarity, (G) mean speed and (H) mean angle between velocity and polarity for different packing fractions ρ_R. The number of cells was fixed ($N = 25$ cells), while the system size was varied. The fits in panels (G) and (H) provide a guide to the eye. Scale bar: 10 μm.

centrated in one certain part of cells – but collisions change their velocities, the vectors $\vec{P}$ and $\vec{V}$ cease to be aligned and the angle between them, thus, increases.

The numerical results suggest that stuck/push collision scenarios are more relevant at higher cell densities. As cells impede each others motion as a

result of stalling, these collisions may lead to the formation of clusters composed of immobile cells. This mechanism is reminiscent of the explanation of motility-induced phase separation (MIPS) as observed in self-propelled discs [164] that show phase separation at high density because particles hamper each others motion upon head-on collision. It is important to highlight, that the clustering dynamics observed in deformable cells is different from classical MIPS: as cells are deformable, the local stress acting on one cell is anisotropic. This effect is even more pronounced as clusters grow in size and, consequently, the local pressure increases. As a result, clusters frequently break apart, thereby giving rise to a complex and dynamic clustering dynamics. To quantify clustering, the cluster size distribution was measured numerically (Figure 4.10). It was considered that two cells belong to the same cluster if the distance between them is smaller than $12\mu m$ which corresponds roughly to twice the average radius of a cell (in the absence of interactions). At low densities, a few collisions lead to the transient formation of small groups of cells. Group sizes range from a few cells to more than half of the total number of cells in the system (Figure 4.10A). In contrast, larger groups are more frequently formed in dense systems (Figure 4.10B-D). Accordingly, the cluster size distribution broadens as the cell density is increased and adopts even a bimodal shape in the high density limit (Figure 4.10E). A direct comparison of the transition from a unimodal to a bimodal shape can be seen in Figure 4.10F, where panels corresponding to the lowest and highest density are shown together for a better visualization. This structural change of the cluster size distribution eventually allows to define a critical density above which clustering sets in, similar to the clustering transition observed in ensembles of self-propelled rods [165, 166].

It was furthermore quantified the random transport of cells within an en-

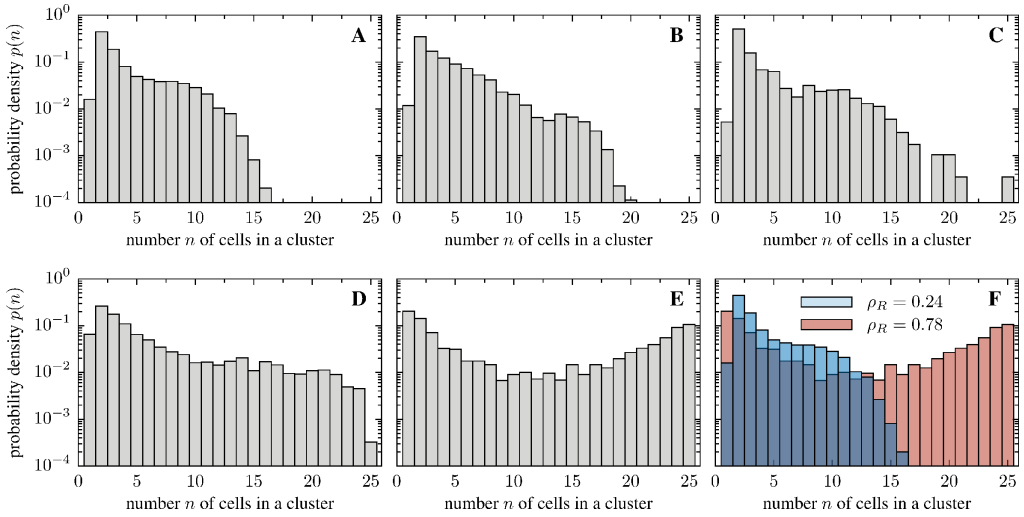

Figure 4.10: Histograms of the observed cluster sizes for various packing fractions. The cell number was kept constant ($N = 25$ cells) and the system size was varied. The packing fractions values of the different panels are (A) $\rho_R = 0.24$, (B) $\rho_R = 0.30$, (C) $\rho_R = 0.40$, (D) $\rho_R = 0.54$ and (E) $\rho_R = 0.78$. For increasing density, the cluster size distribution changes from a unimodal to a bimodal structure, signaling a clustering transition. This transition is highlighted in the last panel (F), where the cluster size distribution for low and high packing fraction is overlayed to simplify the comparison.

semble by the mean square displacement $\langle|\Delta\vec{x}(t)|^2\rangle$, i.e. the average displacement of a cell evaluated at different time lags. The mean square displacement (MSD) decreases monotonically with the cell density ρ_R as cells can move more persistently at lower cell densities. In all cases, it is observed a transition from a ballistic regime ($\langle|\Delta\vec{x}(t)|^2\rangle \sim t^2$) at short time scales to a diffusive regime ($\langle|\Delta\vec{x}(t)|^2\rangle \sim t$) in the long-time limit (see Figure 4.11). It was measured the density dependence of the effective diffusion coefficient D of cells by fitting Fürth's formula,

$$\left\langle|\vec{x}(t) - \vec{x}(t=0)|^2\right\rangle = 4D\left[t - \tau\left(1 - e^{-t/\tau}\right)\right], \tag{4.3}$$

to the numerically obtained MSD curves. The diffusion coefficient decreases as the density is increased (cf. Figure 4.11C). Moreover, the fits show that the crossover timescale τ decreases as the density of particle

increases, due to a reduction of the mean-free path and a higher collision frequency at high density.

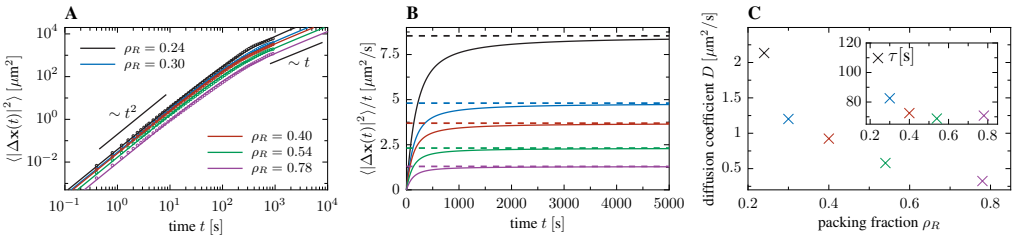

Figure 4.11: (A) Mean square displacement (MSD) of cells for a system of $N = 25$ cells in a box of various side length (implying various packing fractions). (B) Mean square displacement (MSD) of particles, divided by time, for a system of $N = 25$ cells in a box of various side length. (C) Dependence of the effective diffusion coefficient on the packing fraction, extracted via fitting Fürth's formula to the mean square displacement; the inset shows the decrease of the crossover timescale τ as a function of the density (Eq. (4.3)).

It was double-checked that equivalent results are obtained when the density is increased by changing the particle number in a system of fixed size of $L = 108\mu m$ (data not shown) instead of fixing the particle number and decreasing the side length of the simulation box as discussed above (Figures 4.9-4.11).

4.9 Increasing of the system size keeping the density of cells does not modify the observed dynamics

The results section was concluded by assessing the relevance of the finite system size in numerical simulations. A finite-size scaling analysis was performed, varying the number of cells and system size such that the density or, equivalently, the packing fraction is kept constant. Five representative snapshots of the simulated systems are shown in Figure 4.12A-E, where the

number of cells is 25, 36, 49, 64 and 81, respectively, and the system size was adjusted from $L = 60\ \mu m$ to $L = 108\ \mu m$ accordingly. As shown in Figure 4.12F and G, the measured value of the mean polarity and velocity does not reveal a significant system size dependence. Furthermore, the angle θ between the vectors $\vec{P}$ and $\vec{V}$ in all cases does not change on average as the number of cells is varied (cf. Figure 4.12H).

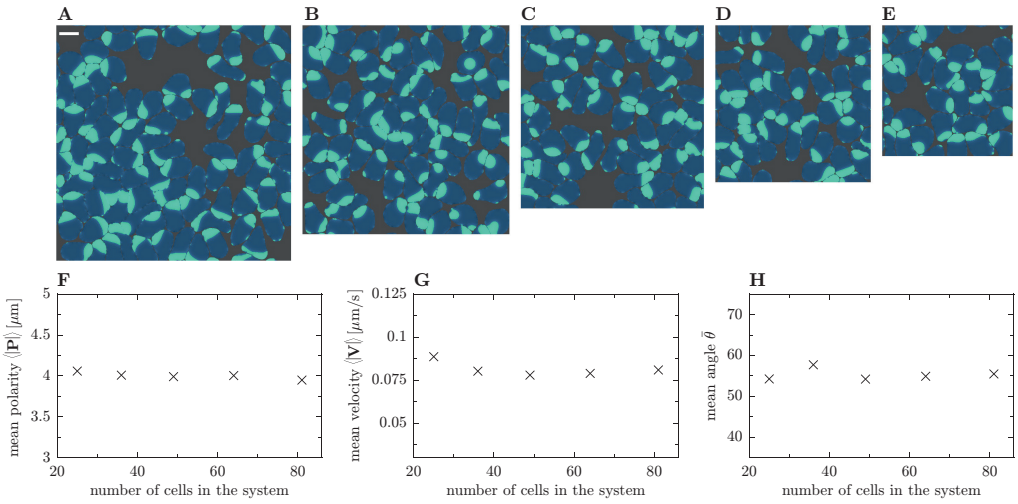

Figure 4.12: Snapshots of simulations with the same particle packing fraction $\rho_R = 0.78$. The number of cells and the side length are (A) 81 cells and $L = 108\mu m$, (B) 64 cells and $L = 96\mu m$, (C) 49 cells and $L = 84\mu m$, (D) 36 cells and $L = 72\mu m$, (E) 25 cells and $L = 60\mu m$. (F) Mean polarity, (G) mean velocity and (H) mean angle between velocity and polarity vector for a fixed packing fraction but various cell numbers in the system. Scale bar: 10 μm.

The tendency of cells to align or impede each others motion upon collision in stuck/push configurations implies a tendency towards cluster formation in the system (see Supplementary Movies SM9 and SM10 for simulations with 49 and 64 cells, respectively). As the system size increases, larger clusters of cells tend to form as shown in Figure 4.12. The clustering dynamics were quantitatively investigated by measuring the cluster size distribution in the stationary state; a comparison of all the studied cases is displayed in Figure 4.13. In contrast to the numerical experiment discussed in Section 4.8, where the density was increased, the shape of the cluster

size distribution is now qualitatively independent of the system size as the cell number and system size is increased simultaneously such that the cell density remains constant. The cluster size distribution turns out to be bimodal for the considered density (Figures 4.13A-E). Figure 4.13F shows the probability of the rescaled cluster size for the system with the highest ($N = 81$) and smallest number of cells ($N = 25$). Note, however that the results display large fluctuations and conclusions have to be drawn with caution.

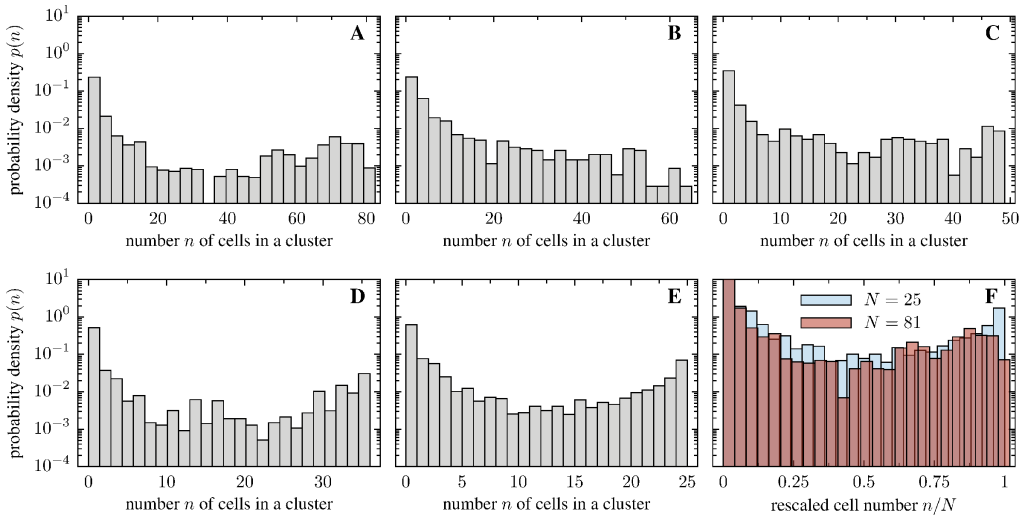

Figure 4.13: Cluster size distribution for a fixed packing fraction but various system sizes: (A) 81 cells and $L = 108\mu m$, (B) 64 cells and $L = 96\mu m$, (C) 49 cells and $L = 84\mu m$, (D) 36 cells and $L = 72\mu m$, (E) 25 cells and $L = 60\mu m$. In panel (F) is overlaid the probability distribution of the re-scaled cluster size n/N for the smallest and largest particle number, indicating that the structure of the cluster size distribution is system size independent.

4.10 Discussion

A generic mathematical model to describe the collective pattern formation of soft, deformable, self-driven cells was employed. The model couples the intracellular biochemistry, responsible for cell polarization, the formation

of membrane protrusions and, thus, for active motion, with a phase field which accounts for the current position and shape of the cell membrane. Each cell is described by an individual phase field. It was included a repulsive interaction between cells into a previously established phase field model for individual cells [88] in order to prevent them from overlapping. This framework enables us to address the complex interplay of dynamic particle shape, nonlinear repulsive interactions, self-propelled motion and the emergence of collective patterns in the context of active matter.

Individual *D. discoideum* cells may aggregate following chemotactic signals to form a multicellular structure [167]. At large spatial scales, the chemotactic concentration and the density of cells can be modelled using reaction-diffusion equations [168]. In addition, there are several attempts to model the life cycle of *D. discoideum* from single cell shape changes and chemotaxis to collective behavior [169, 170].

The present modeling framework constitutes an active matter system composed of individual propellers, which are simple models of deformable cell like amoeba, e.g. *D. discoideum* cells. Whereas the role of particle shape [165, 166, 171] and the symmetries of interactions [146, 172] have extensively been debated for active matter systems, the relevance of the deformability of particles has seldomly been addressed [162, 173]. Oftentimes, active particles are considered as point-like objects or active spins [174], in the spirit of the seminal Vicsek model [146, 172], or as rigid objects such as active rods [166], microswimmers [175] and self-propelled discs [176] or . The advantage of these approaches is their low computational cost, allowing to simulate several thousands of particles simultaneously. The computational cost associated with the incorporation of the deformability of particles, however, precludes the modeling of large amounts of individuals. A number around 100 cells was reached in the simulations and, therefore,

it is still far away from the limit considered in more theoretical studies. However, here is made a first step towards connecting the dynamics at different scales, namely the intracellular pattern formation – responsible for the polarization of cells – and the collective dynamics of several individuals.

As observed in the simulations, cell deformation is an important aspect included in this work. It permits to recreate scenarios closer to reality, for example in the study of motility in reduced spaces such as narrow vessels in the process of cancer metastasis [130, 177]. This deformation is driven by the accumulation of a biochemical component inside the cell and by the interactions among the different cells present in the system. This characteristic is also observed when nonequilibrium stresses are built up during cluster formation and cells begin to deform. This is quite different from rigid spheres, where other mechanisms influence the motion.

The numerical simulations presented in this work reveal rich collective pattern formation phenomena. For rigid active particles, the symmetry of individuals determines the symmetry of the interaction potential and, thereby, constrain the symmetries of emergent patterns: self-propelled discs may undergo dynamic clustering or motility-induced phase separation [176, 178]; in the classical Vicsek model with polar alignment interaction, polarly ordered structures are observed at the macroscale [146, 172]; elliptical self-propelled rods, in contrast, may form polar or nematic patterns, which may even dynamically coexist, depending on the strength of self-propulsion [171, 179]. Collective dynamics of cells is strongly determined by the interactions among them. While here it was only considered a repulsion term, there are other phenomena involved in cell-to-cell communication [180] and, in particular, in cell-to-cell contact-inhibition [181]. Such interactions can be easily included in the present model. There are already some attempts to include deformation in collective cell dynamics. A protrusion region has

been added to rigid spheres to simulate the deformation of the cells [154] and some phase field models have been already implemented to describe oscillations in epithelial cells [157]. Deformable cells, however, do not fall in any of these categories as the particle shape and, thus, the symmetry of the interactions, is a dynamic feature which is determined by intracellular biochemical processes as well as the complex, nonlinear interactions with other cells due to collisions that, in turn, induce additional cell shape changes. Accordingly, it was found different interaction scenarios that may lead to alignment, anti-alignment and stuck/push configurations, whose relevance depends on the relative position and orientation of two cells before the collision event, the stiffness of particles as well as the global cell density.

The modeling framework decouples the actual displacement of a cell in space from the intracellular polarization dynamics. Therefore, it is possible to establish cell polarity $\vec{P}$ and velocity $\vec{V}$ based on the biochemical concentration patches and spatial displacements, respectively, enabling to quantify the intricate, nonlinear coupling of cell polarization and motion. It was first analyzed at the single-cell level for different parameters sets which could, for example, represent vegetative or starvation conditions of *D. discoideum* cells. Furthermore, it was established how cell polarity and velocity vectors – as well as the angle between them – behave in ensembles of interacting cells and studied their density and system size dependence. For the considered model parameters, cell polarization depends only weakly on cell density, whereas the velocity of cells strongly decreases as the packing fraction is increased.

The present modeling framework allows to tune parameters such that the cell polarity is rather stable. The stability of the polarity axis, due to the intracellular pattern formation mechanisms described here, represents an

effective memory on the polarity axis [182]. This memory precludes the formation of pseudopods at the side and at the rear of the cell [183] when cells follow a gradient of chemoattractant [49]. In this case, the polarity axis can be determined by the external gradient or by fitting an ellipsoid to the cell.

In single cell systems, velocity and polarity of cells are directly correlated. During persistent motion, most of the biochemical component inside the cell is accumulated behind the leading edge of the cell membrane; cell polarity and velocity vectors are aligned to a high degree, i.e. the angle between them is small. A random reorientation takes places if various patches of the biochemical concentration exist inside the cell, thereby inducing a misalignment of cell polarity and velocity vector.

In ensembles of interacting cells, a nontrivial coupling of cell polarization and velocity emerges dynamically due to cell-cell collisions. Even if parameters are tuned such that cells remain highly polarized (starvation conditions of *D. discoideum*), there is a density dependent contribution to the interaction between cell polarization and velocity. In particular, jamming of particles misaligns polarity $\vec{P}$ and velocity $\vec{V}$; in the high density regime, stuck/push collisions during which cells stall each others motion are most prominent. Consequently, is observable a transient clustering – clusters dynamically build-up and break apart. The stability of clusters is crucially determined by the deformability of cells: as cells are soft, the local anisotropic stress acting on one cell inside a cluster yields cell-shape changes which may eventually destabilize the entire cluster. In the low density regime, in contrast, cells can move freely and persistently, reflected by the tendency of cell polarization and velocity to align.

Several model parameters were fixed within this study. There is poten-

tially a plethora of modes of motility to be explored by changing the level of noise intensity, for example. Moreover, the modeling framework can be extended in many nontrivial ways in the future, e.g. including confinement, attractive interactions or collision-induced inhibition [81, 154, 162]. Specific modifications will enable to bring the modeling closer to a particular application, such as the study of collective cell motility in wound repair, immune response and tissue morphogenesis [184, 185].

In summary, it was developed a generic modeling framework to computationally simulate the dynamics of active matter systems which are composed of deformable particles, such as amoeboid cells. This method bridges the gap between the intracellular biochemical kinetics, in turn controlling the membrane activity of cells, the resulting locomotion of amoeboid cells and their emergent collective dynamics. Understanding self-organization processes of cells is of high relevance, for example for the aggregation processes of *D. discoideum*, but also for collective cell dynamics during immune responses and cancer spreading.

Chapter 5

Crawling cells in a confined environment

5.1 Introduction

Under confinement, cells migrate and often move inside narrow and small spaces; as a consequence the cells restructure the cytoplasm and deform the membrane to pass through those small spaces. Recently, the use of microfluidic chips to study this type of cell motility has become more common. These devices have the characteristic that they are connected through open spaces in the form of parallel channels (microchannels) which allow the loaded cells or fluids that are being studied to move along in certain directions. The materials that are employed to develop these types of devices are silicon, glass and polymers. Some examples of these devices are shown in Figure5.1A-C. Devices made of polydimethylsiloxane (PDMS) polymers are commonly used in laboratories due to their low cost and ease of manufacture [186, 187], see Figure5.1D.

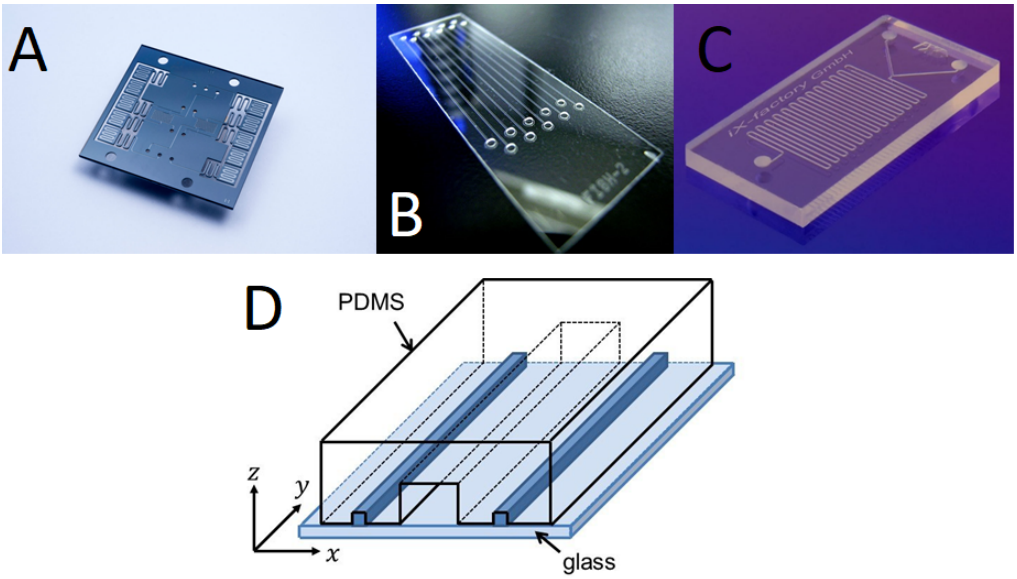

Figure 5.1: Three most common materials in microfluidic chips, (A) silicon, (B) glass and (C) polymers. (D) Scheme of a PDMS device microfluidic channel where two auxiliary channels run in parallel.

In the in vitro scenario some experiments have been done associating the free-flow transport of particles and cells in microchannels with the use of electrokinetics [188], frequency-modulated ultrasound [189], a light-directed migration of multi-cellular organisms (slugs) [190], the response due to a cAMP gradient [191, 192], water permeation [193] and the absence of external gradients [194, 195].

These experiments analyze how microchannels modify the ability of cells to spread and polarize, and their resulting speed. The further study of cell migration inside microchannels allows us to examine some aspects of the environmental confinement with cells experiments *in vivo* [196]. for example, to quantify and determine the existence of an optimized environment for the motility of a specific group of cells like lymphocytes. Another application with great relevance nowadays is the tracking strategies associated with cancer cells [197], first to target them and finally to start the treatment.

One characteristic observed in cells inside channels is the sudden persistent motion, even with the absence or presence of gradients to guide the motion of the cells; see Figure 5.2. Cells tend to slow down in narrow channels because of the close contact with the walls. In wider channels the cell is unable to touch both sides, reducing its forward protrusion [198]. Therefore, there is an optimal size where the cell's speed is maximum.

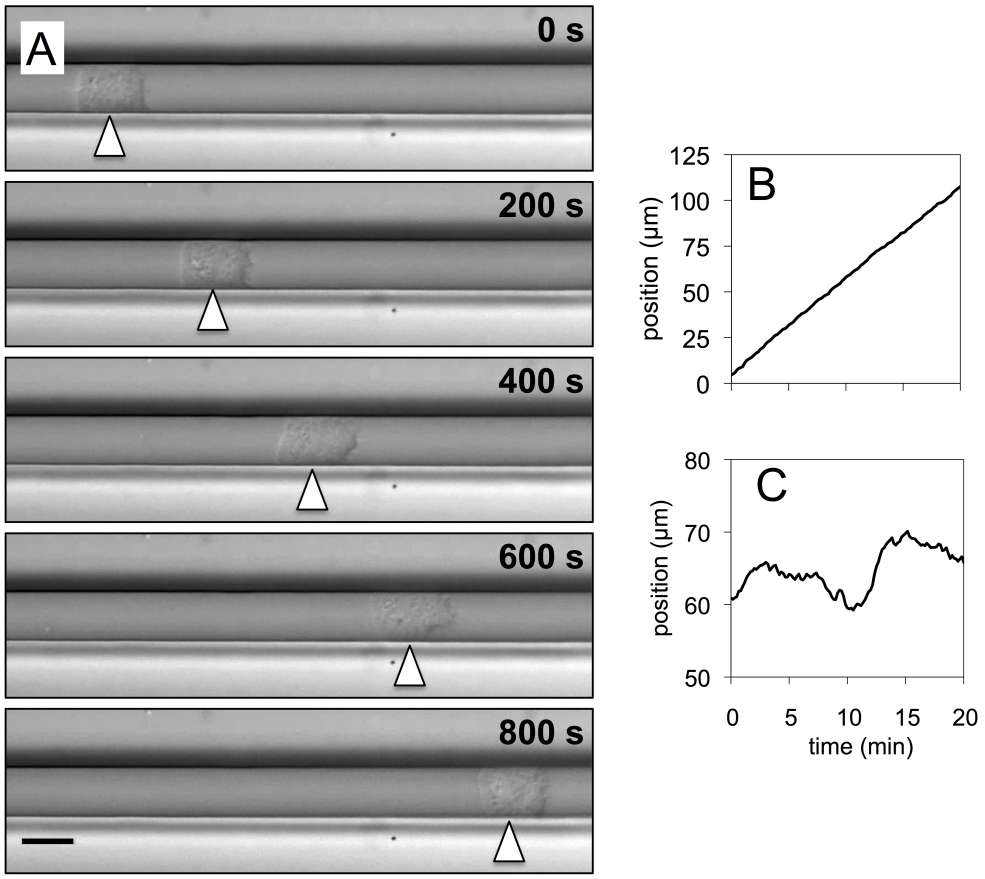

Figure 5.2: (A) Snapshots for a in vivo persistent moving cell inside a microchannel environment, (B) position of a persistent cell inside a microchannel as a function of time , (C) position of an erratic cell inside a microchannel as a function of time. Scale bar: 10 μm. Figure adapted from [130]

There are some studies where the effects of the size of microchannels were modeled [199]. Despite achieving very close agreement with experiments some of their limitations are the assumption that the cell slips freely on a lubricated layer [200], which means that there is no contact between the cell

and the wall, which is contradictory to the experiments where this contact exists. Another limitation is the lack of cell deformability [201] and the inability to encompass a front and a rear of the cell [202].

The adhesion of a phase field in a similar way as noted in previous sections has been studied to reproduce migration inside microchannels. This technique was used to describe the intracellular and membrane dynamics, taking into account internal and external forces, surface tension and obstacle contact [84]. In this chapter this is combined in a stochastic bistable process with a phase field to reproduce some types of cell motion and the respective displacements and shape deformations in scenarios such as microchannels.

5.2 Phase field coupled to a crawling cell model inside microchannels

In the present chapter the effect of the motility of a single social amoeba *Dictyostelium discoideum* cell inside a microchannel is investigated. Here, again, the model described in [88] is taken as a reference. For that purpose, a phase field model was adapted to reproduce a scenario similar to that in microchannel devices. To model this environment, a system coupled with two parallel static walls where the cell moves in between them was constructed. The dynamic phase field proposed here evolves in accordance with the following equation:

$$\tau\frac{\partial\phi}{\partial t} = \gamma\left(\nabla^2\phi - \frac{G'(\phi)}{\epsilon^2}\right) - \beta\left(\int \phi\, dA - A_0\right)|\nabla\phi| + \alpha\,\phi\, c\,|\nabla\phi| - m_a\phi_c\,\phi\,|\nabla\phi|\,, \tag{5.1}$$

which corresponds to the phase field described in equation (2.1) with the addition of the term $-m_a\phi_c\ \phi$, which corresponds to the interaction of the cell's phase field and the static phase field representing the microchannel walls.

In contrast, the reaction-diffusion equation related to the biochemical concentration, previously described as c, was maintained as described in equation (2.2).

5.3 Results of random and persistent cell migration inside microchannels

To create regions of controlled microchannel confinement, simulations for different channel widths were performed ($4.5, 6.0, 7.5, 9.0, 10.5$ and $12.0\mu m$) where position and instant velocity were measured. The parameters for the simulations were the same as those used in Chapter 2 and periodic boundary conditions were maintained. It is important to note that no gradients were included in the simulations. Another point to take into account is that the parameter corresponding to the reaction rate k_a was slightly varied for different simulations, with the purpose of studying a wide range of different motility phases, from random to persistent motility. For a better visualization, in Figure 5.3 a snapshot representation for different channel widths is presented.

The motion of the simulating *Dictyostelium discoideum* cells inside a microfluidic device, represented by a channel, was measured. One notable characteristic is that most of the cells inside the microchannel experienced prevalent sudden changes in their trajectory and direction of motion (from

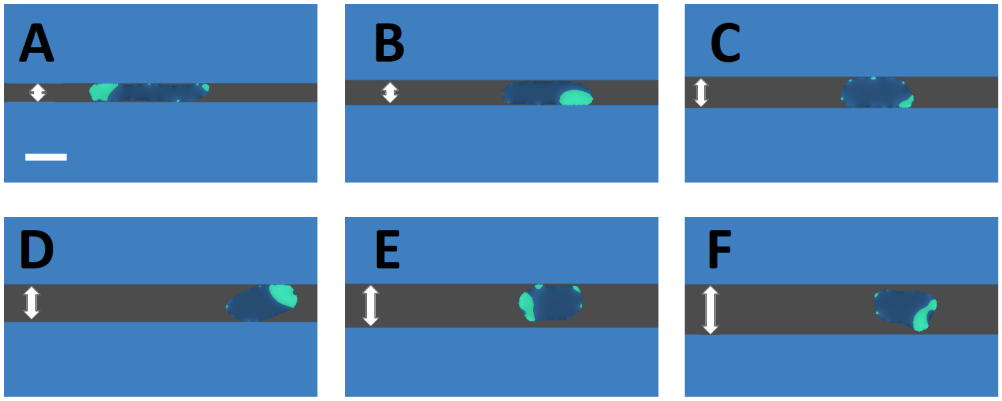

Figure 5.3: Snapshots for the different channel width used in simulations. (A)4.5μm, (B)6.0μm, (C)7.5μm, (D)9.0μm, (E)10.5μm and (F)12.0μm. Scale bar: 10 μm.

left to right and vice versa).

Despite this, it is useful to make a distinction in the population of cells. In Figure 5.4 a sequence of successive snapshots for the two representative case of random and persistent moving cells is shown. On one side are, cells with similar trajectories to a random walk ($k_a = 1, 2, 3\ s^{-1}$) characterized by several changes in the direction of displacement, see Figure 5.4 A for an example. And on the other side are cells that moves persistently ($k_a = 4, 5, 6\ s^{-1}$) through the microchannel device with a few directional changes in their trajectory, see Figure 5.4 B.

The cell trajectories in the x-axis as a function of time for the studied microchannel widths are shown in Figure 5.5. Each panel of Figure 5.5 exhibits representative samples of trajectories which stand for the different channel widths and reaction rate values.

Each color scheme used in the panels corresponds to a certain width of the system, whose precise value can be extracted from the box attached to the right of panel D in Figure 5.5.

Panels A, B and C of Figure 5.5 represent the characteristic random/unpo-

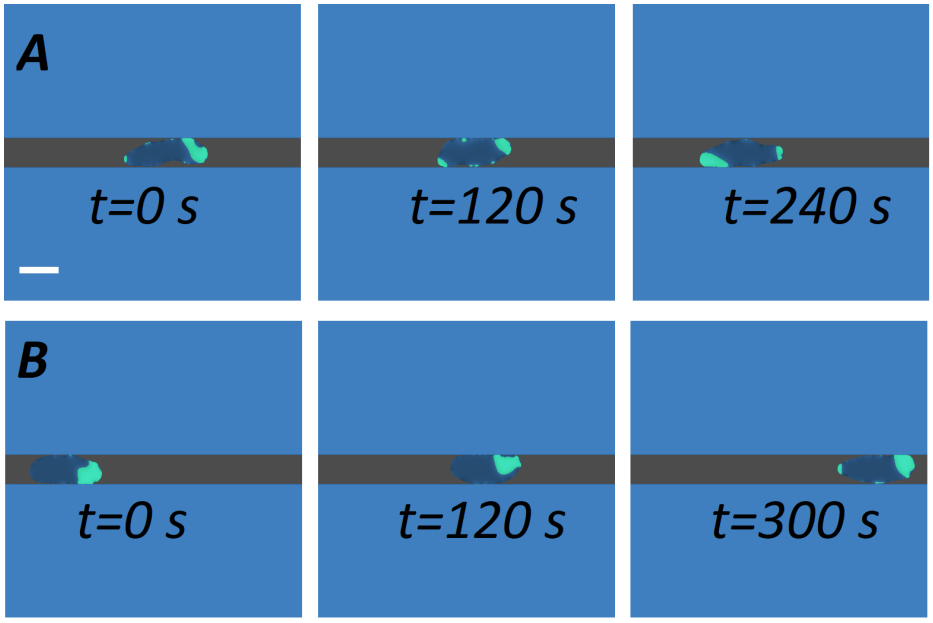

Figure 5.4: Sequencially snapshots for the two representative cell population of cells inside the microchannels. A) Represents the case for a random/unpolarized cell. B) Shows a persistent/polarized cell travleing inside the channel. Scale bar: 10 μm.

larized type motility cells which are characterized by frequent changes in the direction of displacement. The rest of the panels, from D to F, correspond to the starving/polarized cells. This trajectories, displayed principally as angled straight lines, demonstrate the clear persistence of movement mostly in one direction with a few changes of direction.

Finally, cell speed was also measured. Figure 5.6 displays the velocity in function of the channel width. A relation between the velocity and the width of a channel was found, allowing the conclusion that narrow channels tend to reduce the velocity, partly due to the lack of space that the cell experiences and in some cases related to the parameters selected in the model that directly affect the formation of more diverse biochemical concentration areas which are the responsible for producing protrusions and influencing the random cell displacement. However, in the representative cases for unpolarized cells (panels A, B and C of Figure 5.6), the velocity

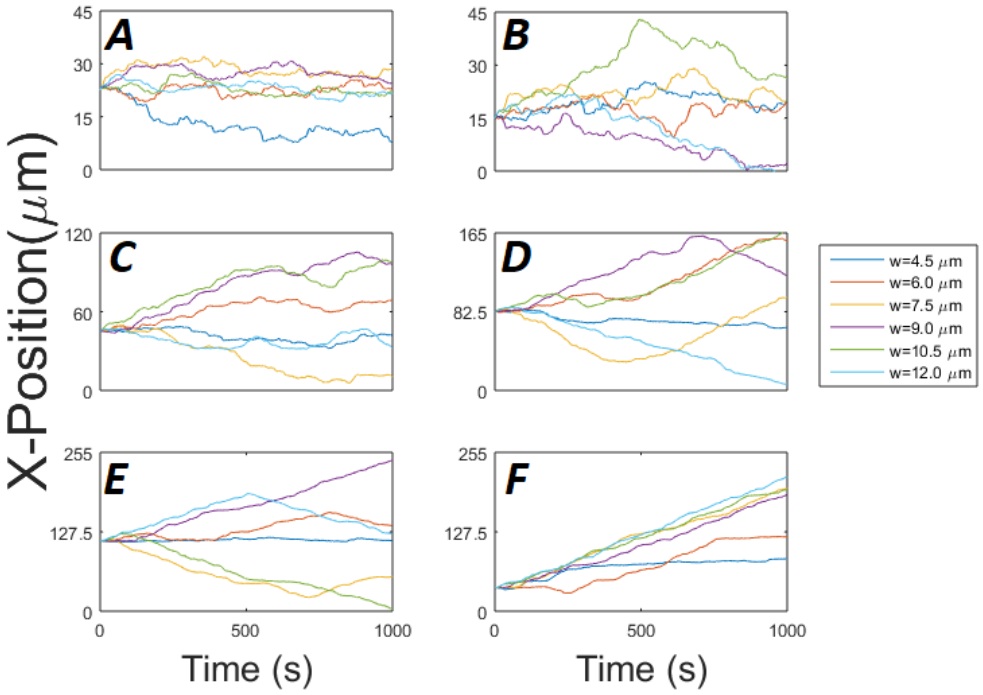

Figure 5.5: Horizontal axes positions of several trajectories for different reaction rate parameter and width size of the channel. In every panel the reaction rate varied from A) $k_a = 1s^{-1}$, B) $k_a = 2s^{-1}$, C) $k_a = 3s^{-1}$, D) $k_a = 4s^{-1}$, E) $k_a = 5s^{-1}$ and F) $k_a = 6s^{-1}$ with a separation of one unity between them.

measured for the different widths of the channel did not change significantly.

In contrast, for the polarized cells, the space increase of wider channels permitted the cell to move freely and more quickly inside the channel. This can be seen in a clear way in panels D, E and F of Figure 5.6 where the velocity rises as the size of the channel is increased.

5.4 Discussion

In general, for all the cases it was found that greater displacement was present in wider channels than in narrower ones. As consequence the migration displacement and speed was also partially suppressed in narrow channels.

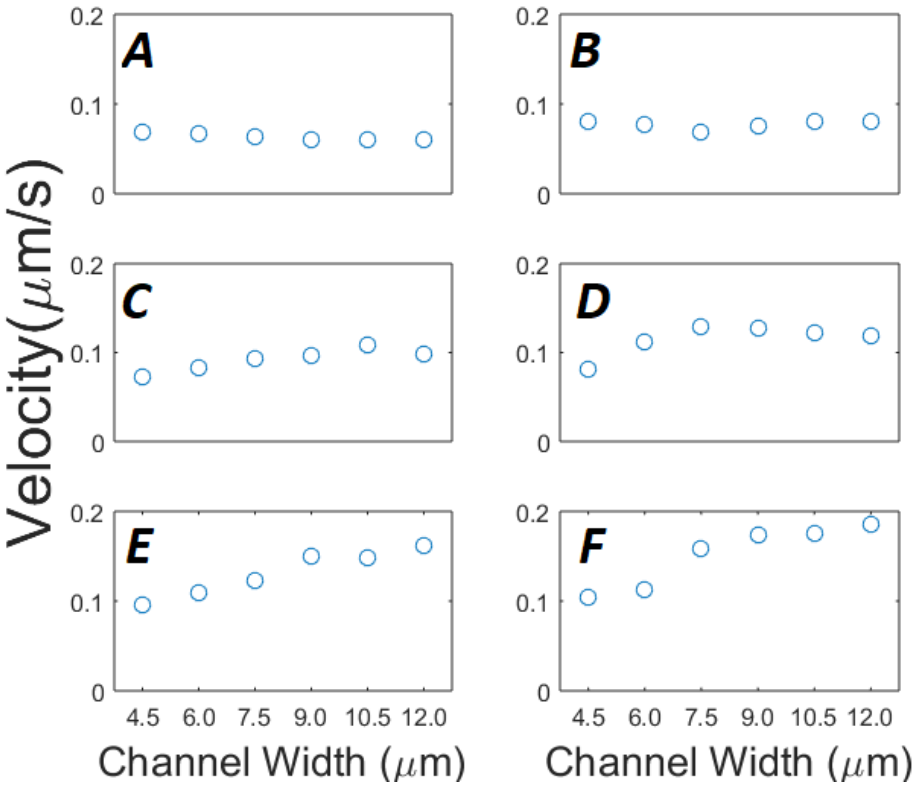

Figure 5.6: Mean measured velocities for different reaction rate ratio. Different width channels were shown in every panel, the reaction rate varied from A) $k_a = 1s^{-1}$, B) $k_a = 2s^{-1}$, C) $k_a = 3s^{-1}$, D) $k_a = 4s^{-1}$, E) $k_a = 5s^{-1}$ and F) $k_a = 6s^{-1}$ with a separation of one unity between them.

A more detailed comparison shows a qualitative agreement between some experiments previously observed and discussed in various studies [195, 203] and the results obtained from the simulations. One of the highlights is that the model of amoeboid motility under the influence of mechanical confinement exhibits certain forms of persistence/polarized and random/unpolarized displacement which have a dependence on the model parameters. One example that may be observed is that using small values of k_a, the model can reproduce scenarios in which cells move randomly and erratically inside the microchannel changing the direction of displacement with great frequency, while for high values of k_a, cells were able to polarize inside channels and to move in a persistent way for long periods of time in the same direction.

Many questions about the connection between migration and confinement remain. Despite the differences in the experiments and the types of cells that were used, some observations point to a greater velocity of cancer cells inside narrow channels and a decrease in velocity in wide channels [197]; alternatively, it has been observed that T cells and cancer cells reach a maximum velocity for an average width of a set of different width channels [194, 203]; finally, yet other experiments show a scenario in which narrow channels decrease the velocity of *Dictyostelium discoideum* cells [195].

However, the studies described above do not include gradient to stimulate cell migration. Others have included an external gradient, normally in the form of chemoattractant [191, 204, 205]. These results open up the possibility to extend the analysis previously made to include an external gradient in the model, similar to the experiments already mentioned [192].

Chapter 6

Coupled Ras-Pseudopod inducer model for a crawling cell

6.1 Introduction

An intensive use of physical and mathematical theories on pattern formation in extended systems [206, 207], gave rise to valuable arguments to explain the formation of certain biological structures. Such mathematical mechanisms have permitted the modeling of processes on very different spatial and temporal scales: from the formation of the skin in fishes [208], to the definition of the direction in embryonic developing [209].

Some mathematical models relay on a local excitation, which, combined with global inhibitions makes the cell respond to external gradients [105], while others rely on the accumulation of a certain biochemical components to guide the motion of the single cells [62]. Normally the accumulation re-

sponsible for this second mechanism is combined with a conservation constraint because the process of polarization is fast in comparison to the production of new biochemical components. With this restriction, the mechanism of pattern formation inside living cells together with the constraint of mass conservation is analogous to a process of coarsening of the initial nucleus of components [210] and gives rise to phase separation [211] and to models of pattern formation [212]. Several simple models of intracellular pattern formation have appeared that include the conservation restriction [62, 92, 213].

Once the axes and direction of movement are defined, small projections (defined as protrusions) are formed in the cell membrane [183]. These projections, which extend and retract periodically, are responsible for pushing the cell to move. Inside these projections several signaling events are triggered, for example activation of the Ras proteins and PI3K enzymes and accumulation of PIP_3 at the front of the cell, while activation of PTEN and myosin occur at the rear of the cell [214, 215]. Membrane areas where the protrusion activity is greater are typically characterized by the presence of Ras-GTP protein zones, denoted as patches [216]. The appearance of Ras regions around the membrane with high protrusion activity [51, 105, 217] has been observed in the slime mold organism *Dictyostelium discoideum* where it is related to cytoskeletal dynamics [218].

As described in previous chapters, a reaction diffusion model with bistable dynamics is one of the common models of cell motility. Some one dimensional bistable models are based in the formation of finite lifetime and localized patches of high protein concentration [219, 220] while others are based in membrane dynamics of moving connected points [221].

Here, first, it was transformed a one dimensional model of the polarization

at the membrane of a single *Dictyostelium discoideum* cell [51] into a two-dimensional domain for the waves in the basal membrane, in contact with the surface, using an additional phase field for the shape of the cell. One can observe a strong dependence of the numerical dynamics on the explicit parameter values of the original model and on the intensity of the stochastic fluctuations. Next, it was proposed a constrain on the conservation of a component of the signal pathway, controlling the autocatalytic mechanism, to increase the robustness of the model to changes on parameter values. Such types of conservation have been previously employed in other models of motion of *Dictyostelium discoideum* cells [69, 88, 89, 222], with the purpose to show that such constrain is an useful and reasonable condition to systematically increase the robustness of the crawling mechanism, increasing the window of parameters values allowing cell migration.

6.2 Biochemical model for Ras activation and pseudopod extension

A reaction-diffusion model [51] for Ras-GTP (R) patches that consist of a local activator and a global inhibitor enhanced by the activation of the Ras-GTP was studied; see diagram in Figure 6.1. The partial differential equations employed are:

$$\frac{\partial R}{\partial t} = (1-R)\left(k_1 + k_2\frac{R^{n1}}{R^{n1}+K_R^{n1}} - k_3 G_R - k_4 L_R\right) - k_5 R\frac{1}{1+k_6 P} + D_R\nabla^2 R + \xi_R(\vec{x},t), \tag{6.1}$$

$$\frac{\partial G_R}{\partial t} = k_7\langle R\rangle - k_9 G_R, \tag{6.2}$$

$$\frac{\partial L_R}{\partial t} = (1 - L_R)k_{10}R - k_{11}L_R + D_{LR}\nabla^2 L_R; \tag{6.3}$$

where $\xi_R(\vec{x}, t)$ is a Gaussian spatio-temporal distributed white noise with zero mean $\langle \xi_R(\vec{x}, t)\rangle = 0$ and correlation $\langle \xi_R(\vec{x}, t)\xi_R(\vec{x'}, t')\rangle = 2\sigma_R\delta(\vec{x} - \vec{x'})\delta(t - t')$. The variables L_R and G_R correspond, respectively, to local and global inhibitors of R. Finally, note that the quantity $\langle R\rangle$ corresponds to the spatial integration in the whole system of the field R.

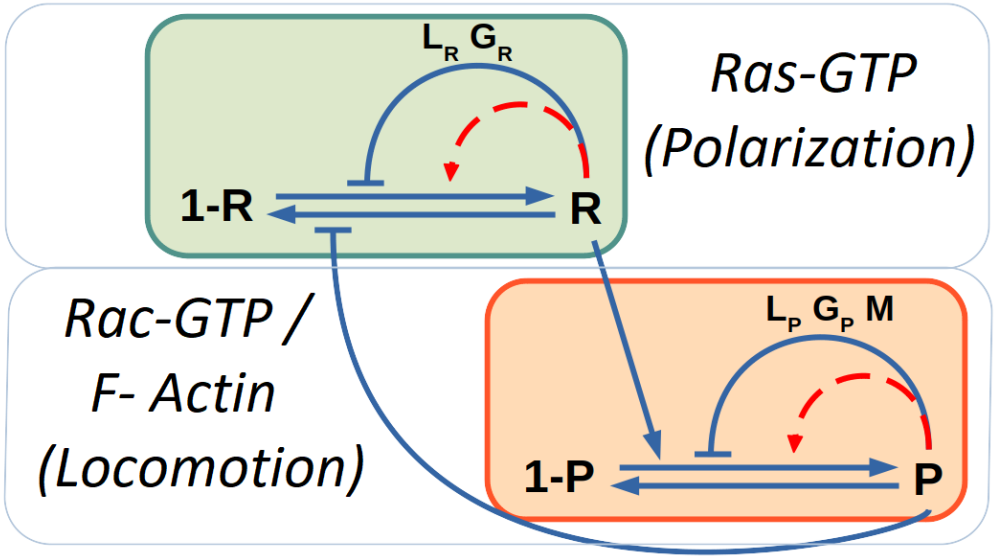

Figure 6.1: Sketch of the biochemical model of polarization and locomotion modules. Blue solid lines corresponds to the interactions and red dashed lines to auto-catalytic processes. The mass-conservation constrains control the auto-catalytic interactions.

At the same time it was included a quantity related to the formation of protrusions (P) such as F-actin and Rac-GTP molecules; see diagram in Figure 6.1. Also these variables were coupled with their respective inhibitors:

$$\frac{\partial P}{\partial t} = (1-P)\left(k_{12} + k_{13}R + k_{14}\frac{P^{n2}}{P^{n2}+K_P^{n2}} + k_{15}\frac{M^{n3}}{M^{n3}+K_M^{n3}} - k_{16}G_P - k_{17}L_P\right) \quad (6.4)$$
$$-k_{18}P + D_P\nabla^2 P + \xi_P(\vec{x},t),$$

$$\frac{\partial G_P}{\partial t} = k_{19}\langle P\rangle - k_{20}G_P, \quad (6.5)$$

$$\frac{\partial L_P}{\partial t} = (1-L_P)k_{21}P - k_{22}L_P + D_{LP}\nabla^2 L_P; \quad (6.6)$$

where $\xi_P(\vec{x},t)$ is a Gaussian spatio-temporal distributed white noise with zero mean $\langle\xi_P(\vec{x},t)\rangle = 0$ and correlation $\langle\xi_P(\vec{x},t)\xi_P(\vec{x'},t')\rangle = 2\sigma_P\delta(\vec{x}-\vec{x'})\delta(t-t')$. Equivalent to the previous set of equations, the variables L_P and G_P correspond, respectively, to local and global inhibitors of P.

Finally, the model takes into account the inclusion of a variable of memory (M) which is coupled with P; this variable stimulates the formation of new protrusion zones and represents the results observed in some experiments where a certain relation between the formation of new pseudopods in previous pseudopod locations is present [182, 223]:

$$\frac{\partial M}{\partial t} = k_{23}P - k_{24}M + D_M\nabla^2 M \quad (6.7)$$

For a more exhaustive description of the model, check the original study [51]. Note that the noise description in the original study was different and here it was adapted to an equivalent description based on physical derivations of stochastic fluctuations [111].

One dimensional simulations were made using periodic boundary conditions and using 120 points for the grid. The cell was considered as circular and having a radius of 6.25 μm. The pixel size for this case was set at $\Delta x = 0.32$ μm and the time step $\Delta t = 0.03s$. The definition and the value of the parameters of the model can be found in Table A.2.

6.3 Mathematical description of the mass-conservation constrain

The mathematical model described in equations (6.1-6.7) has several conservation terms which affect the dynamics of the system; see for example equation (6.2) and equation (6.5). However, a feedback control through the parameter k_2 and k_{14} to control the bistability shown by the model was included, which is discussed in next sections. Therefore, the parameters k_2 and k_{14} are dynamically controlled depending on the total amount of the protein R of inducer P at the cell, respectively.d

The new term control related to k_2 is

$$k_2 = k_2^* + \eta_1 \left(\langle R \rangle - C_R \right) , \tag{6.8}$$

also, in a similar way the control term for k_{14} read as follow

$$k_{14} = k_{14}^* + \eta_1 \left(\langle P \rangle - C_P \right) , \tag{6.9}$$

where k_2^* and k_{14}^* are new constants that replace k_2 and k_{14}, respectively, for η_1=0 one can recover the original model. Parameter C_R is the fraction of the cell area occupied by patches of Ras R and C_P is the fraction occupied by the pseudopod inducer P.

6.4 One dimension results of Ras model are based in stochastic generation of patches

In a one-dimensional system, mimicking the membrane of a crawling cell, the generation of a local patch of high biochemical concentration is equivalent to cell polarization. A stable domain in a specific location of the membrane is related with actin accumulation and produces persistent motion of the cell in like direction. The random appearance and disappearance of small domains is related with amoeboid motion, where two or three pseudopods compete for a certain time. The alternation of direction gives rise to random motion of the virtual cell.

Stochastic reaction-diffusion equations, as in equations(6.1-6.7), and previously developed [51], can be numerically integrated into a one-dimensional domain as in the original study. For certain window of parameter values, the spatio-temporal dynamics of concentration R displays relatively stable patches which appear at different locations; see spatio-temporal plots in Figure 6.2.

In the simulations shown in Figure 6.2, the parameters k_{14} and k_{18} are kept constant and the response of P along the membrane is quite similar for the parameters considered. There are some persistent patches during a long period of the simulations. Under such conditions the cell may develop its own locomotion. Note that the activation of P by R is weak; a strong coupling, controlled by parameter k_{13}, would correlate the patches of both fields. It was kept the original values of this parameter [51]. For small values of the parameter k_5 and large values of k_2, the concentration of R is high and homogeneously distributed along the membrane; see corresponding spatio-temporal plots in Figure 6.2. The concentration of R increases

the probability of the generation of patches of P, and therefore, depending on the particular realization, some direct motion is expected under such conditions. On the other hand, in the opposite limit, large values for parameter k_5 and small values for k_2, the concentration of R is low, and the probability of directed motion is smaller.

If we fix k_2 and k_5 values and vary the parameters controlling for the evolution of P, we obtain the inverse behaviour; see Figure 6.3. For large values of k_{14} and small values of k_{18} the membrane is completely covered by P, while for small values of k_{14} and large values of k_{18} the concentration of P strongly decreases. Locomotion is, therefore, expected for intermediate values of these two parameters as shown in Figure 6.3. However, the effect of changing such parameters on the dynamics of R is small.

6.4.1 Mechanism of amoeboid motion is based in bistability

For the evaluation of the mechanism of the spatio-temporal plots in Figures 6.2 and 6.3, we fixed the stochastic source of perturbations of the additive noises in eqs (6.1-6.7) to $\sigma_R = 0.04$ and $\sigma_P = 0.025$. No changes were expected in the average behaviour or in the quantification the value of the total concentration R in the face of the parameters k_2 and k_5 because the fluctuations are additive [111]. Stationary solutions were found for the deterministic version of equations (6.1-6.7). Slowly increasing the parameter k_2 we observed the evolution of the stationary value of R; see Figure 6.4. Once the system of equations saturated to a certain value of R$\sim 0.85 - 0.90$ we reduced the value of k_2, giving rise to a hysteresis cycle; see Figure 6.4A. The hysteresis cycle shows that the system actually follows bistable dynamics. Equivalent dynamics of R can be observed under

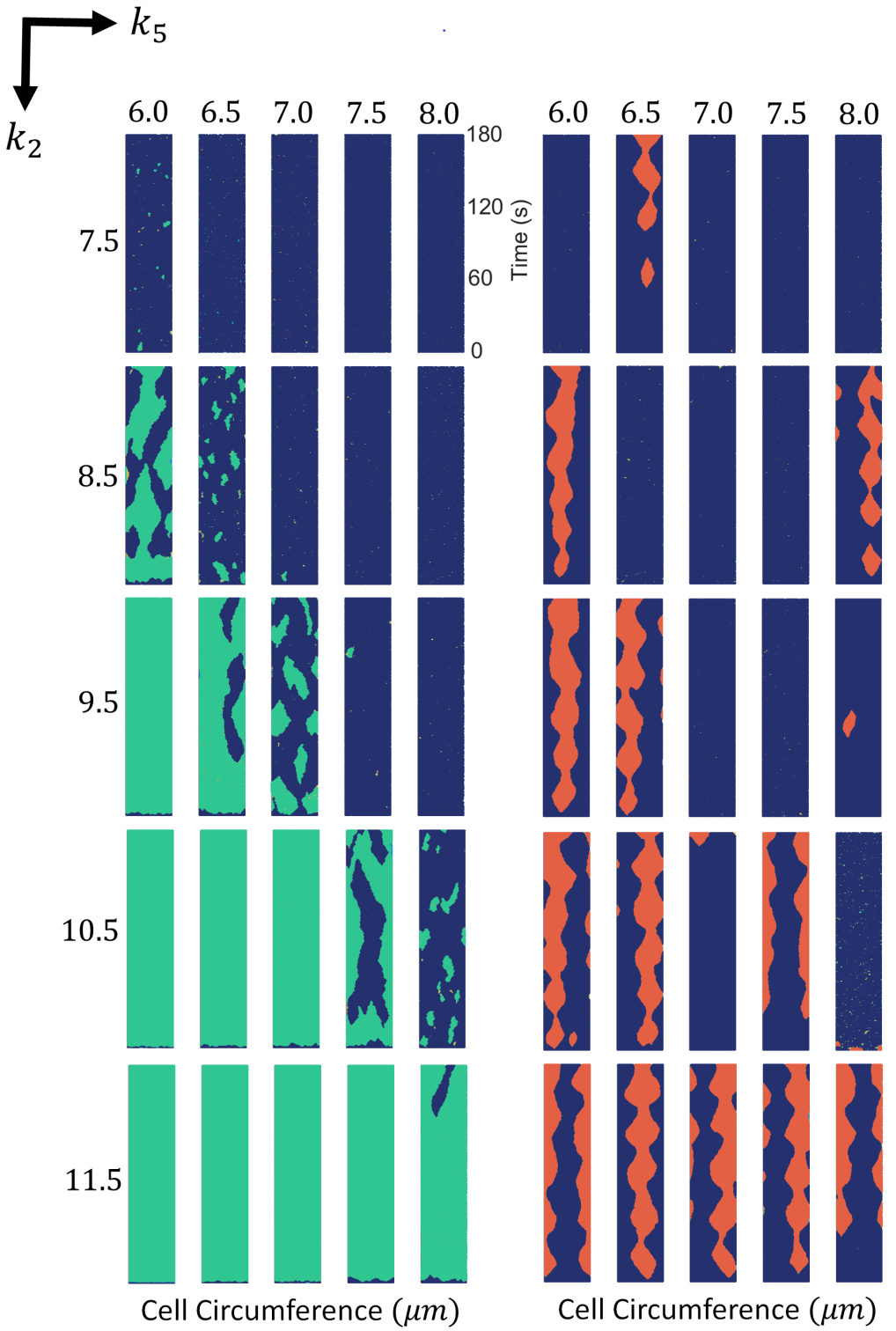

Figure 6.2: Spatio-temporal plots of R (in green) and P (in red) for different values of k_5 and k_2. Variance of noise intensity was fixed at $\sigma_R = 0.04$ and $\sigma_P = 0.025$.

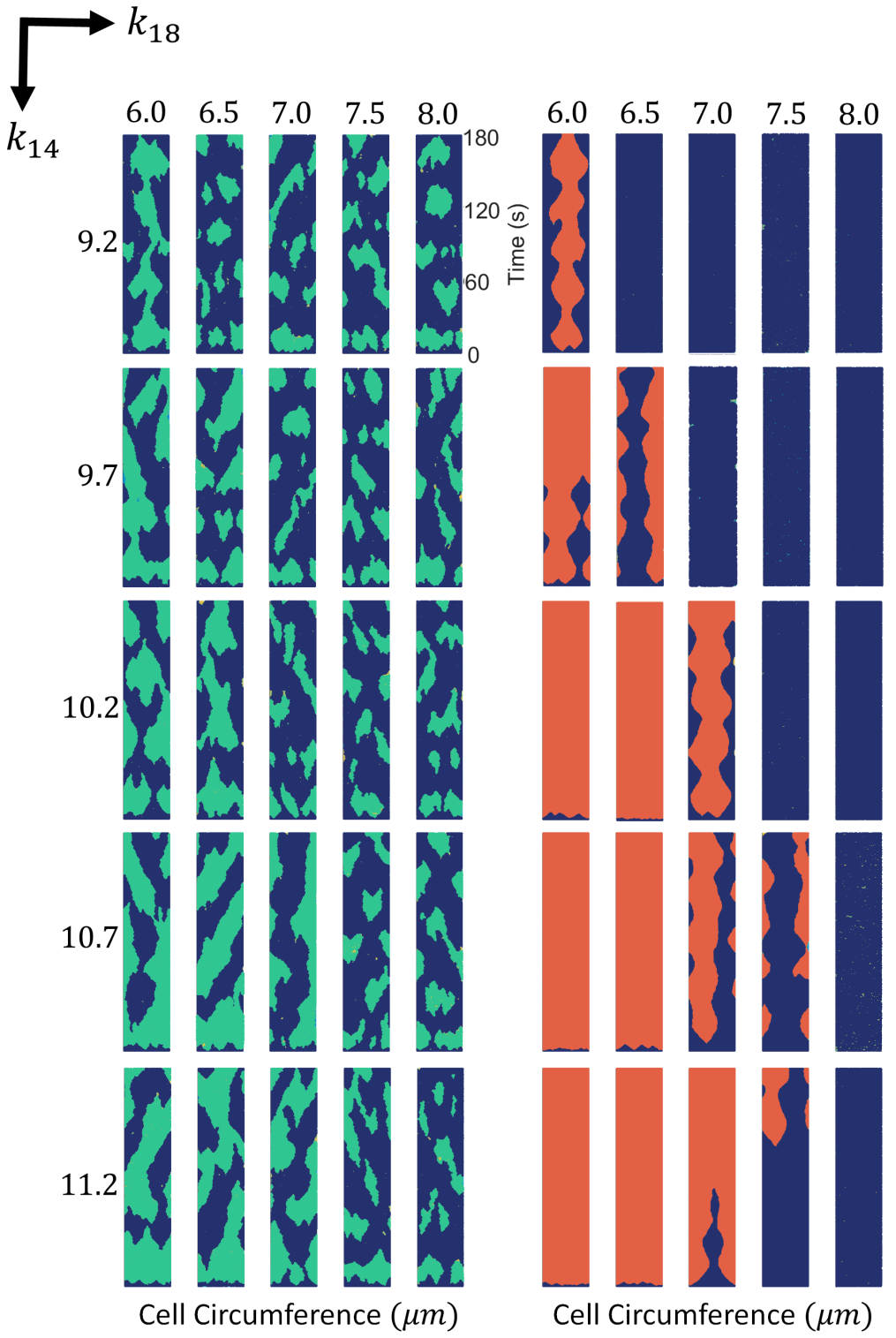

Figure 6.3: Spatio-temporal plots of R (in green) and P (in red) for different values of k_{14} and k_{18}. Variance of noise intensity was fixed at $\sigma_R = 0.04$ and $\sigma_P = 0.025$.

a similar change in k_5; see Figure 6.4B.

In contrast, the same analysis was made for the constants k_{14} and k_{18}, which are related to the variable of the pseudopod inducer P. The resulting dynamics revealed bistable behavior for two stable states as shown in the hysteresis curve for parameters k_{14} (Figure 6.4C) and k_{18} (Figure 6.4D).

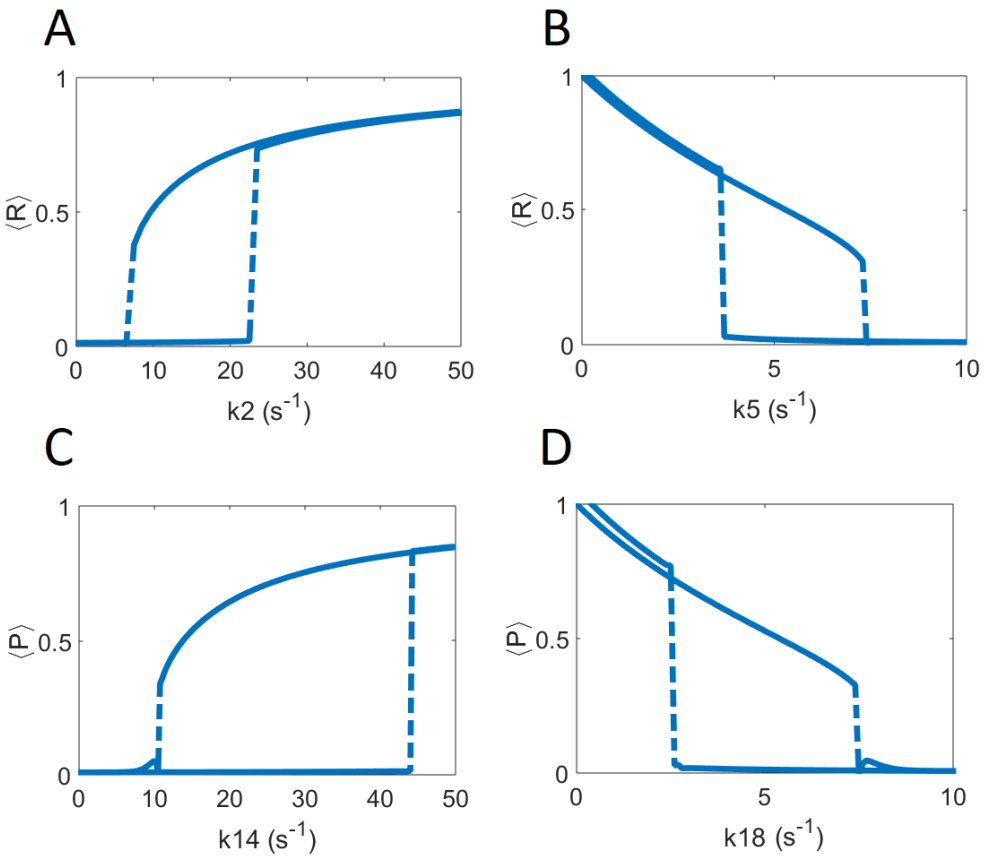

Figure 6.4: Hysteresis curves of the deterministic model for R dynamics varying (A) k_2 and (B) k_5. Similar hysteresis curves of the deterministic model for P dynamics were obtained when varying (C) k_{14} and (D) k_{18}.

It is known that the combination of a bistable dynamics with an appropriate noise intensity, producing the formation of localized patches in reaction-diffusion equations [224, 225]. This formation is the mechanism responsible for the formation of localized domains of R and P. The localized pattern observed in Figure 6.2 is not due to excitable dynamics but rather to bistable dynamics with noise.

6.5 Addition of a physical phase field model for cell shape deformations

The model originally does not include deformable cells, therefore, the system was expanded to 2D geometry by coupling the model to an auxiliary phase field ϕ with the purpose of describe the evolution of the cell shape. The equation for the phase field is described as follows

$$\begin{aligned} \tau \frac{\partial \phi}{\partial t} &= \gamma \left(\nabla^2 \phi - \frac{G'(\phi)}{\epsilon^2} \right) \\ &\quad -\beta \left(\int \phi \, dA - A_0 \right) |\nabla \phi| + \alpha \, \phi \, P \, |\nabla \phi| \ , \end{aligned} \tag{6.10}$$

where the difference respect to previous phase fields equations used previously (equation (2.1)) is in the third term which describe the active force generated by the Rac-GTP (P) molecules when pushing on the cell membrane [88].

The inclusion of the phase field as previously mentioned implies the change of geometry from 1D to 2D. Here, the cell was considered as a circle with radius equal to $6.25 \mu m$. The pixel size used was the half as in the 1D case $\Delta x = \Delta y = 0.16 \mu m$. Also, to increase the accuracy, the time discretization was reduced to $\Delta t = 0.003 s$. The equations (6.1-6.10) were integrated using periodic boundary conditions and standard finite differences. The rest of parameters are kept as displayed in Table A.2 and A.3.

6.6 Two dimensional stochastic bistable model provides a mechanism of cell crawling motion

For the coupling of the polarization mechanism to the proper cell motion shown in the previous section we used a phase field. This additional field is employed for the definition of the interior of the cell. In this case, the two dimensional phase field permits the use of different biochemical concentrations in the ventral part of the cell in a surface.

The extension of the stochastic reaction-diffusion described in the previous section to two dimensions permits numerical simulations of the shape of the crawling cell and the corresponding motion responding to the dynamics of the patches. In Figure 6.5 we see snapshots of the *in silico* cells with different parameter values corresponding to equivalent parameter values shown in Figure 6.2. We reproduced the dynamics expected from the one dimensional simulations and the crawling dynamics can be clearly studied. Again, for small values of parameter k_5 and large values of k_2 the concentration of R is mostly high and homogeneously distributed along the membrane; see Figure 6.5. On the other hand, in the opposite limit, for large values of k_5 and small values of k_2 the concentration of R disappears from the ventral membrane. However, for a small window of values of the parameters the cell moves and inspects the surrounding region. The shape of the resulting cell depends on the particular realization and the parameter values; in the snapshots shown in Figure 6.5 we obtain fan-shaped cells, a typical mode of Dictyostelium Discoideum cell crawling [117].

From the snapshots resulting from Figure 6.5 different scenarios show different types of movement together with the concentrations of R and P. The

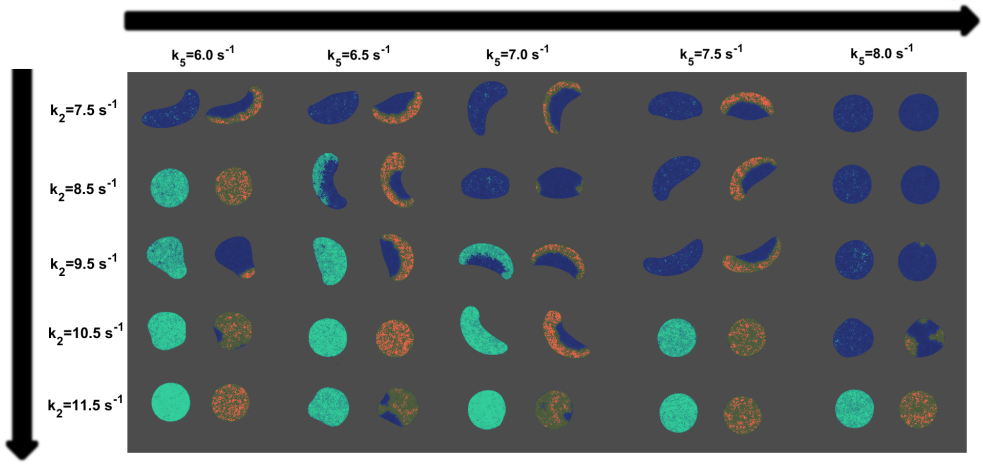

Figure 6.5: Snapshots of R (in green) and P (in red) dynamics obtained from computer simulations and applying the phase field technique to the model for different values of k_2 and k_5. Variance of noise intensity was fixed at $\sigma_R = 0.04$ and $\sigma_P = 0.025$.

model exhibits sensitivity to variations in parameters k_2 and k_5. Different realizations of simulations with the same parameters could bring the cell from quite persistent movement into an alternation between an almost static state for low concentrations of $\langle R \rangle$, and transitory motion in random directions for large values of $\langle R \rangle$. As in Figure 6.2 the small influence of R in P is evident in these two-dimensional simulations. Note that the presence of patches of P appearing for high values of k_2 and low values of k_5 is more common because $\langle R \rangle$ slightly increases the probability of forming new $\langle P \rangle$ patches. In contrast, for low values of k_2 and high values of k_5 the presence of $\langle P \rangle$ patches is less frequently observed.

In contrast to this, the dependence of locomotion on the parameters k_{14} and k_{18} is much stronger as shown in Figure 6.6, where persistent motion is observed only for intermediate values of the two parameters. For very small or very large amounts of $\langle P \rangle$ cells do not move, independently of the behaviour of R.

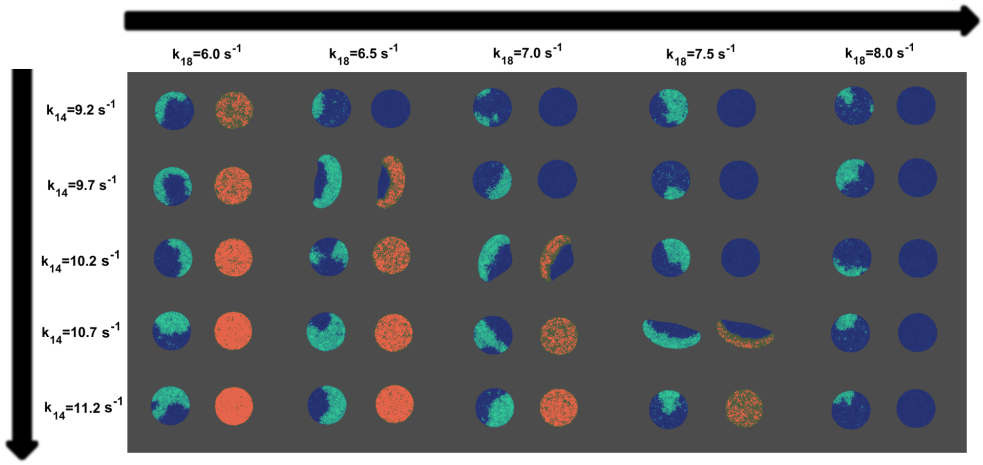

Figure 6.6: Snapshots of R (in green) and P (in red) dynamics obtained from computer simulations and applying the phase field technique to the model for different values of k_{14} and k_{18}. Variance of noise intensity was fixed at $\sigma_R = 0.04$ and $\sigma_P = 0.025$.

6.6.1 Noise intensities determine the type of motion

The variation of the type of cell motion is determined by the intensity of the noise. Low levels of both noises do not permit the formation of the domains of R and P needed to give rise to cell movement; see Figure 6.7. As we increase the amplitude of noise for P, we reach a single domain that fills the front part of the cell and persistent motion is shown; see middle column and right hand snapshots in Figure 6.7. This type of motion is reminiscent of the fan-shaped amoeboid cells previously reported [117] and also reproduced with simpler models [89]. An increase in the noise intensity produces an increase in the appearance and disappearance of pseudopods and therefore a transition to amoeboid movement; see fifth column in Figure 6.7 for higher noise intenisties. Another evident change the effects of which will be discussed in the following sections is the variance associated with the formation of Ras patches (σ_R) becoming varied. There are some noise intensities which produce patterns and dynamics similar to the characteristic patterns observed in the experiments, however, as previously mentioned,

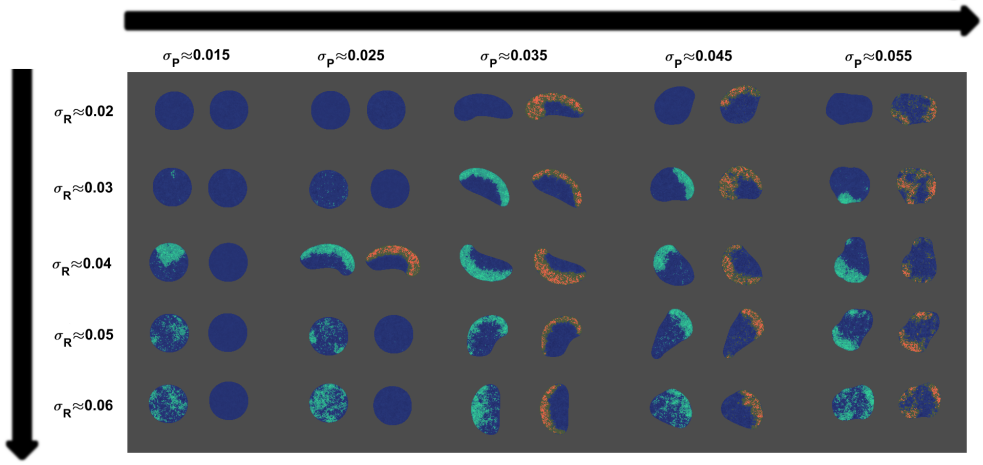

Figure 6.7: Map of snapshots taken from different variance values of noise intensity for the no mass conserved model. For every column, left/green snapshots refer to R dynamics while right/red snapshots indicate P dynamics. The value of the parameter of the simulations are $k_2 = 9.50$, $k_5 = 7.0$, $k_{14} = 10.20$ and $k_{18} = 7.0$. The rest of them are consistent with Table A.2 and A.3.

and shown in Figure 6.9, small variations in the parameter values may completely change the movement dynamics.

6.6.2 Inclusion of mass-conservation stabilizes cell motion

In order to reduce the high sensitivity of the movement on the parameter values, we included a conservation constraint on the total quantities of the protein Ras R and the inducer P in the biochemical rates responsible for the bistable transition. Following similar previous approaches [88, 222], we included this conservation as a global feedback condition in the reaction-diffusion equations.

In Figure 6.8 several realizations incorporating the conservation constraint of R and P proteins, for different parameter values are shown; see equations (6.8) and (6.9). A direct comparison can be made with the results displayed

in Figure 6.5. Results in Figure 6.8 show the effects of the inclusion of the mass conservation feedback, where a wide change in the parameter values does not affect either the bistability of the model or the quantity of protein R inside the cell phase field, which was kept constant. The incusion of this global condition permits the use of a larger range of parameter values, increasing the robustness of the mechanism in comparison with the non-conserved condition.

As with the cases without mass conservation, the shape and type of motion were affected by the noise intensity. Using the same parameters of Figure 6.7 we studied the effects of varying the noise variance in the mass conserved scenarios. In Figure 6.9 we see two different types of transitions. The first is observed when the variance related to the pseudopod inducer P increases, changing the shape from persistent fan-shape to random amoeboid phenotype. This change is present because while small values of P variance generates less blurred patches, an increment in the P variance drives the opposite effect, which is the appearance of more blurred and distributed patches for P.

For a second transition, we follow the same comparison line between the simulations without and with mass conservation from Figure 6.7 and Figure 6.9, respectively; now we analyze the effects for different values of the variance corresponding to the dynamics of the Ras concentration R. Similar to the patterns of P, small values of σ_R induce the formation of less diffuse and distributed Ras patches. In contrast, greater values of σ_R stimulate more diffuse and distributed Ras patches. Despite the close relationship between the effects of σ_R and σ_P, the real difference is in the dynamics of the movement. For example, if we focus on the top of the first column of Figure 6.9 for small values of the noise variances we see for both snapshots a domain in the front part of the cell which translates into persistent motion.

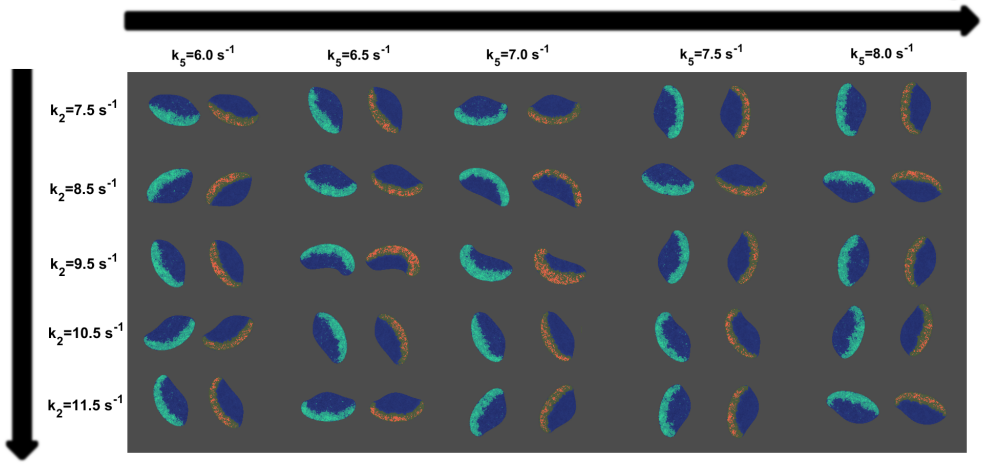

Figure 6.8: Snapshots of R (in green) and P (in red) dynamics obtained from computer simulations and applying the phase field technique to the mass conserved model for different values of k_2 and k_5. Variance of noise intensity was fixed at $\sigma_R = 0.04$ and $\sigma_P = 0.025$.

Now, if we look in detail at the bottom of the first column corresponding to higher a value for the variance σ_R, we see a notable difference in the left hand snapshots, moving from a more compact domain in the front part of the cell to a more diffuse domain inside the cell. This transition only takes place at the Ras concentration (R) level, while maintaining consistent dynamics of the pseudopod inducer P and thus persistent motion of the cell. The same analogy could be made for the last column in Figure 6.9 where high values of σ_P lead to a more random motion for all the cases regardless of the value of σ_R, the effect of which is to promote the appearance of less and more distributed Ras patches but without affecting the dynamics.

Figure 6.10 shows a kymogrpah for the two most characteristic cell phenotype obtained by the model coupled with a phase field, being the persistent fan shape characterized by the formation of more conjoined patches, see Figure 6.10A. And in the other side the amoeboid shape, which can be distinguished by the presence of more less continuous patches, see Figure 6.10B.

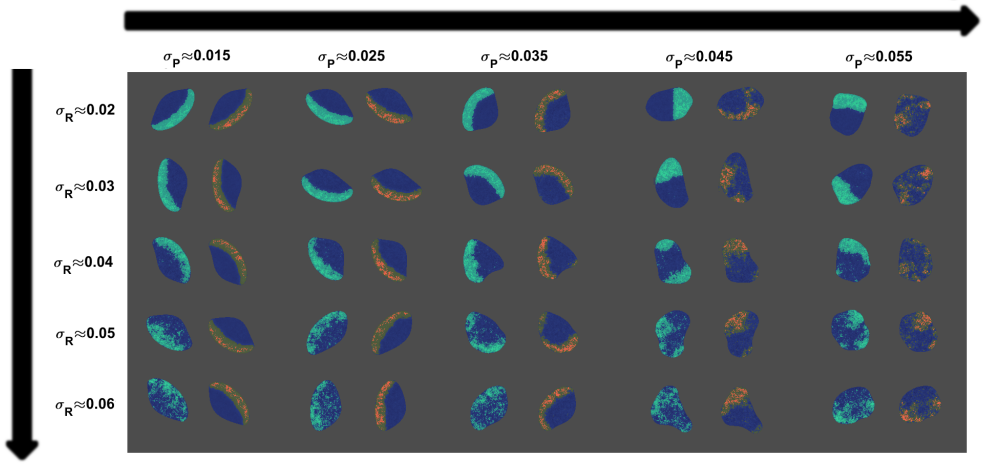

Figure 6.9: Map of snapshots taken from different variance values of noise intensity for the mass conserved model. For every column, left/green snapshots refer to R dynamics while right/red snapshots indicate P dynamics. The value of the parameter of the simulations are $k_2 = 9.50$, $k_5 = 7.0$, $k_{14} = 10.20$ and $k_{18} = 7.0$. The rest of them are consistent with Table A.2 and A.3.

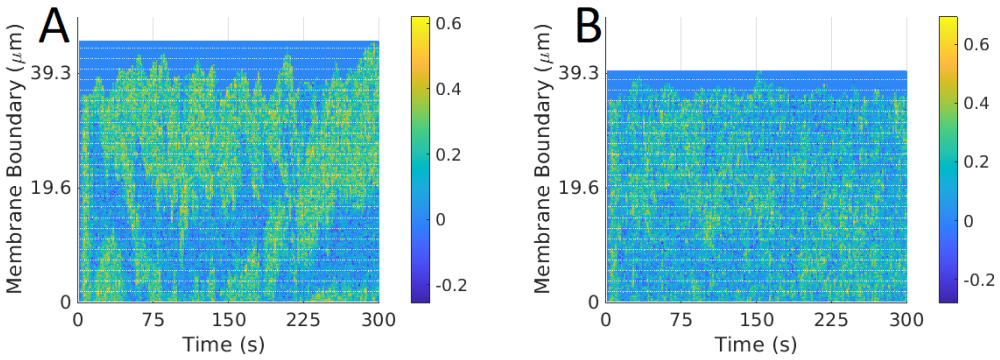

Figure 6.10: Kymograph for the two most representative cases of crawling cells obtained by the model. Panel A) shows a Persistent cell and B) an Amoeboid cell.

6.7 Mass-conservation constraint in the Ras model adds more robustness to the system

The use of the mass conservation condition has been previously employed for the generation of stable pattern formation on polarization process in single cells. Here, it is employed a version of such mechanism to modify a previous reaction-diffusion equations to incorporate restrictions on the conservation of R and P. It is also shown that such condition increases the window of parameters of the model to develop typical dynamics of cell crawling.

For the characterization of the mechanism we calculated the speed of the resulting cells for different parameter conditions for the non-conserved and conserved models. We observed that the dynamics of the simulated cells are more robust for the mass-conserved version of the equations; see Figure 6.11.

For the non-conserved version of the model the speed and shape drastically changes when varying the parameters, and every simulation reproduces different dynamics of crawling cells (see Figure 6.5). Furthermore, for the conserved version both velocities and shapes are more similar to each other for a much larger window of parameter values, as we can see in the speeds calculated in Figure 6.11. Results displayed in Figure 6.11A were obtained by changing k_5 to correspond to simulations shown in the third row of Figures 6.5 and 6.8. The dynamics are fixed because of the conservation condition. In contrast, Figure 6.11B was obtained by changing k_{18} to correspond to simulations shown in the third row of Figure 6.6 for the no mass conservation case (results not shown for the mass-conservation

system). Here one can see the preserving of the speed in the conserved system in comparison with the original model due to the small window of parameters, without the mass conservation condition that shows crawling dynamics.

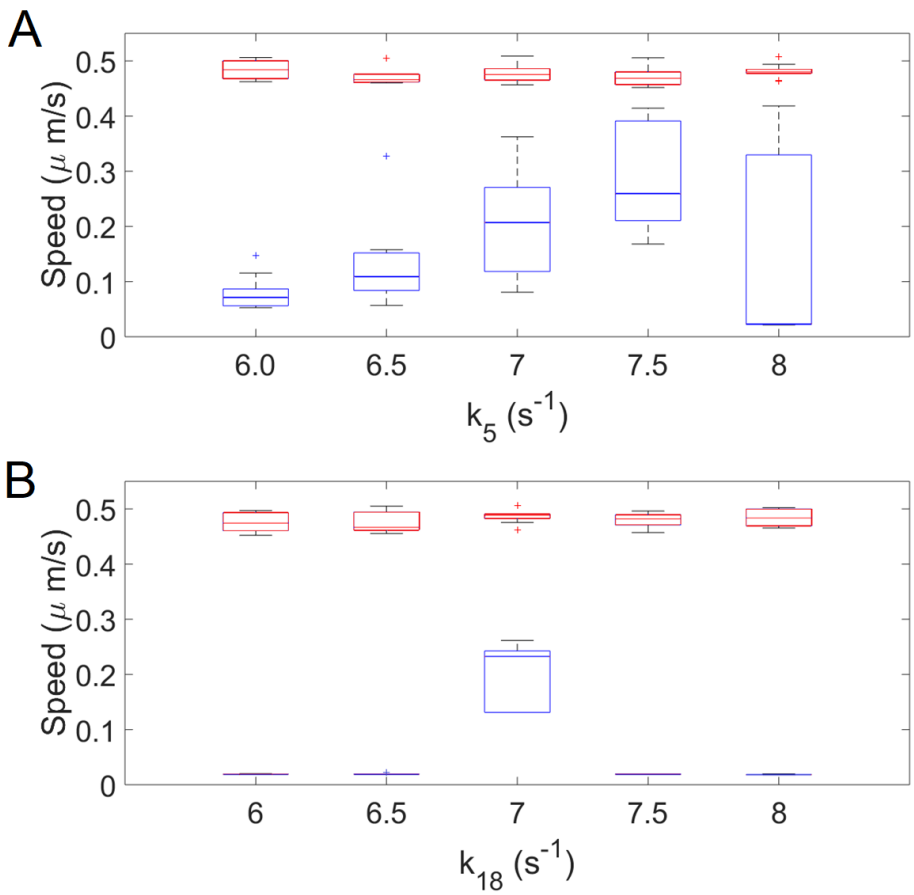

Figure 6.11: Box plot representation for the cell speed of the model without (blue color) and with (red color) mass conservation condition. Results are for when A) k_5 and B) k_{18} are varied. For both cases it was used a fixed value of $k_2 = 9.5$ and $k_{14} = 10.2$, $\sigma_R = 0.04$ and $\sigma_P = 0.025$. Ten realizations for each case were performed.

In Figure 6.12 we see the dependency of the speed on the noise σ_P for different values of σ_R. The speed of the cells employed for the calculation comes from the results in Figures 6.7 and 6.9. For the non-conserved outcome which is displayed in blue bars we do not observe a clear tendency in the bars. However, in contrast, in the mass conserved results, represented by red bars, a clearer tendency in the bars is noted.

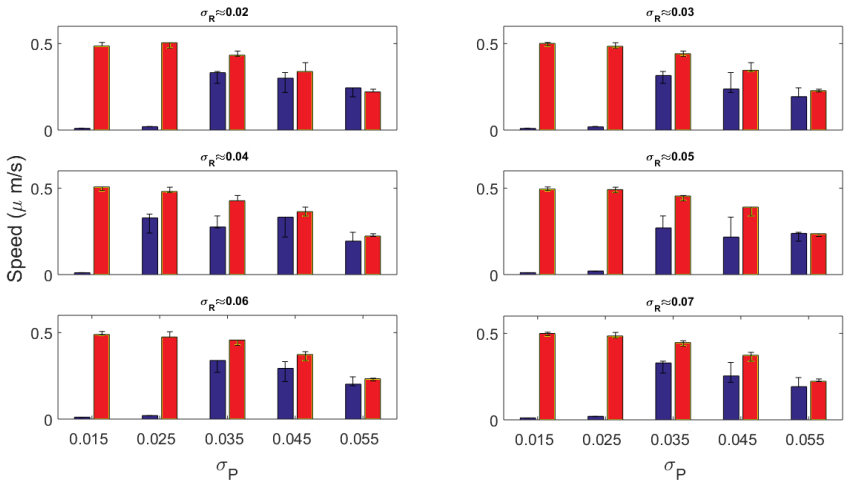

Figure 6.12: Speed bar plots measured by the no conserved (blue bars) and conserved (red bars) model by varying the noise variance σ_P. In each panel the variance associated to σ_R was fixed for different values.

We observe that the speed obtained from mass-conserved model decreases for greater noise intensities. However, for the set of blue bars almost null velocities appear for low noise magnitude, and as we increase the noise variance, different values close to the magnitude of the red bars are reached, thereby showing a similarity in the speed measurements as the variance is increased.

6.8 Influence of cAMP gradient on cell motility

An extension of the non conserved and conserved model is possible with the inclusion of an external chemoattractant gradient to analyze the response, known as chemotaxis and already considered in the original model [51] and studied previously in other experimental [226, 227] and modeling works [221, 228]. Next, some simulations which study the relation of the chemotactic motion of *Dictyostelium discoideum* cells with the stochastic

fluctuations and the rest of parameters will be shown.

The gradient used in the simulations was established as a slope with no cAMP on one of the sides of the grid and a maximal level in the opposite side of the gird. Different maximal values of cAMP ($c_{max} = 2-10nM/\mu m$) were considered for the different gradient steepness.

In Figure 6.15 two sets of sequential frames at different times of a cell without mass conservation and a variance corresponding to an amoeboid motion are displayed. On the left side column an example of a simulation without an external gradient is shown. From this set of snapshots its clear to observe the poor motility which is typical of an amoeboid cell. On the other hand, the snapshots in the right column illustrate a cell under the effect of a linear gradient of $c = 4nM$ over a surface of $131\mu m$. The gradient was established in the direction from left to right. The main characteristics of this group of snapshots is the formation of more patches at the side of the synthetic cell facing the highest cAMP concentration and the response of the cell to travel towards the direction of the gradient as time passes.

Complementarily to the results of Figure 6.15, in Figure 6.14 are shown different cell trajectories under the same parameter conditions as in Figure 6.15. The only difference between each trajectory is the variation of the gradient steepness.

The simulation results show that motility of the cell increased with increasing the steepness of the gradient. However, as in some experiments [191] a deep numerical study to measure the effects of the cell shape and velocity caused by a gradient under different conditions (*e.g., microchannels and groups of interacting cells*) can be a topic to investigate.

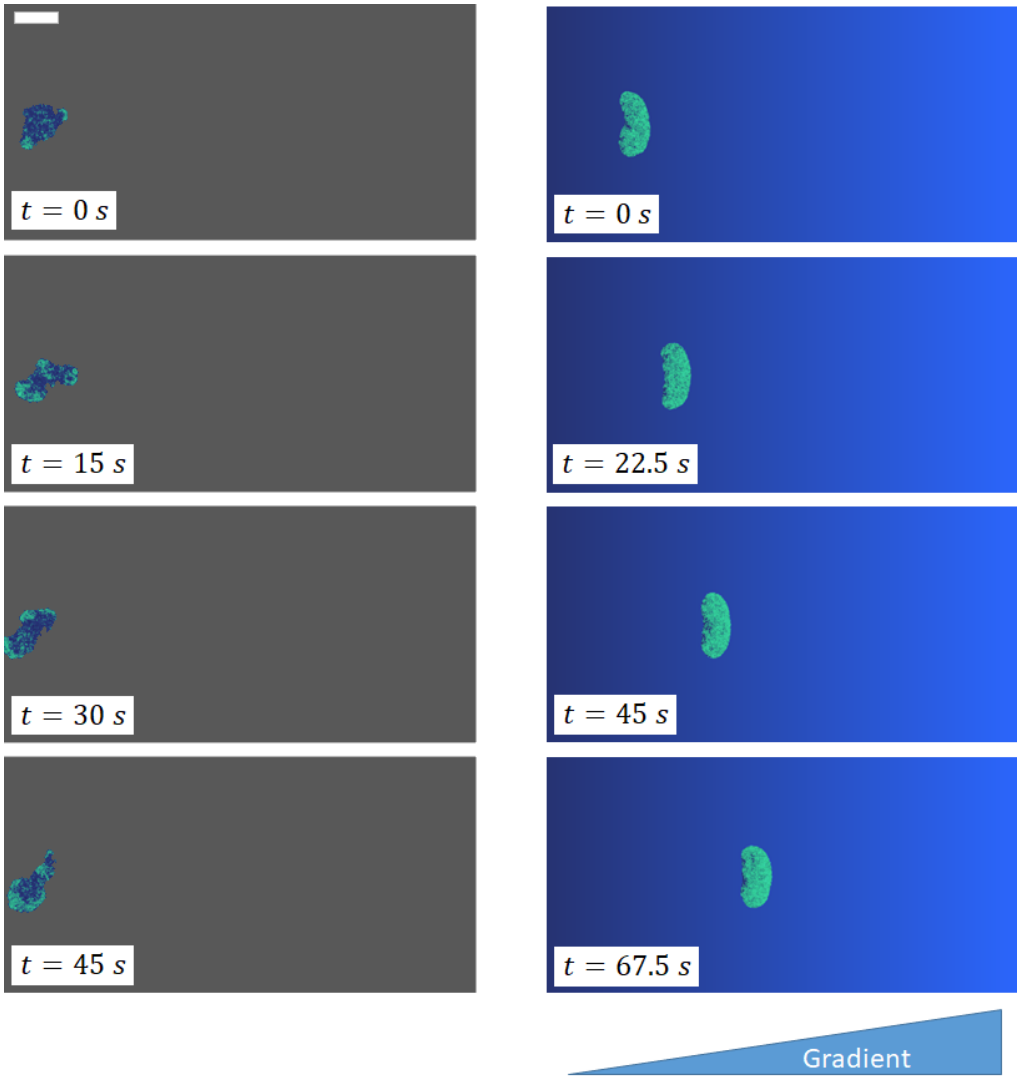

Figure 6.13: Time snapshots of an amoeboid type cell without the presence of an external gradient (left column) and under the presence of a linear gradient of $c = 4nM/\mu m$ (right column). Scale bar: 10 μm.

6.9 Discussion

We studied the dynamics of a one-dimensional *Dictyostelium Discoideum* cell model which is mainly made up of coupled Ras activation (R), pseudopod inducer (P) and stochasticity. The deterministic model by itself reveals the emergence of bistability. This is from the visible hysteresis transition under the change of a set of parameters. In contrast, the model with the stochastic part permits the transition between two stable regimes which

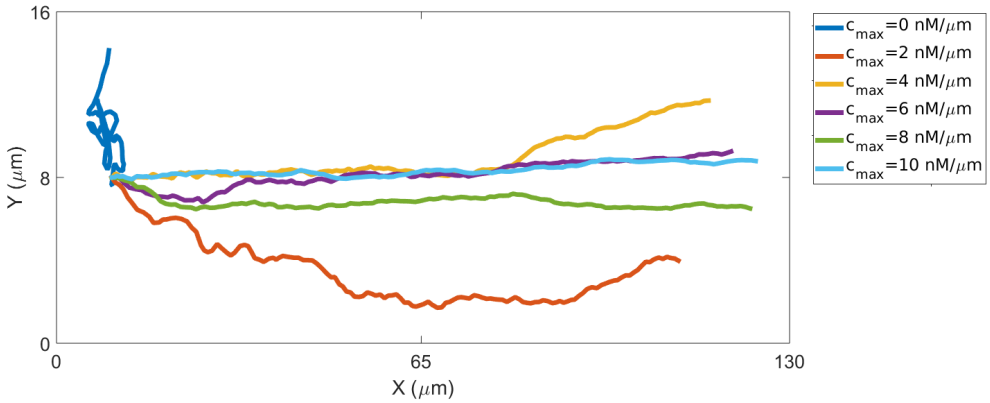

Figure 6.14: Simulated cell trajectories for different gradient intensity.

are induced by the parameters and the noise intensity. The extension of the model into two dimensions with the use of the addition of a phase field, allowing cell deformation, shows similar behaviour when parameters are varied to the one-dimensional model, in agreement with [51].

Since for most of the realistic scenarios the mass barely changes despite environmental perturbations, we chose to incorporate global feedback for the Ras and pseudopod inducer inside the cell. This increases the robustness of the model and expands the parameter range without affecting the shape and dynamics.

Note that other global feedbacks were already considered in the original version of the model [51]; see the dynamics of the global inhibitors, defined by G_R and G_P in equation (7.2) and equation (7.5) respectively, similarly to other models of the motion of *Dictyostelium discoideum* cells based on global cytosolic quantities [69, 105]. The addition of global control quantities which can determine the available concentration inside the cell has previously been employed in other models [77, 89, 222].

Instant speed was measured, highlighting that for the no conserved case a considerable set of parameters driven to velocities of close to zero, while for

the set of parameters for the conserved scenario the speed remained almost constant.

Note that it was shown that the original model is based in a bistable conditions with the adequate noise intensity. Similar simple stochastic bistable models for the description of the motion of *Dictyostelium discoideum* cells [88, 89] were used, which are based on the same concept together with a mass-conservation constrain. There are also other models based in similar constrains [222]. Therefore, such constrain is a convenient mechanism to gain robustness in the delicate equilibrium between stochastic fluctuations and a bistable condition.

Note that we have shown that the original model is based on a bistable conditions with the appropiate noise intensity. We have previously used simple stochastic bistable models for the description of the motion of *Dictyostelium discoideum* cells [88, 89] based on the same concept together with a mass-conservation constraint. There are also other models based on similar constraints [222]. Therefore, this constraint is a convenient mechanism to increase robustness in the delicate equilibrium between stochastic fluctuations and a bistable condition.

The coupling of R on the pseudopod inducer P is weak. The coupling is produced by the term proportional to k_{13} and it increases the probability of the generation of patches of P. A chemotactic concentration can enhance R and, therefore, polarize the field P and direct the locomotion [51]. In the absence of chemotaxis the coupling is small, while more physiological conditions may require larger couplings. In Figure 6.15 we increased parameter k_{13} to demonstrate the increase in the coupling of both field R and P through the parameter. Intermediate values can be compared with experimental measures to fit an appropiate value; however such evaluation

is outside the scope of this work.

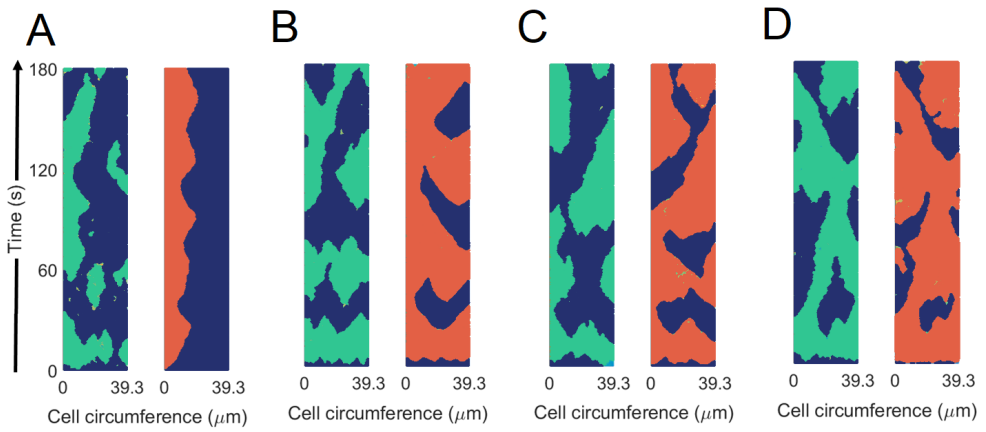

Figure 6.15: Spatio-temporal plots of R (in green) and P (in orange) for different values of the coupling parameter between R and P: $k_{13} = 0.1$ (A), $k_{13} = 0.5$ (B), $k_{13} = 1$ (C), and $k_{13} = 2$ (D). Results are for a fixed values of $\sigma_R = 0.04$ and $\sigma_P = 0.025$.

In summary, it has shown that the inclusion of a mass-conservation constrain in the correct position, substantially increases the robustness of a computational model of a crawling cell.

Finally, the addition of a chemoattractant cAMP gradient as already considered in the original one-dimensional model [51] to reproduce chemotaxis stimulates Ras activation which is one of the components that are coupled in the system.

Chapter 7

Biochemical excitability triggers symmetry breaking

7.1 Introduction

Exploring with detail the machinery involved in cell polarization, migration, division and in consequence cell symmetry breaking, require to describe several biochemical reactions in the interior of the cell [229]. At such levels of description the concepts of small G proteins (Ras GTPases) and phosphatidylinositol lipids PtdIns (e.g.,phosphatidylinositol (3,4,5)-trisphosphate PIP_3 and phosphatidylinositol (4,5)-bisphosphate PIP_2) appear, with all these molecules responsible for the accumulation on the cell membrane and on the reorganization of the cytoskeleton [230]. The accumulation of these molecules, in particular Ras, leads to the formation of pseudopods in the region with higher cAMP concentrations and as consequence the breaking of the symmetry due to the gradient of chemoattractant. However, the accumulation of these molecules in the membrane is also possible in the absence of the chemoattractant [216, 231].

Experimental evidence demonstrates that symmetry breaking signals can arise in a spontaneous way due to fluctuations in the internal excitability of the signaling network [218, 232]. Normally an excitable system has a threshold at which it responds to external stimuli, see section 1.2.1. The excitation after the stimulus is followed by a period of refraction during which the system cannot respond to a new stimulus. A characteristic of excitable systems is exhibiting traveling waves or oscillations for certain threshold conditions [233]. For these features to appear, two feedback mechanisms are required: first, positive feedback for the response to a stimulus and second, a delayed negative feedback for the temporal response followed by the refractory period.

Chemoattractant signals in *Dictyostelium discoideum* cells trigger activation of the excitable signaling system [234, 235]. Such signals are mediated by the G proteins and Ras-GTPases. Ras-GTPases are responsible for activating the phosphoinositide 3 kinase (PI3K), and, at the same time, this enzyme triggers the production of PIP_3 from PIP_2, both located at the cell membrane [230]. In addition, the phosphatase and tensin homolog (PTEN) contributes to the reverse reaction, producing PIP_2 from PIP_3. This reaction is present predominantly in areas where the effect of pseudopod formation and the chemoattractant is low.

Considering the scenario with two stable states where the cell is rich in PIP_2 and PIP_3, the system can be considered a bistable medium. Thereby, if positive feedback is added it is possible to stabilize the signal arising from the excitability of the Ras. Once the two processes are coupled it is possible to recreate the intracellular symmetry breaking network.

7.2 Modeling cell symmetry breaking in a $Ras - PIP_3$ system

Diverse nonlinear mathematical models have been proposed to explain the intracellular dynamics in excitable systems [105, 236]. Although these models describe fundamental behavior of the intracelullar signaling system, the explanation for all the variety of spatiotemporal dynamics under isotropic conditions, including the formation of persistent and temporary traveling domains of PIP_2 and PIP_3 [231], is complicated.

With the use of a set of coupled reaction diffusion equations the dynamics of $PIP_3, PIP_2, PTEN, RAS_{GDP}$ and RAS_{GTP} can be reconstructed in a numerical simulation to describe the influence of Ras excitability in the process of spontaneous symmetry breaking during cell migration.

Here, the original model proposed in [93] is employed, based on experimental observations. As mentioned before, positive feedback and delayed negative feedback were used to model Ras excitability [232, 237].

A conservative system for the production of PIP_3 was considered. PIP_2 phosphorylation to PIP_3 is catalyzed by PI3K, according to a simple Michaelis-Menten type equation. In a similar way, dephosphorylation from PIP_3 to PIP_2 by PTEN was contemplated as a Michaelis-Menten reaction. Finally, the process by which PTEN is attached to the membrane via interaction with PIP_2 and detached from the membrane by interaction with PIP_3 is also described as a Michaelis-Menten reaction.

Since bistability is reached in the PIP_3 - PTEN system, this state is subordinate to the RAS-GTP excitable state because of the interaction between RAS-GTP and PI3K that consequently provides travelling waves. The

whole excitable network is completed with various Ras-GTPase proteins, Ras, GEFS and GAPS, where GEFS and GAPS regulate Ras-GTPase in a positive and negative way, respectively, and causing an excitation state when the system exceeds the threshold.

As mentioned before, excitability and wave pattern formation arise from the Ras network. The dynamics of PIP_3 follows Ras-GTP and the reverse feedback maintains the excitability of the system. Thus, the evolution of the PIP_3 signaling is described as:

$$\frac{\partial PIP_3}{\partial t} = R_{PI3K} - R_{PTEN} - \lambda_{PIP_3} PIP_3 + D\nabla^2 PIP_3, \tag{7.1}$$

$$\frac{\partial PIP_2}{\partial t} = R_{PTEN} - R_{PI3K} + \lambda_{PIP_3} PIP_3 + D\nabla^2 PIP_2, \tag{7.2}$$

$$\langle PIP_3 \rangle + \langle PIP_2 \rangle = \langle PIP_{tot} \rangle, \tag{7.3}$$

where the reaction terms are described as Michaelis-Menten dynamics:

$$R_{PI3K} = V_{PI3K} PI3K \frac{PIP_2}{K_{PI3K} + PIP_2}, \tag{7.4}$$

$$R_{PTEN} = V_{PTEN} PTEN \frac{PIP_3}{K_{PTEN} + PIP_3}, \tag{7.5}$$

the two enzymes responsible for phosphorylation and dephosphorylation follow the dynamics below:

$$PI3K = \beta(RasGTP), \tag{7.6}$$

$$\frac{\partial PTEN}{\partial t} = -R_{PTEN} + V_{PTEN_{ass}} PTEN_{cyt} \left(\frac{PIP_2}{K_{PIP_2} + PIP_2} \right) + D\nabla^2 PTEN, \tag{7.7}$$

$$PTEN_{cyt} = PTEN_{tot} - \chi\langle PTEN \rangle. \tag{7.8}$$

where as indicated in equations (7.1) and (7.2), PIP_3 is generated from the phosphorylation of PIP_2 via PI3K (R_{PI3K}) and in the opposing way PIP_2 arises from the dephosphorylation of PIP_3 via PTEN (R_{PTEN}), respectively. The addition of a PIP_3 degradation rate, λ_{PIP_3}, which is related to the observation made in the PTEN-null strain, was included. A diffusion term for PIP_3 and PIP_2 is also added. The sum of PIP_3 and PIP_2 concentrations remains constant (equation (7.3)).

The equations related to the processes of PIP_2 phosphorylation reaction (R_{PI3K}) and PIP_3 dephosphorylation reaction (R_{PTEN}) are shown in (7.4) and (7.5), respectively. It is important to note that equations (7.4) and (7.5) were described as Michaelis-Menten enzymatic reactions where for each equation the addition of the reaction rates (V_{PI3K} and V_{PTEN}) and the Michaelis constant (K_{PI3K} and K_{PTEN}) was made. Due to the PI3K exchange between the cytosol and the membrane, a $RasGTP$ dependent $PI3K$ translocation-activation is introduced in equation (7.6). Parameter β is related to the proportionality among membrane association rates of PI3K and Ras-GTP level.

Equation (7.7) describes the interaction exchange of PTEN between cytosol and membrane, assuming this interaction to be a result of PTEN membrane dissociation rate and similar to dephosphorylation (R_{PTEN}). Additionally, in PTEN recruitment, by coupling the interaction within PIP_2, a reaction rate $V_{PTEN_{ass}}$ and Michaelis constant K_{PIP_2} was introduced. As a complement, in equation (7.8) there was considered to be an uniform PTEN concentration in the cytosol, and χ indicates the constant related to transforming the surface concentration on the membrane into a volume concentration in the cytosol. And as the final note on this part of the model, the angle brackets notation in equations (7.3) and (7.8) refers to the average concentration of the quantities involved.

Next part of the model follows the construction of an excitable network based on Ras signals [232]. The equations are given as follow:

$$\frac{\partial RasGDP}{\partial t} = R_{GAP} - R_{GEF} + k - \lambda_{RasGDP} + D\nabla^2 RasGDP, \tag{7.9}$$

$$\frac{\partial RasGTP}{\partial t} = R_{GEF} - R_{GAP} - \lambda_{RasGTP} + D\nabla^2 RasGTP, \tag{7.10}$$

where the reactions are:

$$R_{GEF} = \left(V_{GEFS} + \frac{V_{feedback} PIP_3}{K_{PIP_3} + PIP_3}\right)\left(\frac{RasGDP}{K_{GEFS} + RasGDP}\right), \tag{7.11}$$

$$R_{GAP} = V_{GAPS} GAPS \left(\frac{RasGTP}{K_{GAPS} + RasGTP}\right), \tag{7.12}$$

and the dynamics of the enzyme:

$$\frac{\partial GAPS}{\partial t} = V_{GAPS_{ass}} GAPS_{cyt} \left(\frac{RasGDP}{K_{RasGDP} + RasGDP} \right) \left(\frac{K_\alpha + \alpha_1 RasGTP}{K_\alpha + RasGTP} \right) - \lambda_{GAPS} GAPS + D\nabla^2 GAPS, \tag{7.13}$$

$$GAPS_{cyt} = GAPS_{tot} - \chi \langle GAPS \rangle. \tag{7.14}$$

The second part of the model couples a positive and a negative regulator of Ras as GEF and GAPS, respectively. Here, Ras is activated by the R_{GEF} reaction and inactivated by the R_{GAP} reaction. At the same time RasGDP is consumed and supplied by membrane dissociation and association at the rates λ_{RasGDP} and k, respectively, see equation (7.9). A similar reaction is described in equation (7.10), where RasGTP dissociates from the membrane at λ_{RasGTP}. Equations (7.11-7.12) are described as enzymatic reactions with their respective reaction rates and Michaelis constants. This formulation is the result of the experimental observations which indicates that PIP_3 production influences the formation of Ras waves.

The introduction of a positive regulation from RasGDP and negative regulation from RasGTP promotes the formation of RasGTP patches. These regulations were described as two positive feedback loops, with the positive regulation described as an MM-type enzymatic reaction with a reaction rate $V_{GAPS_{ass}}$ and a Michealis Constant K_{RasGDP}, and the negative based on [231]. Additionally, the degradation of GAPS was introduced at rate λ_{GAPS}, see equation (7.13). Finally, in equation (7.14), a GAPS uniform concentration inside the cytosol was considered, where χ has the same

meaning as in equation (7.8).

Deterministic simulations of the model (equations (7.1-7.14)) in one dimension were performed in a grid of 100 points along the membrane to reconstruct the kymographs shown below. Additionally, stochastic simulations of the model were made in the framework of the Langevin equation. The radius of the cell was set at $5\mu m$, which means that $dx = 0.3141\mu m$. Finally, a time step of $\Delta t = 0.005s$ was chosen.

Complementary to the one-dimensional system, a two dimensional analysis with the use of a phase field was also considered, with the same cell radius of $5\mu m$ and time step $\Delta t = 0.005s$, while $dx = 0.1570\mu m$. The parameters used in the simulations are summarized in Table A.4.

7.3 One dimensional results for the symmetry breaking Ras-PIP_3 system

The kymographs for deterministic (Figure 7.1A-B) and stochastic simulations (Figure 7.1C-D) show that with the excitability present in the model one can successfully reproduce the travelling waves of PIP_3 (left column) and Ras-GTP (right column) observed in the experiments of Fukushima's study [93].

If no PI3K activity is assumed, because of the excitability one can reproduce Ras-GTP waves, but the waves related to PIP_3 (and PIP_2) disappear in the period of inactivation of PI3K; see kymographs of Figure 7.2A-B and Figure 7.2C-D for a deterministic and stochastic simulations, respectively. This shows that Ras triggers the waves through interaction with PI3K. In addition, during the period when PI3K is active the Ras-GTP and PIP_3

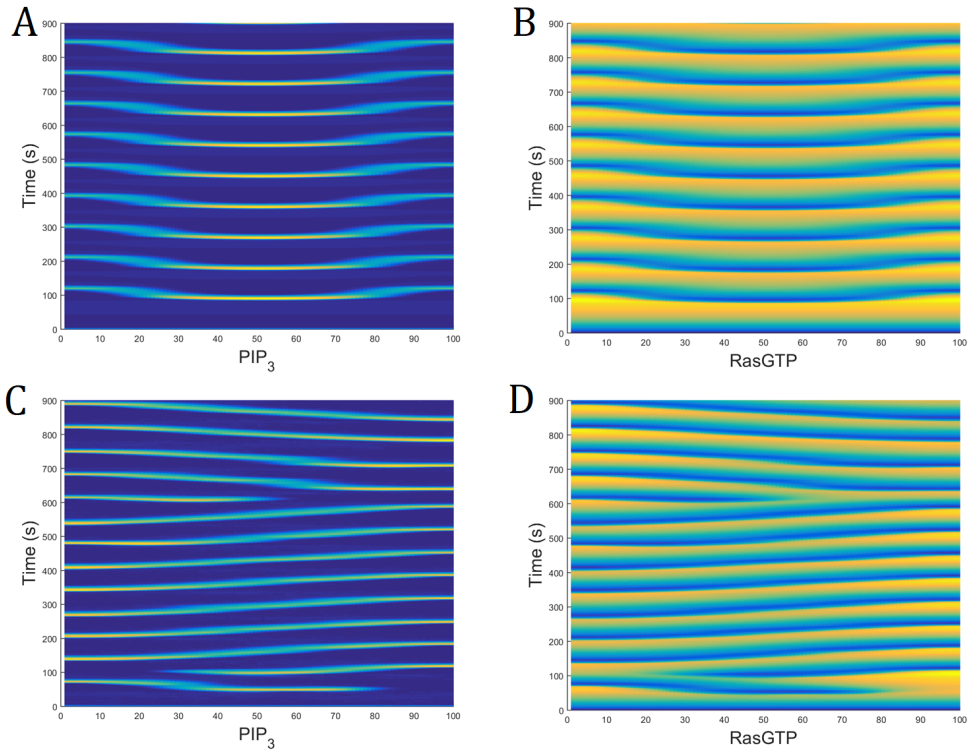

Figure 7.1: A)PIP_3 and B)Ras-GTP waves for deterministic simulations. In other side, C)PIP_3 and D)Ras-GTP waves for stochastic simulations. Activation rate of Ras by GEFS was set to $V_{GEF} = 450s^{-1}$.

waves are coupled in a similar way, with the only difference being in the wave period of the Ras-GTP due to the positive feedback from PIP_3 to Ras.

To examine the relation between the Ras-GTP and PIP_3 feedback in greater detail, simulations were performed with different values of V_{GEFS}, which is responsible for the basal activity of GEFS. One characteristic of these results is the addition of the activation and deactivation of PI3K during half of the simulation and observing how this change affects the Ras waves. For each panel in Figure 7.3 kymograph simulations with different V_{GEFS} values are displayed, corresponding to the panels in the left column to deterministic simulations, while the right column is representative of the stochastic simulations. The results show a dependence between the Ras waves and V_{GEFS} magnitude. At low $V_{GEF} = 450s^{-1}$ (first row in

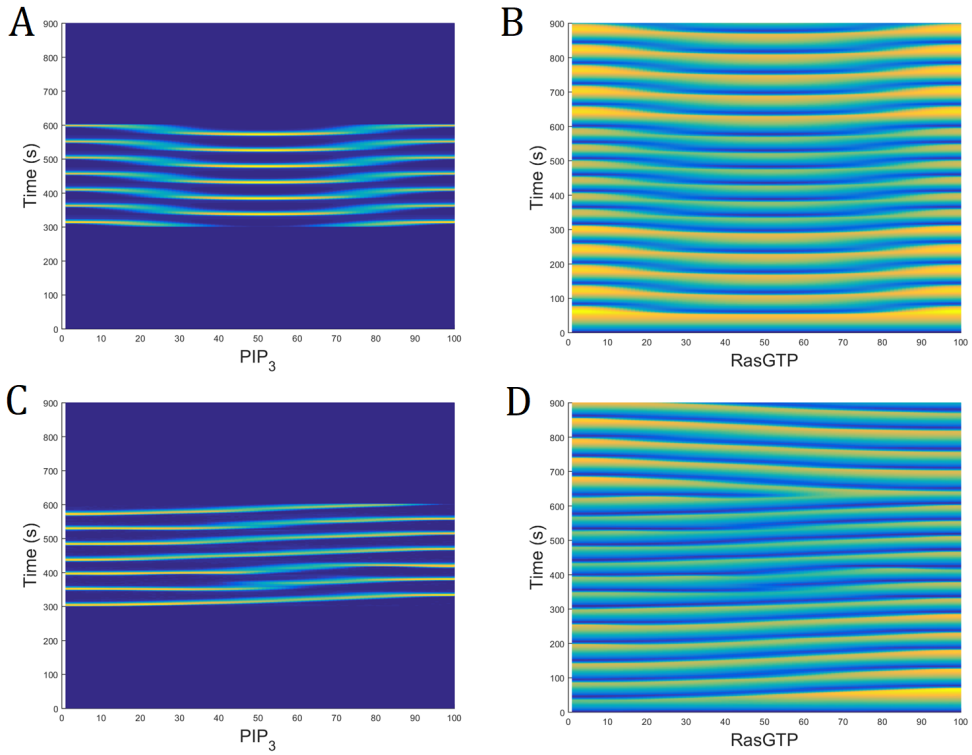

Figure 7.2: Deterministic simulations of A)PIP_3 and B)Ras-GTP waves. Panels C) and D) correspond to stochastic simulations of PIP_3 and Ras-GTP, respectively. For both, deterministic and stochastic cases no PI3K activity was assumed during two periods of time, corresponding from 0 to 300 seconds and from 600 to 900 seconds; periods where the PIP_3 wave activity was ceased. An activation rate of Ras by GEFS of $V_{GEF} = 600s^{-1}$ was considered.

Figure 7.3), no wave recovery activity was found before the deactivation of PI3K in a deterministic simulation, in contrast to the stochastic simulation where the noise helps the system to enter an excitable state and in consequence Ras waves appear. In the same frame, after the PI3K deactivation, the deterministic and stochastic scenarios show no presence of Ras waves. This may be explained by the effect of small V_{GEFS} and PI3K inhibition which imposes a greater distance in order to reach the excitability threshold.

Intermediate values of $V_{GEF} = 500s^{-1}$ are shown in the second row of Figure 7.3. In the deterministic case one can see that the system reaches the

excitability threshold, but once more, after the deactivation of PI3K this threshold becomes larger and the excitation is not recovered. In contrast, in the stochastic case after the inhibition of PI3K, the noise activity and the loss effect of the negative feedback on Ras help the system to recover excitation.

Finally, in the third and fourth row of Figure 7.3 are shown the simulation results with values of $V_{GEF} = 550s^{-1}$ and $V_{GEF} = 600s^{-1}$, respectively. Here the Ras waves never vanished. This effect is the result of the model entering high Ras-GTP basal levels, reducing the threshold to reach excitability, independently of whether PI3K is active or inactive.

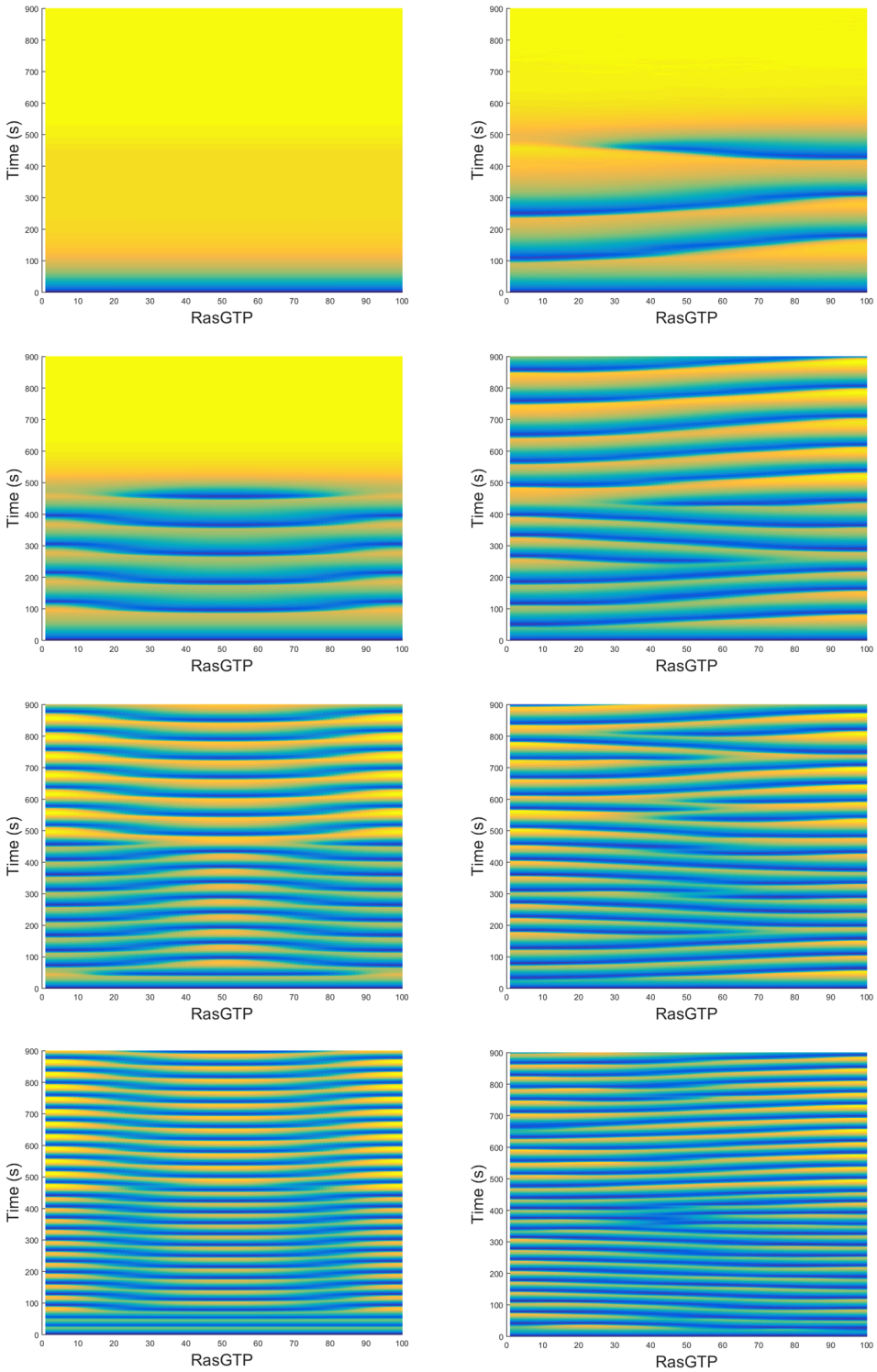

Figure 7.3: In left and right column are shown deterministic and stochastic simulations for Ras-GTP waves, respectively. PI3K activity was kept activated only during the first half of the simulation. Large values of $V_{GEF} = 600s^{-1}$ (being larger from top to bottom) drive the system to a complete excitation state independently of PI3K activity.

7.4 Phase field coupled to a symmetry breaking Ras-PIP_3 system

The previous results can be extended to a two-dimensional lattice, and in the same way as with the one-dimensional model, with certain parameter values and with the inclusion of noise the presence of an excitable behavior may be observed.

The stochastic simulation displayed in Figure 7.4 with $V_{GEF} = 600s^{-1}$ shows the propagation of a PIP_3 wave over time through the square grid. Once the travelling wave decays, after a refractory period a new wave emerges (last image), demonstrating the excitable characteristics of the model. No flux boundary conditions were considered for the simulation.

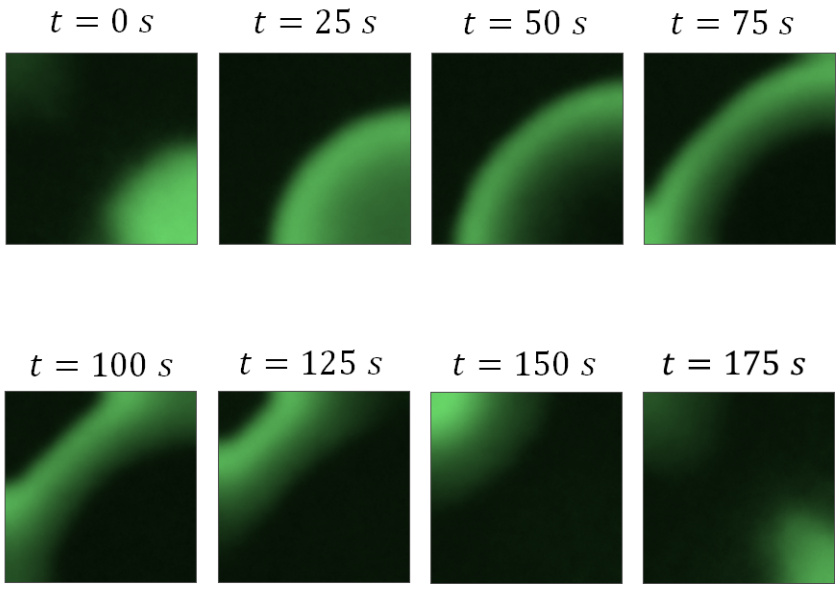

Figure 7.4: Snapshots of PIP_3 waves taken from the stochastic simulation of the two dimensional Ras-PIP_3 model on a square grid. A value of $V_{GEF} = 600s^{-1}$ and a side length of $L = 31.416\mu m$ were set.

In a similar way to previous sections the phase field technique is included in the Ras-PIP_3 model to study the cell morphology of the system. In

this particular case the phase field equation is rewritten in a similar form as other equations defined in this work for a phase field approximation, expressed in the following way:

$$\begin{aligned} \tau\frac{\partial\phi}{\partial t} &= \gamma\left(\nabla^2\phi - \frac{G'(\phi)}{\epsilon^2}\right) \\ &\quad -\beta\left(\int \phi\, dA - A_0\right)|\nabla\phi| + \alpha\,\phi\, PIP_3\,|\nabla\phi| \ , \end{aligned} \tag{7.15}$$

where one difference is the replacement of the state variable coupled with the active force term, in this case PIP_3 is incorporated in the phase field due to the strong relationship in actin polymerization which allows the cytoskeleton to reshape and form new protrusions in the direction in which the cell is moving. It is also important to mention that some parameters of the phase field were modified in comparison to the previous analysis when coupled with the symmetry breaking Ras-PIP_3 model, setting the value of $\beta = 20.26pN\mu m^{-3}$ and $\alpha = 0.03pN\mu m^{-1}$.

In Figure 7.5 one can observe the wave response for PIP_3 (A) and Ras-GTP (B) with $V_{GEF} = 600s^{-1}$. At around $t = 75s$ and $t = 200s$ one notes the presence of a lighter color domain inside the phase field and consequently a distance displacement when compared with the following image. An explanation for this behavior is that the excitation of the system allows the propagation of both waves, emulating the displacement of a cell in the direction of the membrane with greater PIP_3 and Ras-GTP concentration. After a refractory period, the cell recovers its shape to once again experience the effect of a new wave that subsequently will deform and move the cell.

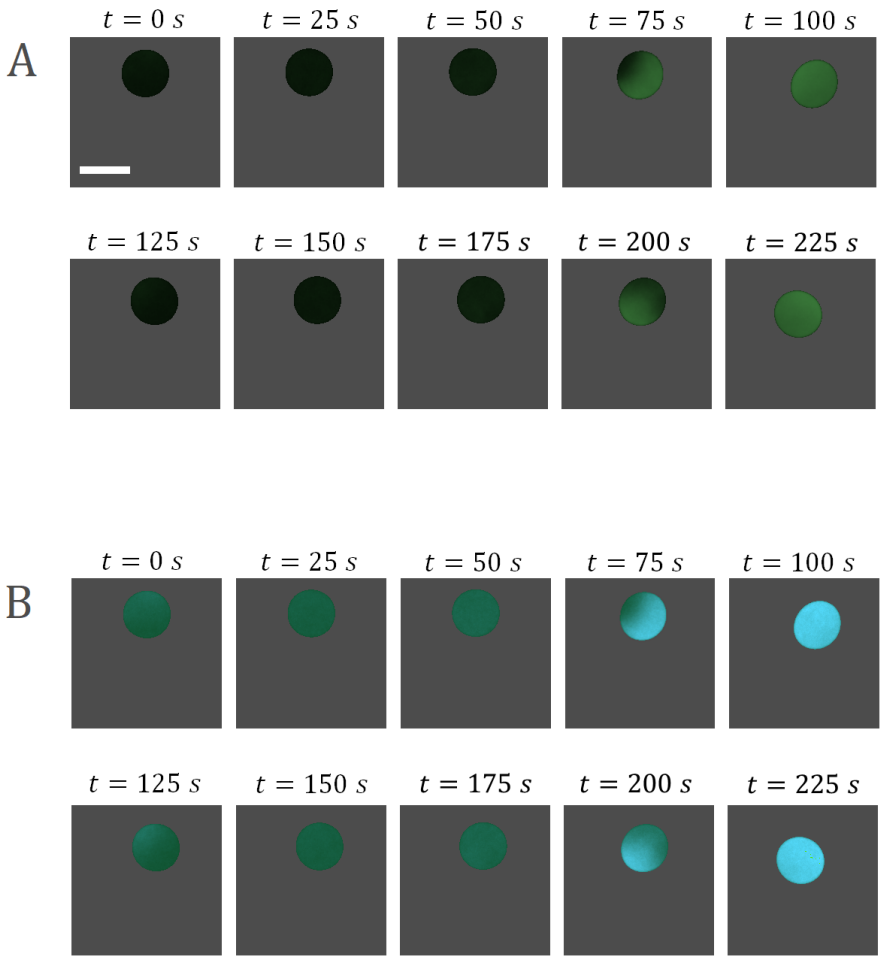

Figure 7.5: Stochastic simulations of the Ras-PIP_3 model when coupled with a dynamical phase field. For the two sets of snapshots the lighter color areas indicates a bigger concentration of (A) PIP_3 and (B) Ras-GTP which is the side where the synthetic cell is migrating. A value of $V_{GEF} = 600s^{-1}$ was set. Scale bar: 10 μm.

7.5 Discussion

The study of excitability in a system is crucial to understanding the symmetry breaking process of a single cell. One example of these systems is the Ras network which is responsible for governing/activating the phosphatidylinositol lipid signaling pathways. At the same time, experimental observations exhibit PIP_3 duality in showing oscillatory and stationary dynamics. In other words, PIP_3 waves travel through the membrane in

the absence of external signals, but at the same time remain stationary in the same location facing the higher concentration in response to external signals.

The model studied here [93] specifically employs a coupled network in which the *Ras* system constitutes an excitable network where GEFS and GAPS regulates the threshold to reach excitability, while the phosphatidylinositol lipid (PIP_2, PIP_3 and PTEN) is the bistable network that generates PIP_3-high/PTEN-low and PIP_3-low/PTEN-high states. The bistable system is subordinate to the excitable network, in the sense that Ras-GTP/PI3K interaction triggers the formation of PIP_2, PIP_2 and PTEN waves which are synchronized with the Ras waves.

The combined machinery represents the cell symmetry breaking system which is the decision-making process before leading a cell into a polarized motion mode.

When the whole system is coupled with a phase field, the model is able to reproduce the preliminary deformation of the membrane and the directed migration of a moving cell.

However, further study of the model is needed to recover the main characteristics of the amoeboid motion and membrane deformation observed in other models.

In a complementary manner, the coupled phase field Ras-PIP_3 could be used to study different types of cells, such as neutrophils, and to try to validate them with experiments. Finally, another improvement would be a new design of the phosphatidylinositol lipid signaling network in order to describe, in greater detail and more realistically, the proteins involved in the reorganization of the cytoskeleton.

Chapter 8

Conclusions and outlook.

The present study examined the soil amoeba organism *Dictyostelium discoideum*. Numerical methods based on stochastic reaction diffusion equations were employed to perform the analysis.

A mathematical model composed of a reaction diffusion equation with bistable dynamics, Ornstein-Uhlenbeck noise, and coupled with a dynamic phase field was used to describe the dynamics of the baseline cell membrane. The numerical results of the simulations showed successful qualitative agreement with essential morphological features for the different motility scenarios observed in the experiments of *Dictyostelium discoideum*. Other motility measures such as velocity, directionality and circularity also showed good quantitative agreement.

An extension of the bistable model was implemented by taking into account multiple cell interactions. Even though the number of elements (around 81 cells) was too small to systematically study collective behavior, the simulations of the deformable cell revealed rich collective dynamics and pattern formation. The simulations led to different configurations, which

depended on the type of two-cell collision, the correlation among polarity $\vec{P}$ and velocity $\vec{V}$ vectors, as well as the cell density present in the system. For example, for a simple isolated cell the vectors tended to misalign, while in the presence of a single starving cell the two vectors tended to align. Nevertheless, this alignment between vectors for starving cells was reduced by two more factors: first by interaction with multiple cells, and second by an increase in cell density. As a consequence of multiple cell interactions, it was possible to observe the transient formation of clusters, whose stability was conditioned by the deformability of the cells.

A further extension of the model was the inclusion of the virtual cell in confined environments such as microchannels. Here, simulations of starving/polarized cells exhibited highly persistent and mostly unidirectional motion while erratic/unpolarized cells presented an irregular motion from left to right or vice versa. Generally in experiments greater cell displacement is observed inside wider channels, although in some situations the observations are different. It is here that numeric simulations proved useful to investigate diverse scenarios. The correspondence between simulations and experiments depends on the type of cells and the size of channels under consideration.

For the final part of the study, two additional models based on the biochemistry of *Dictyostelium discoideum* were examined in one and two dimensions. The first model describes a bistable system which shows patches forming of Ras dynamics which induces the new formation of a pseudopod inducer. Due to the lack of mass conservation and the sensitivity of the parameters in the original model, the mechanism of cell locomotion was not robust. To increase robustness global feedback was incorporated to keep the area occupied by the Ras and the pseudopod inducer constant. This resulted in a substantial increase in the robustness of the model, yielding a

wider range of parameters where locomotion was observed. Subsequently a dynamic phase field was coupled to the system with and without mass conservation in order to compare patterns of membrane deformation and cell locomotion. Finally, different levels of chemoattractant cAMP were incorporated in order to stimulate the activation of Ras, reproducing chemotaxis to generate cell displacement towards the gradient steepness.

The last model studied here corresponds to an excitable system formed by the Ras-PIP_3 network which represents the symmetry breaking of a cell. The model displays Ras wave generation regardless of the signal of the positive feedback from PIP_3. Later, once the excitable network was coupled with a dynamic phase field, properties such as directed cell migration and membrane deformation were successfully reproduced by the model.

One extension of the model would be to explore the capacity of cells to carry and transport micro-cargo particles, which would lead to a better understanding of the adhesion process of *Dictyostelium discoideum* and the behavior of this organism in the presence of different cargo particle types .

To date, most computational study of cell migration has focused on two-dimensional morphologies because of the obvious simplification of the computational cost and time. Nevertheless, cell migration is a three-dimensional process. For this reason, the models may be adapted to a three-dimensional environment to simulate motility and membrane deformation at the tissue level.

Furthermore, the models employed in this work can be extended to the study of different types of cells (e.g., keratocytes, T-cells and neutrophils) under diverse conditions, complementing the existing bibliography with experimental data.

In summary, mathematical and computational models are useful in different research disciplines, such as physics and biology. They provide an abstraction by helping to reduce a problem to its essential characteristics for different scenarios.

Bibliography

[1] Andrey B Rubin. *Fundamentals of Biophysics*. John Wiley & Sons, 2014.

[2] Bruce Alberts, Alexander Johnson, Julian Lewis, Martin Raff, Keith Roberts, and Peter Walter. Molecular biology of the cell. garland science. *New York*, pages 1227–1242, 2015.

[3] Carl R Woese and George E Fox. Phylogenetic structure of the prokaryotic domain: the primary kingdoms. *Proceedings of the National Academy of Sciences*, 74(11):5088–5090, 1977.

[4] Carl R Woese, Otto Kandler, and Mark L Wheelis. Towards a natural system of organisms: proposal for the domains archaea, bacteria, and eucarya. *Proceedings of the National Academy of Sciences*, 87(12):4576–4579, 1990.

[5] Robert H Whittaker and Lynn Margulis. Protist classification and the kingdoms of organisms. *Biosystems*, 10(1-2):3–18, 1978.

[6] Joseph M Scamardella. Not plants or animals: a brief history of the origin of kingdoms protozoa, protista and protoctista. 1999.

[7] Clement KM Tsui, Wyth Marshall, Rinka Yokoyama, Daiske Honda, J Casey Lippmeier, Kelly D Craven, Paul D Peterson, and Mary L Berbee. Labyrinthulomycetes phylogeny and its implications for the

evolutionary loss of chloroplasts and gain of ectoplasmic gliding. *Molecular Phylogenetics and Evolution*, 50(1):129–140, 2009.

[8] Kenneth B Raper. Dictyostelium discoideum, an ew species of. *Journal of agricultural research*, 50:135, 1935.

[9] Petra Fey, Anthony S Kowal, Pascale Gaudet, Karen E Pilcher, and Rex L Chisholm. Protocols for growth and development of dictyostelium discoideum. *Nature protocols*, 2(6):1307, 2007.

[10] Hanna Brzeska, Kevin Pridham, Godefroy Chery, Margaret A Titus, and Edward D Korn. The association of myosin ib with actin waves in dictyostelium requires both the plasma membrane-binding site and actin-binding region in the myosin tail. *PloS one*, 9(4):e94306, 2014.

[11] Sarah J Annesley and Paul R Fisher. Dictyostelium discoideum—a model for many reasons. *Molecular and cellular biochemistry*, 329(1):73–91, 2009.

[12] Peter Devreotes. Dictyostelium discoideum: a model system for cell-cell interactions in development. *Science*, 245(4922):1054–1058, 1989.

[13] Albert Goldbeter. Oscillations and waves of cyclic amp in dictyostelium: a prototype for spatio-temporal organization and pulsatile intercellular communication. *Bulletin of mathematical biology*, 68(5):1095–1109, 2006.

[14] Pauline Schaap. Evolution of developmental cyclic adenosine monophosphate signaling in the dictyostelia from an amoebozoan stress response. *Development, growth & differentiation*, 53(4):452–462, 2011.

[15] Yasuo Maeda and Junji Chida. Control of cell differentiation

by mitochondria, typically evidenced in dictyostelium development. *Biomolecules*, 3(4):943–966, 2013.

[16] Robert Day Allen. Motility. *The Journal of cell biology*, 91(3):148s–155s, 1981.

[17] Hiroyuki Terashima, Seiji Kojima, and Michio Homma. Flagellar motility in bacteria: structure and function of flagellar motor. *International review of cell and molecular biology*, 270:39–85, 2008.

[18] Jørgen Henrichsen. Twitching motility. *Annual review of microbiology*, 37(1):81–93, 1983.

[19] John S Mattick. Type iv pili and twitching motility. *Annual Reviews in Microbiology*, 56(1):289–314, 2002.

[20] Daniel B Kearns. A field guide to bacterial swarming motility. *Nature Reviews Microbiology*, 8(9):634–644, 2010.

[21] T Mignot. The elusive engine in myxococcus xanthus gliding motility. *Cellular and Molecular Life Sciences*, 64(21):2733–2745, 2007.

[22] Yukinori Nishigami, Masatoshi Ichikawa, Toshiya Kazama, Ryo Kobayashi, Teruo Shimmen, Kenichi Yoshikawa, and Seiji Sonobe. Reconstruction of active regular motion in amoeba extract: Dynamic cooperation between sol and gel states. *PloS one*, 8(8):e70317, 2013.

[23] Dennis Bray. *Cell movements: from molecules to motility*. Garland Science, 2000.

[24] Raimon Sunyer, Vito Conte, Jorge Escribano, Alberto Elosegui-Artola, Anna Labernadie, Léo Valon, Daniel Navajas, José Manuel García-Aznar, José J Muñoz, Pere Roca-Cusachs, et al. Collective cell durotaxis emerges from long-range intercellular force transmission. *Science*, 353(6304):1157–1161, 2016.

[25] Deborah Huber, Ali Oskooei, Xavier Casadevall i Solvas, Andrew Demello, and Govind V Kaigala. Hydrodynamics in cell studies. *Chemical reviews*, 118(4):2042–2079, 2018.

[26] Barbara Cortese, Ilaria Elena Palamà, Stefania D'Amone, and Giuseppe Gigli. Influence of electrotaxis on cell behaviour. *Integrative Biology*, 6(9):817–830, 2014.

[27] Matthias Kiel, Dimitri Berh, Jens Daniel, Nils Otto, Adrian ter Steege, Xiaoyi Jiang, Eva Liebau, and Benjamin Risse. A multipurpose worm tracker based on fim. *bioRxiv*, page 352948, 2018.

[28] Borge Ten Hagen, Felix Kümmel, Raphael Wittkowski, Daisuke Takagi, Hartmut Löwen, and Clemens Bechinger. Gravitaxis of asymmetric self-propelled colloidal particles. *Nature communications*, 5(1):1–7, 2014.

[29] Gáspár Jékely. Evolution of phototaxis. *Philosophical Transactions of the Royal Society B: Biological Sciences*, 364(1531):2795–2808, 2009.

[30] Anat Bahat and Michael Eisenbach. Sperm thermotaxis. *Molecular and cellular endocrinology*, 252(1-2):115–119, 2006.

[31] Michael Eisenbach. Chemotaxis. *Wiley Encyclopedia of Chemical Biology*, pages 1–8, 2007.

[32] M Elizabeth Fini. Keratocyte and fibroblast phenotypes in the repairing cornea. *Progress in retinal and eye research*, 18(4):529–551, 1999.

[33] Judith A West-Mays and Dhruva J Dwivedi. The keratocyte: corneal stromal cell with variable repair phenotypes. *The international journal of biochemistry & cell biology*, 38(10):1625–1631, 2006.

[34] Eberhard Nieschlag, S Nieschlag, and Ursula-F Habenicht. *Spermatogenesis—Fertilization—Contraception: Molecular, Cellular and Endocrine Events in Male Reproduction*, volume 4. Springer Science & Business Media, 2013.

[35] Marco Baggiolini. Chemokines and leukocyte traffic. *Nature*, 392(6676):565–568, 1998.

[36] Mohammad Madjid, Imran Awan, James T Willerson, and S Ward Casscells. Leukocyte count and coronary heart disease: implications for risk assessment. *Journal of the American College of Cardiology*, 44(10):1945–1956, 2004.

[37] W James Nelson. Adaptation of core mechanisms to generate cell polarity. *Nature*, 422(6933):766–774, 2003.

[38] Bob Goldstein and Ian G Macara. The par proteins: fundamental players in animal cell polarization. *Developmental cell*, 13(5):609–622, 2007.

[39] Thomas J Klein and Marek Mlodzik. Planar cell polarization: an emerging model points in the right direction. *Annu. Rev. Cell Dev. Biol.*, 21:155–176, 2005.

[40] Wouter-Jan Rappel and Leah Edelstein-Keshet. Mechanisms of cell polarization. *Current opinion in systems biology*, 3:43–53, 2017.

[41] Sandrine Etienne-Manneville. Actin and microtubules in cell motility: which one is in control? *Traffic*, 5(7):470–477, 2004.

[42] Daniel A Fletcher and R Dyche Mullins. Cell mechanics and the cytoskeleton. *Nature*, 463(7280):485–492, 2010.

[43] TJ Mitchison and LP Cramer. Actin-based cell motility and cell locomotion. *Cell*, 84(3):371–379, 1996.

[44] Jonathan M Scholey, Ingrid Brust-Mascher, and Alex Mogilner. Cell division. *Nature*, 422(6933):746–752, 2003.

[45] Elisabetta Dejana. Endothelial cell–cell junctions: happy together. *Nature reviews Molecular cell biology*, 5(4):261–270, 2004.

[46] Alphée Michelot and David G Drubin. Building distinct actin filament networks in a common cytoplasm. *Current Biology*, 21(14):R560–R569, 2011.

[47] Revathi Ananthakrishnan and Allen Ehrlicher. The forces behind cell movement. *International journal of biological sciences*, 3(5):303, 2007.

[48] Alexander D Bershadsky and Michael M Kozlov. Crawling cell locomotion revisited. *Proceedings of the National Academy of Sciences*, 108(51):20275–20276, 2011.

[49] Natalie Andrew and Robert H Insall. Chemotaxis in shallow gradients is mediated independently of ptdins 3-kinase by biased choices between random protrusions. *Nature cell biology*, 9(2):193–200, 2007.

[50] Peter JM Van Haastert and Peter N Devreotes. Chemotaxis: signalling the way forward. *Nature reviews Molecular cell biology*, 5(8):626–634, 2004.

[51] Peter JM van Haastert, Ineke Keizer-Gunnink, and Arjan Kortholt. Coupled excitable ras and f-actin activation mediates spontaneous pseudopod formation and directed cell movement. *Molecular biology of the cell*, 28(7):922–934, 2017.

[52] Andrey B Rubin. *Compendium of biophysics*. John Wiley & Sons, 2017.

[53] Richard FitzHugh. Impulses and physiological states in theoretical models of nerve membrane. *Biophysical journal*, 1(6):445–466, 1961.

[54] Jinichi Nagumo, Suguru Arimoto, and Shuji Yoshizawa. An active pulse transmission line simulating nerve axon. *Proceedings of the IRE*, 50(10):2061–2070, 1962.

[55] Thomas Eissing, Holger Conzelmann, Ernst D Gilles, Frank Allgower, Eric Bullinger, and Peter Scheurich. Bistability analyses of a caspase activation model for receptor-induced apoptosis. *Journal of Biological Chemistry*, 279(35):36892–36897, 2004.

[56] D Kim, O Rath, W Kolch, and Kwang-Hyun Cho. A hidden oncogenic positive feedback loop caused by crosstalk between wnt and erk pathways. *Oncogene*, 26(31):4571–4579, 2007.

[57] MR Boyet and BR Jewell. Analysis of the effects of changes in rate and rhythm upon electrical activity in the heart. *Progress in biophysics and molecular biology*, 36:1–52, 1981.

[58] Elisabetta Tosti. Dynamic roles of ion currents in early development. *Molecular reproduction and development*, 77(10):856–867, 2010.

[59] Adolph Fick. V. on liquid diffusion. *The London, Edinburgh, and Dublin Philosophical Magazine and Journal of Science*, 10(63):30–39, 1855.

[60] Peter Grindrod. *The theory and applications of reaction-diffusion equations: patterns and waves*. Clarendon Press, 1996.

[61] Joel Smoller. *Shock waves and reaction—diffusion equations*, volume 258. Springer Science & Business Media, 2012.

[62] Yoichiro Mori, Alexandra Jilkine, and Leah Edelstein-Keshet. Wave-pinning and cell polarity from a bistable reaction-diffusion system. *Biophysical journal*, 94(9):3684–3697, 2008.

[63] William M Bement and George von Dassow. Single cell pattern formation and transient cytoskeletal arrays. *Current opinion in cell biology*, 26:51–59, 2014.

[64] William J Boettinger, James A Warren, Christoph Beckermann, and Alain Karma. Phase-field simulation of solidification. *Annual review of materials research*, 32(1):163–194, 2002.

[65] Antonio J Pons and Alain Karma. Helical crack-front instability in mixed-mode fracture. *Nature*, 464(7285):85–89, 2010.

[66] Nele Moelans, Bart Blanpain, and Patrick Wollants. An introduction to phase-field modeling of microstructure evolution. *Calphad*, 32(2):268–294, 2008.

[67] R Folch, J Casademunt, A Hernández-Machado, and L Ramirez-Piscina. Phase-field model for hele-shaw flows with arbitrary viscosity contrast. i. theoretical approach. *Physical Review E*, 60(2):1724, 1999.

[68] Danying Shao, Herbert Levine, and Wouter-Jan Rappel. Coupling actin flow, adhesion, and morphology in a computational cell motility model. *Proceedings of the National Academy of Sciences*, 109(18):6851–6856, 2012.

[69] Daisuke Taniguchi, Shuji Ishihara, Takehiko Oonuki, Mai Honda-Kitahara, Kunihiko Kaneko, and Satoshi Sawai. Phase geometries of two-dimensional excitable waves govern self-organized morphody-

namics of amoeboid cells. *Proceedings of the National Academy of Sciences*, 110(13):5016–5021, 2013.

[70] Brian A. Camley, Yanxiang Zhao, Bo Li, Herbert Levine, and Wouter-Jan Rappel. Crawling and turning in a minimal reaction-diffusion cell motility model: Coupling cell shape and biochemistry. *Phys. Rev. E*, 95:012401, Jan 2017.

[71] Thierry Biben, Klaus Kassner, and Chaouqi Misbah. Phase-field approach to three-dimensional vesicle dynamics. *Physical Review E*, 72(4):041921, 2005.

[72] Julien Kockelkoren, Herbert Levine, and Wouter-Jan Rappel. Computational approach for modeling intra-and extracellular dynamics. *Physical Review E*, 68(3):037702, 2003.

[73] Brian A Camley, Yanxiang Zhao, Bo Li, Herbert Levine, and Wouter-Jan Rappel. Periodic migration in a physical model of cells on micropatterns. *Physical review letters*, 111(15):158102, 2013.

[74] Danying Shao, Wouter-Jan Rappel, and Herbert Levine. Computational model for cell morphodynamics. *Physical review letters*, 105(10):108104, 2010.

[75] Falko Ziebert, Sumanth Swaminathan, and Igor S Aranson. Model for self-polarization and motility of keratocyte fragments. *Journal of The Royal Society Interface*, 9(70):1084–1092, 2011.

[76] Masoud Nickaeen, Igor L Novak, Stephanie Pulford, Aaron Rumack, Jamie Brandon, Boris M Slepchenko, and Alex Mogilner. A free-boundary model of a motile cell explains turning behavior. *PLoS computational biology*, 13(11):e1005862, 2017.

[77] Brian A Camley, Yanxiang Zhao, Bo Li, Herbert Levine, and Wouter-Jan Rappel. Crawling and turning in a minimal reaction-diffusion cell motility model: Coupling cell shape and biochemistry. *Physical Review E*, 95(1):012401, 2017.

[78] Jakob Löber, Falko Ziebert, and Igor S Aranson. Modeling crawling cell movement on soft engineered substrates. *Soft matter*, 10(9):1365–1373, 2014.

[79] Eduardo Moreno, Robert Grossmann, Carsten Beta, and Sergio Alonso. From single to collective motion of social amoebae: A computational study of interacting cells. *Preprint*, 2021.

[80] Sara Najem and Martin Grant. Phase-field approach to chemotactic driving of neutrophil morphodynamics. *Physical Review E*, 88(3):034702, 2013.

[81] Dirk Alexander Kulawiak, Brian A Camley, and Wouter-Jan Rappel. Modeling contact inhibition of locomotion of colliding cells migrating on micropatterned substrates. *PLoS computational biology*, 12(12):e1005239, 2016.

[82] Nicolas Ecker and Karsten Kruse. Excitable actin dynamics and amoeboid cell migration. *Plos one*, 16(2):e0246311, 2021.

[83] Luiza Stankevicins, Nicolas Ecker, Emmanuel Terriac, Paolo Maiuri, Rouven Schoppmeyer, Pablo Vargas, Ana-Maria Lennon-Duménil, Matthieu Piel, Bin Qu, Markus Hoth, et al. Deterministic actin waves as generators of cell polarization cues. *Proceedings of the National Academy of Sciences*, 117(2):826–835, 2020.

[84] Adrian Moure and Hector Gomez. Computational model for amoe-

boid motion: Coupling membrane and cytosol dynamics. *Physical Review E*, 94(4):042423, 2016.

[85] Adrian Moure and Hector Gomez. Phase-field model of cellular migration: Three-dimensional simulations in fibrous networks. *Computer Methods in Applied Mechanics and Engineering*, 320:162–197, 2017.

[86] Adrian Moure and Hector Gomez. Three-dimensional simulation of obstacle-mediated chemotaxis. *Biomechanics and modeling in mechanobiology*, 17(5):1243–1268, 2018.

[87] Sven Flemming, Francesc Font, Sergio Alonso, and Carsten Beta. How cortical waves drive fission of motile cells. *Proceedings of the National Academy of Sciences*, 117(12):6330–6338, 2020.

[88] Sergio Alonso, Maike Stange, and Carsten Beta. Modeling random crawling, membrane deformation and intracellular polarity of motile amoeboid cells. *PloS one*, 13(8):e0201977, 2018.

[89] Eduardo Moreno, Sven Flemming, Francesc Font, Matthias Holschneider, Carsten Beta, and Sergio Alonso. Modeling cell crawling strategies with a bistable model: From amoeboid to fan-shaped cell motion. *Physica D: Nonlinear Phenomena*, page 132591, 2020.

[90] Yuansheng Cao, Elisabeth Ghabache, Yuchuan Miao, Cassandra Niman, Hiroyuki Hakozaki, Samara L Reck-Peterson, Peter N Devreotes, and Wouter-Jan Rappel. A minimal computational model for three-dimensional cell migration. *Journal of the Royal Society Interface*, 16(161):20190619, 2019.

[91] Yuansheng Cao, Elisabeth Ghabache, and Wouter-Jan Rappel. Plas-

ticity of cell migration resulting from mechanochemical coupling. *Elife*, 8, 2019.

[92] Sergio Alonso and Markus Baer. Phase separation and bistability in a three-dimensional model for protein domain formation at biomembranes. *Physical biology*, 7(4):046012, 2010.

[93] Seiya Fukushima, Satomi Matsuoka, and Masahiro Ueda. Excitable dynamics of ras triggers spontaneous symmetry breaking of pip3 signaling in motile cells. *J Cell Sci*, 132(5):jcs224121, 2019.

[94] Nathan W Goehring and Stephan W Grill. Cell polarity: mechanochemical patterning. *Trends in cell biology*, 23(2):72–80, 2013.

[95] Carsten Beta and Karsten Kruse. Intracellular oscillations and waves. *Annual Review of Condensed Matter Physics*, 8:239–264, 2017.

[96] Jun Allard and Alex Mogilner. Traveling waves in actin dynamics and cell motility. *Current opinion in cell biology*, 25(1):107–115, 2013.

[97] Alexandra Jilkine and Leah Edelstein-Keshet. A comparison of mathematical models for polarization of single eukaryotic cells in response to guided cues. *PLoS computational biology*, 7(4):e1001121, 2011.

[98] Mikiya Otsuji, Shuji Ishihara, Kozo Kaibuchi, Atsushi Mochizuki, Shinya Kuroda, et al. A mass conserved reaction–diffusion system captures properties of cell polarity. *PLoS computational biology*, 3(6):e108, 2007.

[99] Carsten Beta, Gabriel Amselem, and Eberhard Bodenschatz. A bistable mechanism for directional sensing. *New Journal of Physics*, 10(8):083015, 2008.

[100] Britta Schroth-Diez, Silke Gerwig, Mary Ecke, Reiner Hegerl, Stefan Diez, and Günther Gerisch. Propagating waves separate two states of actin organization in living cells. *HFSP Journal*, 3(6):412–427, December 2009.

[101] Carsten Beta. Bistability in the actin cortex. *PMC biophysics*, 3(1):12, 2010.

[102] Satomi Matsuoka and Masahiro Ueda. Mutual inhibition between pten and pip3 generates bistability for polarity in motile cells. *Nature communications*, 9(1):4481, 2018.

[103] Steven J Altschuler, Sigurd B Angenent, Yanqin Wang, and Lani F Wu. On the spontaneous emergence of cell polarity. *Nature*, 454(7206):886, 2008.

[104] Pablo A Iglesias and Peter N Devreotes. Navigating through models of chemotaxis. *Current opinion in cell biology*, 20(1):35–40, 2008.

[105] Yuan Xiong, Chuan-Hsiang Huang, Pablo A Iglesias, and Peter N Devreotes. Cells navigate with a local-excitation, global-inhibition-biased excitable network. *Proceedings of the National Academy of Sciences*, 107(40):17079–17086, 2010.

[106] Kristen F Swaney, Chuan-Hsiang Huang, and Peter N Devreotes. Eukaryotic chemotaxis: a network of signaling pathways controls motility, directional sensing, and polarity. *Annual review of biophysics*, 39:265–289, 2010.

[107] Matthias Gerhardt, Mary Ecke, Michael Walz, Andreas Stengl, Carsten Beta, and Günther Gerisch. Actin and pip3 waves in giant cells reveal the inherent length scale of an excited state. *Journal of Cell Science*, 127(20):4507–4517, 2014.

[108] John B Walsh. An introduction to stochastic partial differential equations. In *École d'Été de Probabilités de Saint Flour XIV-1984*, pages 265–439. Springer, 1986.

[109] Robert C Dalang, Davar Khoshnevisan, Carl Mueller, David Nualart, and Yimin Xiao. *A minicourse on stochastic partial differential equations*, volume 1962. Springer, 2009.

[110] Xuerong Mao. The truncated euler–maruyama method for stochastic differential equations. *Journal of Computational and Applied Mathematics*, 290:370–384, 2015.

[111] Jordi García-Ojalvo and José Sancho. *Noise in spatially extended systems*. Springer Science & Business Media, 2012.

[112] Alex Mogilner, Jun Allard, and Roy Wollman. Cell polarity: quantitative modeling as a tool in cell biology. *Science*, 336(6078):175–179, 2012.

[113] Alex Mogilner, Erin L. Barnhart, and Kinneret Keren. Experiment, theory, and the keratocyte: An ode to a simple model for cell motility. *Seminars in Cell & Developmental Biology*, page S1084952119300369, November 2019.

[114] Peter J. M. Van Haastert and Peter N. Devreotes. Chemotaxis: signalling the way forward. *Nature Reviews Molecular Cell Biology*, 5(8):626–634, August 2004.

[115] Sarah J. Annesley and Paul R. Fisher. Dictyostelium discoideum—a model for many reasons. *Molecular and Cellular Biochemistry*, 329(1-2):73–91, September 2009.

[116] Yukako Asano, Takafumi Mizuno, Takahide Kon, Akira Nagasaki, Kazuo Sutoh, and Taro QP Uyeda. Keratocyte-like locomotion in

amib-null dictyostelium cells. *Cell motility and the cytoskeleton*, 59(1):17–27, 2004.

[117] Yuchuan Miao, Sayak Bhattacharya, Marc Edwards, Huaqing Cai, Takanari Inoue, Pablo A Iglesias, and Peter N Devreotes. Altering the threshold of an excitable signal transduction network changes cell migratory modes. *Nature cell biology*, 19(4):329, 2017.

[118] Gareth Bloomfield, David Traynor, Sophia P Sander, Douwe M Veltman, Justin A Pachebat, and Robert R Kay. Neurofibromin controls macropinocytosis and phagocytosis in dictyostelium. *Elife*, 4:e04940, 2015.

[119] Peggy Paschke, David A Knecht, Augustinas Silale, David Traynor, Thomas D Williams, Peter A Thomason, Robert H Insall, Jonathan R Chubb, Robert R Kay, and Douwe M Veltman. Rapid and efficient genetic engineering of both wild type and axenic strains of dictyostelium discoideum. *PLoS One*, 13(5):e0196809, 2018.

[120] Marc Edwards, Huaqing Cai, Bedri Abubaker-Sharif, Yu Long, Thomas J Lampert, and Peter N Devreotes. Insight from the maximal activation of the signal transduction excitable network in dictyostelium discoideum. *Proceedings of the National Academy of Sciences*, 115(16):E3722–E3730, 2018.

[121] Roman Gorelik and Alexis Gautreau. Quantitative and unbiased analysis of directional persistence in cell migration. *Nature protocols*, 9(8):1931, 2014.

[122] Lena Collenburg, Niklas Beyersdorf, Teresa Wiese, Christoph Arenz, Essa M Saied, Katrin Anne Becker-Flegler, Sibylle Schneider-Schaulies, and Elita Avota. The activity of the neutral sphingomyeli-

nase is important in t cell recruitment and directional migration. *Frontiers in immunology*, 8:1007, 2017.

[123] Maayan Lustig, Qingling Feng, Yohan Payan, Amit Gefen, and Dafna Benayahu. Noninvasive continuous monitoring of adipocyte differentiation: From macro to micro scales. *Microscopy and Microanalysis*, 25(1):119–128, 2019.

[124] Chen-Yu Lee, Sukryool Kang, Andrew D Chisholm, and Pamela C Cosman. Automated cell junction tracking with modified active contours guided by sift flow. In *2014 IEEE 11th International Symposium on Biomedical Imaging (ISBI)*, pages 290–293. IEEE, 2014.

[125] Viktoria Frank, Stefan Kaufmann, Rebecca Wright, Patrick Horn, Hiroshi Y Yoshikawa, Patrick Wuchter, Jeppe Madsen, Andrew L Lewis, Steven P Armes, Anthony D Ho, et al. Frequent mechanical stress suppresses proliferation of mesenchymal stem cells from human bone marrow without loss of multipotency. *Scientific reports*, 6(1):1–12, 2016.

[126] Athanasius FM Marée, Alexandra Jilkine, Adriana Dawes, Verônica A Grieneisen, and Leah Edelstein-Keshet. Polarization and movement of keratocytes: a multiscale modelling approach. *Bulletin of mathematical biology*, 68(5):1169–1211, 2006.

[127] Masoud Nickaeen, Igor L. Novak, Stephanie Pulford, Aaron Rumack, Jamie Brandon, Boris M. Slepchenko, and Alex Mogilner. A free-boundary model of a motile cell explains turning behavior. *PLOS Computational Biology*, 13(11):1–22, 11 2017.

[128] Jakob Löber, Falko Ziebert, and Igor S. Aranson. Collisions of deformable cells lead to collective migration. *Scientific Reports*, 5:9172, March 2015.

[129] Matthias Gerhardt, Michael Walz, and Carsten Beta. Signaling in chemotactic amoebae remains spatially confined to stimulated membrane regions. *J Cell Sci*, 127(23):5115–5125, December 2014.

[130] Oliver Nagel, Can Guven, Matthias Theves, Meghan Driscoll, Wolfgang Losert, and Carsten Beta. Geometry-Driven Polarity in Motile Amoeboid Cells. *PLoS ONE*, 9(12):e113382, December 2014.

[131] Benjamin Winkler, Igor S. Aranson, and Falko Ziebert. Confinement and substrate topography control cell migration in a 3D computational model. *Communications Physics*, 2(1):1–11, July 2019.

[132] Erin L. Barnhart, Greg M. Allen, Frank Jülicher, and Julie A. Theriot. Bipedal locomotion in crawling cells. *Biophysical Journal*, 98(6):933 – 942, 2010.

[133] Bruce Alberts, Dennis Bray, John Howard Wilson, Julian Lewis, Martin Raff, Keith Roberts, James D Watson, et al. *Molecular biology of the cell*, volume 2. Courier Corporation, 1989.

[134] Peter Friedl and Darren Gilmour. Collective cell migration in morphogenesis, regeneration and cancer. *Nature reviews Molecular cell biology*, 10(7):445–457, 2009.

[135] Mathieu Poujade, Erwan Grasland-Mongrain, A Hertzog, J Jouanneau, Philippe Chavrier, Benoît Ladoux, Axel Buguin, and Pascal Silberzan. Collective migration of an epithelial monolayer in response to a model wound. *Proceedings of the National Academy of Sciences*, 104(41):15988–15993, 2007.

[136] Carl-Philipp Heisenberg and Yohanns Bellaïche. Forces in tissue morphogenesis and patterning. *Cell*, 153(5):948–962, 2013.

[137] Dirk Dormann and Cornelis J Weijer. Chemotactic cell movement during development. *Current opinion in genetics & development*, 13(4):358–364, 2003.

[138] Denise J Montell. Border-cell migration: the race is on. *Nature reviews Molecular cell biology*, 4(1):13–24, 2003.

[139] Kevin J Cheung and Andrew J Ewald. A collective route to metastasis: Seeding by tumor cell clusters. *Science*, 352(6282):167–169, 2016.

[140] Peter Friedl, Joseph Locker, Erik Sahai, and Jeffrey E Segall. Classifying collective cancer cell invasion. *Nature cell biology*, 14(8):777–783, 2012.

[141] Reza Farhadifar, Jens-Christian Röper, Benoit Aigouy, Suzanne Eaton, and Frank Jülicher. The influence of cell mechanics, cell-cell interactions, and proliferation on epithelial packing. *Current Biology*, 17(24):2095–2104, 2007.

[142] Alexandre J Kabla. Collective cell migration: leadership, invasion and segregation. *Journal of The Royal Society Interface*, 9(77):3268–3278, 2012.

[143] Laurence Petitjean, Myriam Reffay, Erwan Grasland-Mongrain, Mathieu Poujade, Benoıt Ladoux, Axel Buguin, and Pascal Silberzan. Velocity fields in a collectively migrating epithelium. *Biophysical journal*, 98(9):1790–1800, 2010.

[144] Ricard Alert and Xavier Trepat. Physical models of collective cell migration. *Annual Review of Condensed Matter Physics*, 11:77–101, 2020.

[145] Brian A Camley and Wouter-Jan Rappel. Physical models of collective cell motility: from cell to tissue. *Journal of physics D: Applied physics*, 50(11):113002, 2017.

[146] Tamás Vicsek, András Czirók, Eshel Ben-Jacob, Inon Cohen, and Ofer Shochet. Novel type of phase transition in a system of self-driven particles. *Physical review letters*, 75(6):1226, 1995.

[147] James A Glazier and François Graner. Simulation of the differential adhesion driven rearrangement of biological cells. *Physical Review E*, 47(3):2128, 1993.

[148] François Graner and James A Glazier. Simulation of biological cell sorting using a two-dimensional extended potts model. *Physical review letters*, 69(13):2013, 1992.

[149] Tatsuzo Nagai and Hisao Honda. A dynamic cell model for the formation of epithelial tissues. *Philosophical Magazine B*, 81(7):699–719, 2001.

[150] Douglas B Staple, Reza Farhadifar, J-C Röper, Benoit Aigouy, Suzanne Eaton, and Frank Jülicher. Mechanics and remodelling of cell packings in epithelia. *The European Physical Journal E*, 33(2):117–127, 2010.

[151] Bo Li and Sean X Sun. Coherent motions in confluent cell monolayer sheets. *Biophysical journal*, 107(7):1532–1541, 2014.

[152] Dapeng Bi, Xingbo Yang, M Cristina Marchetti, and M Lisa Manning. Motility-driven glass and jamming transitions in biological tissues. *Physical Review X*, 6(2):021011, 2016.

[153] Silvanus Alt, Poulami Ganguly, and Guillaume Salbreux. Vertex models: from cell mechanics to tissue morphogenesis. *Philo-*

sophical Transactions of the Royal Society B: Biological Sciences, 372(1720):20150520, 2017.

[154] Luke Coburn, Luca Cerone, Colin Torney, Iain D Couzin, and Zoltan Neufeld. Tactile interactions lead to coherent motion and enhanced chemotaxis of migrating cells. *Physical biology*, 10(4):046002, 2013.

[155] Makiko Nonomura. Study on multicellular systems using a phase field model. *PloS one*, 7(4):e33501, 2012.

[156] Benoit Palmieri, Yony Bresler, Denis Wirtz, and Martin Grant. Multiple scale model for cell migration in monolayers: Elastic mismatch between cells enhances motility. *Scientific reports*, 5(1):1–13, 2015.

[157] Grégoire Peyret, Romain Mueller, Joseph d'Alessandro, Simon Begnaud, Philippe Marcq, René-Marc Mège, Julia M Yeomans, Amin Doostmohammadi, and Benoît Ladoux. Sustained oscillations of epithelial cell sheets. *Biophysical journal*, 117(3):464–478, 2019.

[158] Romain Mueller, Julia M Yeomans, and Amin Doostmohammadi. Emergence of active nematic behavior in monolayers of isotropic cells. *Physical review letters*, 122(4):048004, 2019.

[159] Guanming Zhang, Romain Mueller, Amin Doostmohammadi, and Julia M Yeomans. Active inter-cellular forces in collective cell motility. *arXiv preprint arXiv:2005.13087*, 2020.

[160] Benjamin Loewe, Michael Chiang, Davide Marenduzzo, and M Cristina Marchetti. Solid-liquid transition of deformable and overlapping active particles. *Physical Review Letters*, 125(3):038003, 2020.

[161] Brian A Camley, Yunsong Zhang, Yanxiang Zhao, Bo Li, Eshel Ben-Jacob, Herbert Levine, and Wouter-Jan Rappel. Polarity mechanisms

such as contact inhibition of locomotion regulate persistent rotational motion of mammalian cells on micropatterns. *Proceedings of the National Academy of Sciences*, 111(41):14770–14775, 2014.

[162] Jakob Löber, Falko Ziebert, and Igor S Aranson. Collisions of deformable cells lead to collective migration. *Scientific reports*, 5:9172, 2015.

[163] JinSeok Park, William R Holmes, Sung-Hoon Lee, Hong-Nam Kim, Deok-Ho Kim, Moon Kyu Kwak, Chiaochun Joanne Wang, Kahp-Yang Suh, Leah Edelstein-Keshet, and Andre Levchenko. A mechanochemical feedback underlies co-existence of qualitatively distinct cell polarity patterns within diverse cell populations. *arXiv preprint arXiv:1612.08948*, 2016.

[164] Michael E. Cates and Julien Tailleur. Motility-induced phase separation. *Annual Review of Condensed Matter Physics*, 6(1):219–244, 2015.

[165] Fernando Peruani, Andreas Deutsch, and Markus Bär. Nonequilibrium clustering of self-propelled rods. *Physical Review E*, 74(3):030904, 2006.

[166] Markus Bär, Robert Großmann, Sebastian Heidenreich, and Fernando Peruani. Self-propelled rods: Insights and perspectives for active matter. *Annual Review of Condensed Matter Physics*, 11:441–466, 2020.

[167] John Tyler Bonner. *Cellular slime molds*. Princeton University Press, 2015.

[168] BN Vasiev, P Hogeweg, and AV Panfilov. Simulation of dictyostelium

discoideum aggregation via reaction-diffusion model. *Physical Review Letters*, 73(23):3173, 1994.

[169] Giovanna De Palo, Darvin Yi, and Robert G Endres. A critical-like collective state leads to long-range cell communication in *Dictyostelium discoideum* aggregation. *PLoS Biology*, 15(4):e1002602, 2017.

[170] Eirikur Palsson and Hans G Othmer. A model for individual and collective cell movement in dictyostelium discoideum. *Proceedings of the National Academy of Sciences*, 97(19):10448–10453, 2000.

[171] Robert Großmann, Igor S Aranson, and Fernando Peruani. A particle-field approach bridges phase separation and collective motion in active matter. *Nature communications*, 11(1):1–12, 2020.

[172] Hugues Chaté. Dry aligning dilute active matter. *Annual Review of Condensed Matter Physics*, 11:189–212, 2020.

[173] Andreas M Menzel and Takao Ohta. Soft deformable self-propelled particles. *EPL (Europhysics Letters)*, 99(5):58001, 2012.

[174] Pawel Romanczuk, Markus Bär, Werner Ebeling, Benjamin Lindner, and Lutz Schimansky-Geier. Active brownian particles. *The European Physical Journal Special Topics*, 202(1):1–162, 2012.

[175] Jens Elgeti, Roland G Winkler, and Gerhard Gompper. Physics of microswimmers—single particle motion and collective behavior: a review. *Reports on progress in physics*, 78(5):056601, 2015.

[176] Ivo Buttinoni, Julian Bialké, Felix Kümmel, Hartmut Löwen, Clemens Bechinger, and Thomas Speck. Dynamical clustering and phase separation in suspensions of self-propelled colloidal particles. *Physical review letters*, 110(23):238301, 2013.

[177] Pouyan Keshavarz Motamed and Nima Maftoon. A systematic approach for developing mechanistic models for realistic simulation of cancer cell motion and deformation. *Scientific Reports*, 11(1):1–18, 2021.

[178] Isaac Theurkauff, Cécile Cottin-Bizonne, Jérémie Palacci, Christophe Ybert, and Lydric Bocquet. Dynamic clustering in active colloidal suspensions with chemical signaling. *Physical review letters*, 108(26):268303, 2012.

[179] L Huber, R Suzuki, T Krüger, E Frey, and AR Bausch. Emergence of coexisting ordered states in active matter systems. *Science*, 361(6399):255–258, 2018.

[180] Wouter-Jan Rappel. Cell–cell communication during collective migration. *Proceedings of the National Academy of Sciences*, 113(6):1471–1473, 2016.

[181] Juliane Zimmermann, Brian A Camley, Wouter-Jan Rappel, and Herbert Levine. Contact inhibition of locomotion determines cell–cell and cell–substrate forces in tissues. *Proceedings of the National Academy of Sciences*, 113(10):2660–2665, 2016.

[182] Peter JM van Haastert. Short-and long-term memory of moving amoeboid cells. *PloS one*, 16(2):e0246345, 2021.

[183] Leonard Bosgraaf and Peter JM Van Haastert. The ordered extension of pseudopodia by amoeboid cells in the absence of external cues. *PloS one*, 4(4):e5253, 2009.

[184] M Deforet, V Hakim, HG Yevick, G Duclos, and P Silberzan. Emergence of collective modes and tri-dimensional structures from epithelial confinement. *Nature communications*, 5(1):1–9, 2014.

[185] Kevin Doxzen, Sri Ram Krishna Vedula, Man Chun Leong, Hiroaki Hirata, Nir S Gov, Alexandre J Kabla, Benoit Ladoux, and Chwee Teck Lim. Guidance of collective cell migration by substrate geometry. *Integrative biology*, 5(8):1026–1035, 2013.

[186] Marc P Wolf, Georgette B Salieb-Beugelaar, and Patrick Hunziker. Pdms with designer functionalities—properties, modifications strategies, and applications. *Progress in Polymer Science*, 83:97–134, 2018.

[187] Hakam Agha and Christian Bahr. Nematic line defects in microfluidic channels: wedge, twist and zigzag disclinations. *Soft Matter*, 14(4):653–664, 2018.

[188] Yuejun Kang and Dongqing Li. Electrokinetic motion of particles and cells in microchannels. *Microfluidics and nanofluidics*, 6(4):431–460, 2009.

[189] Otto Manneberg, Bruno Vanherberghen, Björn Önfelt, and Martin Wiklund. Flow-free transport of cells in microchannels by frequency-modulated ultrasound. *Lab on a Chip*, 9(6):833–837, 2009.

[190] J Kim, H Ennis, T Nguyen, R Kessin, M Stojanovic, and Q Lin. Light-directed migration of d. discoideum slugs in microchannels. In *2011 16th International Solid-State Sensors, Actuators and Microsystems Conference*, pages 322–325. IEEE, 2011.

[191] Markela Ibo, Vasudha Srivastava, Douglas N Robinson, and Zachary R Gagnon. Cell blebbing in confined microfluidic environments. *PLoS One*, 11(10):e0163866, 2016.

[192] Dawit Jowhar, Gus Wright, Philip C Samson, John P Wikswo, and Christopher Janetopoulos. Open access microfluidic device for the

study of cell migration during chemotaxis. *Integrative Biology*, 2(11-12):648–658, 2010.

[193] Kimberly M Stroka, Hongyuan Jiang, Shih-Hsun Chen, Ziqiu Tong, Denis Wirtz, Sean X Sun, and Konstantinos Konstantopoulos. Water permeation drives tumor cell migration in confined microenvironments. *Cell*, 157(3):611–623, 2014.

[194] Daniel Irimia and Mehmet Toner. Spontaneous migration of cancer cells under conditions of mechanical confinement. *Integrative Biology*, 1(8-9):506–512, 2009.

[195] Oliver Nagel, Can Guven, Matthias Theves, Meghan Driscoll, Wolfgang Losert, and Carsten Beta. Geometry-driven polarity in motile amoeboid cells. *PloS one*, 9(12), 2014.

[196] Cally Scherber, Alexander J Aranyosi, Birte Kulemann, Sarah P Thayer, Mehmet Toner, Othon Iliopoulos, and Daniel Irimia. Epithelial cell guidance by self-generated egf gradients. *Integrative Biology*, 4(3):259–269, 2012.

[197] Andrew W Holle, Neethu Govindan Kutty Devi, Kim Clar, Anthony Fan, Taher Saif, Ralf Kemkemer, and Joachim P Spatz. Cancer cells invade confined microchannels via a self-directed mesenchymal-to-amoeboid transition. *Nano letters*, 19(4):2280–2290, 2019.

[198] Kerry Wilson, Alexandre Lewalle, Marco Fritzsche, Richard Thorogate, Tom Duke, and Guillaume Charras. Mechanisms of leading edge protrusion in interstitial migration. *Nature communications*, 4:2896, 2013.

[199] Fong Yin Lim, Yen Ling Koon, and Keng-Hwee Chiam. A compu-

tational model of amoeboid cell migration. *Computer methods in biomechanics and biomedical engineering*, 16(10):1085–1095, 2013.

[200] Fong Yew Leong, Qingsen Li, Chwee Teck Lim, and Keng-Hwee Chiam. Modeling cell entry into a micro-channel. *Biomechanics and modeling in mechanobiology*, 10(5):755–766, 2011.

[201] Donald P Gaver III and Stephanie M Kute. A theoretical model study of the influence of fluid stresses on a cell adhering to a microchannel wall. *Biophysical journal*, 75(2):721–733, 1998.

[202] Marco Scianna and Luigi Preziosi. Modeling the influence of nucleus elasticity on cell invasion in fiber networks and microchannels. *Journal of theoretical biology*, 317:394–406, 2013.

[203] Jordan Jacobelli, Rachel S Friedman, Mary Anne Conti, Ana-Maria Lennon-Dumenil, Matthieu Piel, Caitlin M Sorensen, Robert S Adelstein, and Matthew F Krummel. Confinement-optimized three-dimensional t cell amoeboid motility is modulated via myosin iia–regulated adhesions. *Nature immunology*, 11(10):953, 2010.

[204] KC Chaw, M Manimaran, Francis EH Tay, and S Swaminathan. A quantitative observation and imaging of single tumor cell migration and deformation using a multi-gap microfluidic device representing the blood vessel. *Microvascular research*, 72(3):153–160, 2006.

[205] ZiQiu Tong, Eric M Balzer, Matthew R Dallas, Wei-Chien Hung, Kathleen J Stebe, and Konstantinos Konstantopoulos. Chemotaxis of cell populations through confined spaces at single-cell resolution. *PloS one*, 7(1):e29211, 2012.

[206] Mark C Cross and Pierre C Hohenberg. Pattern formation outside of equilibrium. *Reviews of modern physics*, 65(3):851, 1993.

[207] AJ Koch and Hans Meinhardt. Biological pattern formation: from basic mechanisms to complex structures. *Reviews of modern physics*, 66(4):1481, 1994.

[208] Shigeru Kondo and Takashi Miura. Reaction-diffusion model as a framework for understanding biological pattern formation. *science*, 329(5999):1616–1620, 2010.

[209] Peter Gross, K Vijay Kumar, Nathan W Goehring, Justin S Bois, Carsten Hoege, Frank Jülicher, and Stephan W Grill. Guiding self-organized pattern formation in cell polarity establishment. *Nature Physics*, 15(3):293–300, 2019.

[210] Fabian Bergmann and Walter Zimmermann. On system-spanning demixing properties of cell polarization. *PloS one*, 14(6):e0218328, 2019.

[211] Fridtjof Brauns, Jacob Halatek, and Erwin Frey. Phase-space geometry of mass-conserving reaction-diffusion dynamics. *Physical Review X*, 10(4):041036, 2020.

[212] Jacob Halatek and Erwin Frey. Rethinking pattern formation in reaction–diffusion systems. *Nature Physics*, 14(5):507–514, 2018.

[213] Philipp Khuc Trong, Ernesto M Nicola, Nathan W Goehring, K Vijay Kumar, and Stephan W Grill. Parameter-space topology of models for cell polarity. *New Journal of Physics*, 16(6):065009, 2014.

[214] Helmut Kae, Chinten James Lim, George B Spiegelman, and Gerald Weeks. Chemoattractant-induced ras activation during dictyostelium aggregation. *EMBO reports*, 5(6):602–606, 2004.

[215] Martin Etzrodt, Hellen CF Ishikawa, Jeremie Dalous, Annette Müller-Taubenberger, Till Bretschneider, and Günther Gerisch.

Time-resolved responses to chemoattractant, characteristic of the front and tail of dictyostelium cells. *FEBS letters*, 580(28-29):6707–6713, 2006.

[216] Atsuo T Sasaki, Chris Janetopoulos, Susan Lee, Pascale G Charest, Kosuke Takeda, Lauren W Sundheimer, Ruedi Meili, Peter N Devreotes, and Richard A Firtel. G protein–independent ras/pi3k/f-actin circuit regulates basic cell motility. *Journal of Cell Biology*, 178(2):185–191, 2007.

[217] Changji Shi, Chuan-Hsiang Huang, Peter N Devreotes, and Pablo A Iglesias. Interaction of motility, directional sensing, and polarity modules recreates the behaviors of chemotaxing cells. *PLoS computational biology*, 9(7):e1003122, 2013.

[218] Chuan-Hsiang Huang, Ming Tang, Changji Shi, Pablo A Iglesias, and Peter N Devreotes. An excitable signal integrator couples to an idling cytoskeletal oscillator to drive cell migration. *Nature cell biology*, 15(11):1307–1316, 2013.

[219] Inbal Hecht, David A Kessler, and Herbert Levine. Transient localized patterns in noise-driven reaction-diffusion systems. *Physical review letters*, 104(15):158301, 2010.

[220] Inbal Hecht, Monica L Skoge, Pascale G Charest, Eshel Ben-Jacob, Richard A Firtel, William F Loomis, Herbert Levine, and Wouter-Jan Rappel. Activated membrane patches guide chemotactic cell motility. *PLoS computational biology*, 7(6):e1002044, 2011.

[221] Matthew P Neilson, Douwe M Veltman, Peter JM van Haastert, Steven D Webb, John A Mackenzie, and Robert H Insall. Chemotaxis: a feedback-based computational model robustly predicts multiple aspects of real cell behaviour. *PLoS Biol*, 9(5):e1000618, 2011.

[222] Daisuke Imoto, Nen Saito, Akihiko Nakajima, Gen Honda, Motohiko Ishida, Toyoko Sugita, Sayaka Ishihara, Koko Katagiri, Chika Okimura, Yoshiaki Iwadate, et al. Comparative mapping of crawling-cell morphodynamics in deep learning-based feature space. *bioRxiv*, 2020.

[223] Robert M Cooper, Ned S Wingreen, and Edward C Cox. An excitable cortex and memory model successfully predicts new pseudopod dynamics. *PloS one*, 7(3):e33528, 2012.

[224] Peter Hanggi, Thomas J Mroczkowski, Frank Moss, and Peter VE McClintock. Bistability driven by colored noise: Theory and experiment. *Physical Review A*, 32(1):695, 1985.

[225] Hendrik Anthony Kramers. Brownian motion in a field of force and the diffusion model of chemical reactions. *Physica*, 7(4):284–304, 1940.

[226] Leonard Bosgraaf and Peter JM Van Haastert. Navigation of chemotactic cells by parallel signaling to pseudopod persistence and orientation. *PloS one*, 4(8):e6842, 2009.

[227] Loling Song, Sharvari M Nadkarni, Hendrik U Bödeker, Carsten Beta, Albert Bae, Carl Franck, Wouter-Jan Rappel, William F Loomis, and Eberhard Bodenschatz. Dictyostelium discoideum chemotaxis: threshold for directed motion. *European journal of cell biology*, 85(9-10):981–989, 2006.

[228] Gabriel Amselem, Matthias Theves, Albert Bae, Eberhard Bodenschatz, and Carsten Beta. A stochastic description of dictyostelium chemotaxis. *PloS one*, 7(5):e37213, 2012.

[229] Eric Karsenti. Self-organization in cell biology: a brief history. *Nature reviews Molecular cell biology*, 9(3):255–262, 2008.

[230] Peter N Devreotes, Sayak Bhattacharya, Marc Edwards, Pablo A Iglesias, Thomas Lampert, and Yuchuan Miao. Excitable signal transduction networks in directed cell migration. *Annual review of cell and developmental biology*, 33:103–125, 2017.

[231] Yoshiyuki Arai, Tatsuo Shibata, Satomi Matsuoka, Masayuki J Sato, Toshio Yanagida, and Masahiro Ueda. Self-organization of the phosphatidylinositol lipids signaling system for random cell migration. *Proceedings of the National Academy of Sciences*, 107(27):12399–12404, 2010.

[232] Tatsuo Shibata, Masatoshi Nishikawa, Satomi Matsuoka, and Masahiro Ueda. Modeling the self-organized phosphatidylinositol lipid signaling system in chemotactic cells using quantitative image analysis. *Journal of cell science*, 125(21):5138–5150, 2012.

[233] Benjamin Lindner, Jordi Garcıa-Ojalvo, Alexander Neiman, and Lutz Schimansky-Geier. Effects of noise in excitable systems. *Physics reports*, 392(6):321–424, 2004.

[234] Masatoshi Nishikawa, Marcel Hörning, Masahiro Ueda, and Tatsuo Shibata. Excitable signal transduction induces both spontaneous and directional cell asymmetries in the phosphatidylinositol lipid signaling system for eukaryotic chemotaxis. *Biophysical journal*, 106(3):723–734, 2014.

[235] Ming Tang, Mingjie Wang, Changji Shi, Pablo A Iglesias, Peter N Devreotes, and Chuan-Hsiang Huang. Evolutionarily conserved coupling of adaptive and excitable networks mediates eukaryotic chemotaxis. *Nature communications*, 5(1):1–13, 2014.

[236] Tatsuo Shibata, Masatoshi Nishikawa, Satomi Matsuoka, and Masahiro Ueda. Intracellular encoding of spatiotemporal guidance cues in a self-organizing signaling system for chemotaxis in dictyostelium cells. *Biophysical journal*, 105(9):2199–2209, 2013.

[237] Fabian Knoch, Marco Tarantola, Eberhard Bodenschatz, and Wouter-Jan Rappel. Modeling self-organized spatio-temporal patterns of pip3 and pten during spontaneous cell polarization. *Physical biology*, 11(4):046002, 2014.

Appendices

Appendix A

Tables

Table A.1: Parameter values for the numerical generic bistable model.

Parameter	Value	Meaning
D	0.5 $\mu m^2/s$	Diffusion coefficient
k_a	2-5 s^{-1}	Reaction rate
ρ	0.02 s^{-1}	Degradation rate
σ	0.15 s^{-2}	Noise strength
τ	2 $pNs\mu m^{-2}$	Membrane dynamics time-scale
γ	2 pN	Surface tension
ϵ	0.75 μm	Membrane thickness
β	22.22 $pN\mu m^{-3}$	Parameter for total area constraint
A_0	113 μm^2	Area of the cell
δ_0	0.5	Bistability critical parameter
M	0.045 μm^{-2}	Strength of the global feedback input
k_η	0.1 s^{-1}	Ornstein-Uhlembeck rate
α	3 $pN\mu m^{-1}$	Active tension
Co	28, 56, 84 μm^2	Maximum area coverage by c
Δt	0.002 s	Time step
Δx	0.15 μm	Discretization size

Table A.2: Parameter values for the numerical biochemical bistable model.

Parameter	Value	Meaning
A		cAMP in nM
S		Stimulus, fraction of receptor in cAMP-activated form
k_0	0.01 s^{-1}	Basal production of R
k_1	1.5 s^{-1}	Stimulation production R by local occupied receptor S
$k_2 - k_2^*$	7.5-11.5 s^{-1}	Autocatalytic stimulation of R
k_3	1.5 s^{-1}	Inhibition R by global inhibitor G_R
k_4	1.0 s^{-1}	Inhibition R by local inhibitor LR
k_5	6.0-8.0 s^{-1}	Degradation of R
k_6	0.1 s^{-1}	Inhibition degradation of R
k_7	0.05 s^{-1}	Production of G_R by the average concentration $\langle R \rangle$
k_8	0.15 s^{-1}	Production of G_R by the average receptor occupancy $\langle S \rangle$
k_9	0.15 s^{-1}	Degradation of G_R
k_{10}	0.1 s^{-1}	Production L_R dependent on the local concentration of R
k_{11}	0.1 s^{-1}	Degradation of L_R
k_{12}	0.1 s^{-1}	Basal production of P
k_{13}	0.1 s^{-1}	Production P by R
$k_{14} - k_{14}^*$	9.2-11.2 s^{-1}	Autocatalytic stimulation of P
k_{15}	0.5 s^{-1}	Production P by local memory M
k_{16}	1.5 s^{-1}	Inhibition P by global inhibitor G_P
k_{17}	1.8 s^{-1}	Inhibition P by local inhibitor L_P
k_{18}	6.0-8.0 s^{-1}	Degradation P
k_{19}	0.1 s^{-1}	Production G_P by average value $\langle P \rangle$
k_{20}	0.15 s^{-1}	Degradation G_P
k_{21}	0.2 s^{-1}	Production L_P by local level of P
k_{22}	0.1 s^{-1}	Degradation LP
k_{23}	0.1 s^{-1}	Production M by local level of P
k_{24}	0.03 s^{-1}	Degradation of M
D_R	0.75 $\mu m^2/s$	Diffusion constant of R
D_{LR}	0.25 $\mu m^2/s$	Diffusion constant of L_R
D_P	0.75 $\mu m^2/s$	Diffusion constant of P
D_{LP}	0.25 $\mu m^2/s$	Diffusion constant of L_P
D_M	0.25 $\mu m^2/s$	Diffusion constant of M
n_1	2.0	Hill coefficient of autocatalytic stimulation of R
n_2	2.0	Hill coefficient of autocatalytic stimulation of P
n_3	2.0	Hill coefficient of production P by M
K_R	0.4	Level of R giving half-maximal autocatalytic stimulation of R
K_P	0.4	Level of P giving half-maximal autocatalytic stimulation of P
K_M	0.4	Level of M giving half-maximal stimulation of P
σ_R	$0.02 - 0.06$	Variance of the noise in R
σ_P	$0.015 - 0.055$	Variance of the noise in P

Table A.3: Phase field parameter values for the numerical biochemical bistable model.

Parameter	Value	Meaning
τ	2.0 $pNs\mu m^{-2}$	Membrane dynamics time-scale
γ	2.0 pN	Surface tension
ϵ	0.75 μm	Membrane thickness
β	18.64 $pN\mu m^{-3}$	Parameter for total area constraint
A_0	122.7 μm^2	Area of the cell
α	10.0 $pN\mu m^{-1}$	Active tension
C_R	30.6 μm^2	Area covered by R
C_P	30.6 μm^2	Area covered by P
η_1	$2.0s^{-1}$	Feedback parameter
Δt	$0.03 - 0.003$ s	Time step
Δx	$0.32 - 0.16$ μm	Discretization size

Table A.4: Parameter values for the numerical biochemical excitable model.

Parameter	Value	Meaning
V_{PTEN}	3 s^{-1}	Dephosphorylation rate of PIP_3 by PTEN
K_{PTEN}	500 μm^{-2}	Michaelis constant of PTEN dephosphorylation reaction
V_{PI3K}	12 s^{-1}	Phosphorylation rate of PIP_2 by PI3K
K_{PI3K}	300 μm^{-2}	Michaelis constant of PI3K phosphorylation reaction
$V_{PTENass}$	5000 molecules $\mu M^{-1}\mu m^{-2}s^{-1}$	PTEN association reaction rate by PIP_2
K_{PIP2}	2000 μm^{-2}	Michaelis constant of PTEN association reaction
λ_{PIP3}	0.2 s^{-1}	PTEN-independent PIP_3 degradation rate
β	0.01	Parameter indicates magnitude of PI3K activation by Ras
ξ	0.001 molecules $\mu M\mu m^{-2}$	A constant to transform surface to volume concentration
$PTEN_{tot}$	0.1 μm	Total concentration of PTEN
PIP_{tot}	5000 molecules μm^{-2}	Density of PIPs on plasma membrane
R	5.0 μm	Cell radius
D	0.2 $\mu m^{-2}s^{-1}$	Diffusion coefficient of molecules on plasma membrane
$PIP_3(0)$	0 molecules μm^{-2}	Initial value of PIP_3
$PIP_2(0)$	5000 molecules μm^{-2}	Initial value of PIP_2
$PTEN(0)$	0 molecules μm^{-2}	Initial value of PTEN
V_{GAPS}	16 s^{-1}	Deactivation rate of Ras by GAPs
K_{GAPS}	40 molecules μm^{-2}	Michaelis constant of GAPs deactivation reaction
V_{GEFS}	400-600 s^{-1}	Activation rate of Ras by GEFs
K_{GEFS}	3500 molecules μm^{-2}	Michaelis constant of GEFs activation reaction
$V_{feedback}$	25 s^{-1}	Reaction rate of PIP_3 feedback regulation
K_{PIP3}	0.1 molecules μm^{-2}	Michaelis constant of PIP_3 feedback regulation
λ_{RasGTP}	0.2 s^{-1}	Dissociation rate of RasGTP
λ_{RasGDP}	0.003 s^{-1}	Dissociation rate of RasGDP
k	45 molecules $\mu m^{-2}s^{-1}$	Association rate of RasGDP
$V_{GAPSass}$	1300 molecules $\mu m^{-2}\mu M^{-1}s^{-1}$	Association rate of GAPs by RasGDP
K_{RasGDP}	3000 molecules μm^{-2}	Michaelis constant of GAPs association reaction
λ_{GAPS}	$1.2s^{-1}$	Dissociation rate of GAPs
K_α	120 molecules μm^{-2}	Concentration of RasGTP for negative regulation of GAPs
α_1	0.001	Magnitude of negative regulation of GAPs
$GAPS_{tot}$	0.1 μM	Total concentration of GAPs
$RasGTP(0)$	1000 molecules μm^{-2}	Initial value of RasGTP
$RasGDP(0)$	1000 molecules μm^{-2}	Initial value of RasGDP
$GAPS(0)$	0 molecules μm^{-2}	Initial value of GAPS
τ	2.0 $pNs\mu m^{-2}$	Membrane dynamics time-scale
γ	2.0 pN	Surface tension
ϵ	0.75 μm	Membrane thickness
β	20.26 $pN\mu m^{-3}$	Parameter for total area constraint
A_0	78.54 μm^2	Area of the cell
α	0.03 $pN\mu m^{-1}$	Active tension
Δt	0.005 s	Time step
Δx	0.3141 μm	Discretization size